THE DEVELOPMENT OF AN IMPROVED FINITE ELEMENT MUSCLE MODEL AND THE INVESTIGATION OF THE PRE-LOADING EFFECTS OF ACTIVE MUSCLE ON THE FEMUR DURING FRONTAL CRASHES

by

Sebastian Mendes

A Thesis

Submitted to the Faculty

of the

WORCESTER POLYTECHNIC INSTITUTE

In partial fulfillment of the requirements for the

Degree of Master of Science

in

Civil Engineering

April 29, 2010

APPROVED:

Dr. Malcolm H. Ray, Major Advisor

Dr. Chiara Silvestri, Committee Member

Lenard D. Albano

Dr. Leonard D. Albano, Committee Member

Dr. Tahar El-Korchi, Department Head

ABSTRACT

Mammalian skeletal muscle is a very complicated biological structure to model due to its non-homogeneous and non-linear material properties as well as its complex geometry. Finite element discrete one-dimensional Hill-based elements are largely used to simulate muscles in both passive and active states. There are, however, several shortfalls to utilizing one-dimensional elements, such as the impossibility to represent muscle physical mass and complex lines of action. Additionally, the use of one-dimensional elements restricts muscle insertion sites to a limited number of nodes causing unrealistic loading distributions in the bones. The behavior of various finite element muscle models was investigated and compared to manually calculated muscle behavior. An improved finite element muscle model consisting of shell elements and Hill-based contractile truss elements in series and parallel was ultimately developed. The muscles of the thigh were then modeled and integrated into an existing 50th percentile musculo-skeletal model of the knee-thigh-hip complex. Impact simulations representing full frontal car crashes were then conducted on the model and the pre-loading effects from active thigh muscles on the femur were investigated and compared to cadaver sled test data. It was found that the active muscles produced a pre-load femoral axial force that acted to slightly stabilize the rate of stress intensification on critical stress areas on the femur. Additionally, the active muscles served to direct the distribution of stress to more concentrated areas on the femoral neck. Furthermore, the pre-load femoral axial force suggests that a higher percentage of injuries to the knee-thigh-hip complex may be due to the effects of active muscles on the femur.

ACKNOWLEDGEMENTS

My first and foremost thanks goes to Chiara for her unending assistance and wisdom that she contributed to this research. I never would have learned how to use LS-PrePost and LS-DYNA as quickly as I did if it were not for her guidance. Her knowledge, experience, and support helped me tremendously in organizing and carrying out this undertaking.

A special thanks also goes to Professor Ray who initially offered me this research assistantship. His steadfast encouragement and support helped to greatly facilitate the implementation of this research.

I am grateful for the help offered by fellow research assistants Doug Heath and Tejas Ruparel. Their vast knowledge of using LS-PrePost and LS-DYNA was indispensible. I would also like to thank the helpful student tutors in the Mathematical Sciences Department for assisting me with understanding the mathematical aspects of this research.

Acknowledgement also goes to NHTSA for sponsoring a large part of this research.

Last but not least, much thanks to Professor Albano for being a member of my research committee.

TABLE OF CONTENTS

LIST OF FIGURES

LIST OF TABLES

I. Introduction

Studies have revealed that the distribution of bodily injuries during frontal crashes has shifted from the upper body extremities to the lower body extremities. This trend has been attributed to the increased use of safety belts and air bags. An analysis of risk of injury associated with different regions of the body during frontal crashes was conducted by Kuppa et al. (2001) using real world crash data obtained from the National Automotive Sampling System/Crashworthiness Data System (NASS/CDS) for the years 1993 through 1999. A frontal crash is defined as a crash with the impact direction 10 - 2 o'clock of which full frontal crashes (i.e. impact direction is zero degrees) accounted for 23% of all frontal crashes (Kuppa, 2002). Data was collected for both belted and unbelted front outboard occupants in airbag equipped vehicles. The severity of injury was scaled according to the Abbreviated Injury Scale (AIS) which scores the severity of injury on a scale from 1 to 6, with 1 being minor, 2 moderate, 5 critical and 6 a virtually unsurvivable injury (Linn, 1995). The long term effects of lower body injury were measured according to the Functional Capacity Index (FCI) and societal effects were measured in terms of Functional Life-years Lost to Injury (LLI). It was found that the lower body extremities were the leading injured body region during frontal crashes and were the most common region of AIS 2+ injuries for front outboard occupants in airbag equipped vehicles. Furthermore, it was found that injury to the knee-thigh-hip (KTH) accounted for 55% of all AIS 2+ injuries in the lower body extremities. While these lower body injuries are generally not life threatening, they are coupled with a high level of functional loss and societal cost.

It is evident that injuries to the KTH represent a significant portion of overall AIS 2+ injuries in the lower body extremities for front seat occupants. The majority of the injuries in the KTH were found to be due to fractures of the patella and femur. Very importantly, it was discovered that the level of axial force induced in the femur is a relatively good indicator of the probability of KTH injuries in general. Hence, the probability of AIS 2+ and 3+ KTH injuries may be plotted as functions of axial force in the femur based on test data (Kuppa et al., 2001). Plots of these functions are shown in Figure 1.1.

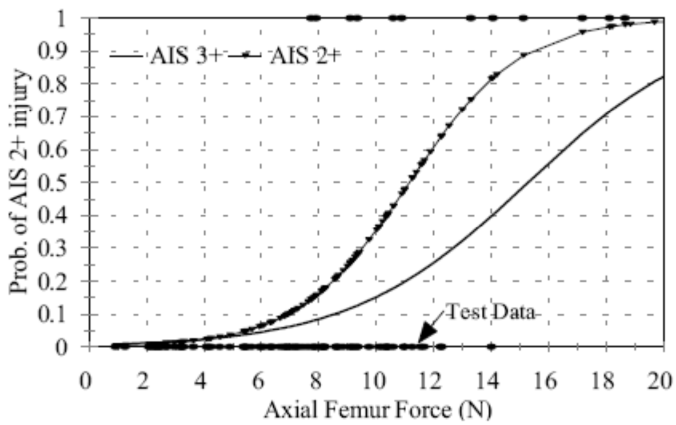

Figure 1.1. Probability of AIS 2+ and 3+ knee-thigh-hip injuries (Kuppa et al., 2001).

The role of active muscle forces in the KTH were presumed to increase the risk of injury in this region during frontal collisions. These muscles are activated by the individual typically with the purpose of applying force to the brake pedal in order to avoid the collision or bracing for the impending impact. The contraction of these muscles produces compressive forces and bending moments in the bones to which they are attached which, in effect, pre-loads the bones prior to collision. Upon collision, the combined pre-load forces and bending moments, and the force from impact, are presumed to increase the probability of injury to the KTH complex. Specifically, the pre-loading effects from the muscle groups of the thigh may increase the femoral axial force and bending moments within the femur and presumably increase the risk of injury to the KTH (Figure 1.2).

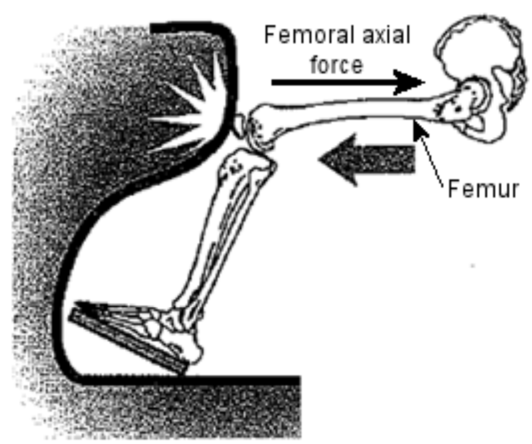

Figure 1.2. Impact force being transmitted from knee bolster through femur (Teresinski, 2005).

Past efforts (Hardin et al., 2003; Chang et al., 2008; Olivetti, 2006) have sought to investigate the influence of active muscles on femoral axial forces during frontal collisions by utilizing finite element (FE) analyses. The purpose of FE analyses are to accurately model and simulate real world occurrences by means of numerical techniques performed by computers. The application of FE modeling is especially useful when the human or monetary cost of performing real world experiments becomes too great. In the case of this research, the investigation of femoral axial forces using human cadavers with active muscles in a sled test was impossible. Hence, the utilization of FE analyses to investigate active muscle forces during collisions was the only viable alternative. This research sought to develop an improved FE muscle model and to integrate it into an existing FE model of the KTH. Impact simulations representing full frontal crashes were then performed in order to further investigate the role of active thigh muscles on the femur.

II. Literature Review

This section outlines the basic anatomy of the KTH bones and muscles as well as the state of the art of scientific and finite element modeling of skeletal muscle.

2.1 Anatomy of the Knee-Thigh-Hip

2.1.1 Bone Organization

2.1.1.1 Typical Bone Anatomy

The human skeleton is a living structure that lies within the soft tissues of the body and is thus called an endoskeleton. This endoskeleton performs several important functions. The functions most relevant to this research include support and movement. The endoskeleton consists of many individual bones each of which has a unique geometry. Bone, however, possesses common structural characteristics on a microscopic scale.

The bones of the skeleton may be grouped into the axial skeleton and the appendicular skeleton as shown in Figure 2.1. The axial skeleton provides the primary axial support for the body and includes such bones that form the skull, vertebral column, and thorax. The appendicular skeleton includes the bones that form the upper and lower limbs, and the pectoral and pelvic girdle (Spence, 1986). The bones of the KTH belong to the appendicular skeleton.

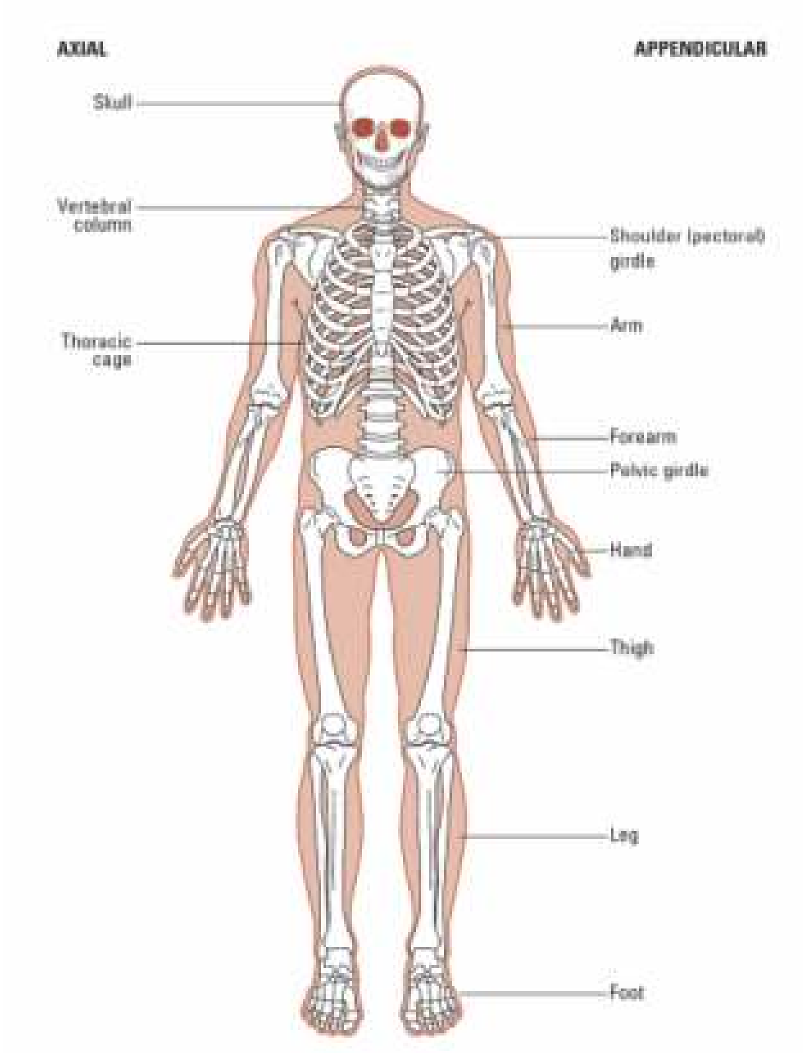

Figure 2.1. Axial and appendicular skeleton (Milner, 2008).

Bones are connected to each other by means of joints which allow for movement in one or more directions (Skeletal System). Most of the joints in the human body are called diarthrosis joints. These joints connect bones to one another by means of strong fibrous tissues called ligaments. Layers of slippery cartilage located on the interface of the adjacent bones allow for smooth movement and the absorption of jolts (Figure 2.2).

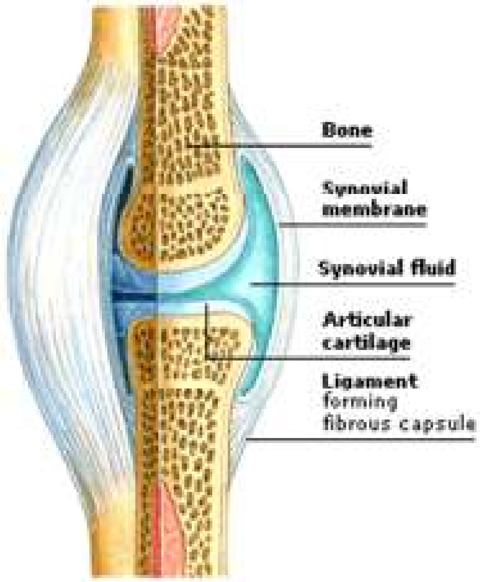

Figure 2.2. Diarthrosis joint (Kindersley, 2007).

There are several classifications of bones according to their shape including long, short, flat, and irregular (Spence, 1986). Although more than one classification of bone is present within the KTH region, the bone classification most relevant to this research is the long bone classification and includes such bones as the femur and tibia. The two most important characteristics of a long bone are that it is longer than it is wide and it has a longitudinal axis. A shaft, called a diaphysis, connects two ends called proximal and distal epiphyses, as shown in Figure 2.3. The diaphysis consists of a hollow cylinder of compact bone containing a yellow bone marrow cavity while the epiphyses consists mainly of spongy bone and contains red bone marrow.

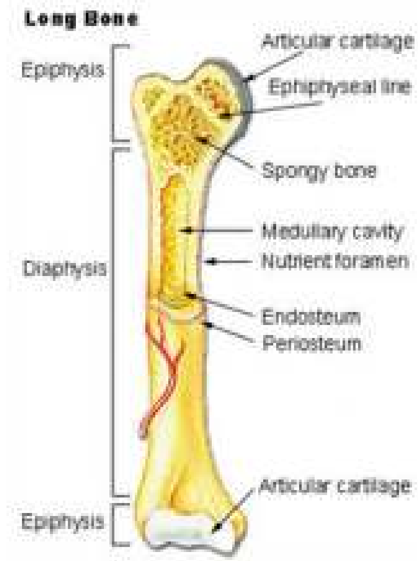

Figure 2.3. Structure of a typical long bone (SEER Training Modules).

The microscopic structure of compact bone, also known as cortical bone, is composed of interconnecting concentric layers of bone called osteons that run parallel to the longitudinal axis of the overall bone (Figure 2.4) giving them the appearance of long tubes. An intricate network of blood vessels and nerves penetrate through the cortical bone through canals to the inner bone marrow. This structure of interconnecting osteons contributes greatly to the bone's compressive strength. (Spence, 1986) Additionally, this microscopic arrangement is the reason for the orthotropic material properties of bone which make it very difficult to model (Turner and Burr, 1993). Nahum and Melvin (2002) summarized the ultimate compressive strength of cortical bone. Specifically, the ultimate compressive strength of cortical bone in the femur and pelvis was found to be approximately 190 MPa and 160 MPa, respectively (Silvestri, 2008). Stresses exceeding these ultimate compressive strengths constitute fracture of the bone.

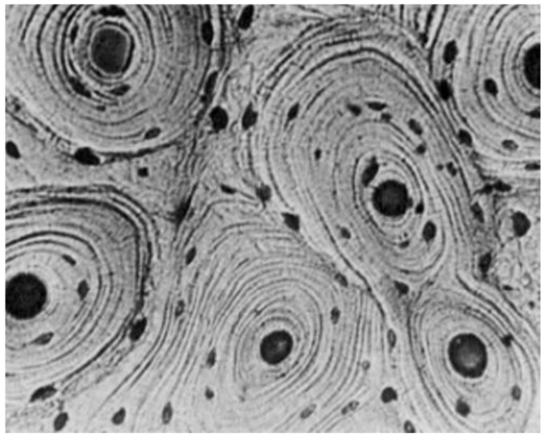

Figure 2.4. Compact (cortical) bone (IBC Dent, 2005).

Spongy bone, also known as trabecular bone, is located at the core of the epiphyses and is surrounded by an outside shell of cortical bone. The spongy bone contains red marrow and a network of blood vessels and nerves. Unlike the relatively organized structure of osteons in cortical bone, trabecular bone consists of nonconcentric layers of bone structured in various directions (Figure 2.5) giving it a porosity that is much higher than that of cortical bone (Turner and Burr, 1993). Additionally, the complex microscopic structure of trabecular bone gives it anisotropic material properties (Silvestri, 2008).

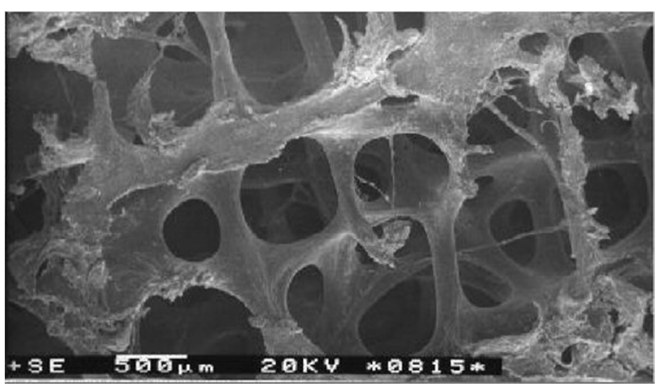

Figure 2.5. Spongy (trabecular) bone (IBC Dent, 2005).

2.1.1.2 Bone Organization

The KTH region consists of three bones including the patella, femur, and pelvis (Figures 2.6 and 2.7). The patella is a small bone that covers the knee joint between the femur and tibia. It is mainly composed of spongy bone and serves to protect the knee joint. The patella is not firmly attached to the skeleton but is rather embedded into the tendons of the quadriceps muscle group which gives those muscles much more leverage in extending the knee joint (Spence, 1986).

The femur is the longest and strongest bone in the body (Spence, 1986; Silvestri, 2008). It is a typical long bone and extends between the upper tibia and the pelvic girdle. The upper epiphysis consists of a head and a neck which serve as the joint connecting the femur with the pelvis. Muscle attachment sites are located at the border between epiphysis and diaphysis.

The pelvis is actually composed of a pair of coxal bones, each of which consists of a fusion of three distinct bones including the ilium, ischium, and pubis. The structure is singly symmetric with both coxal bones mirroring each other. The head of the femur is conjoined with the pelvis in the acetabular cup which is located where the fused ilium, ischium, and pubis bones coincide. (Spence, 1986)

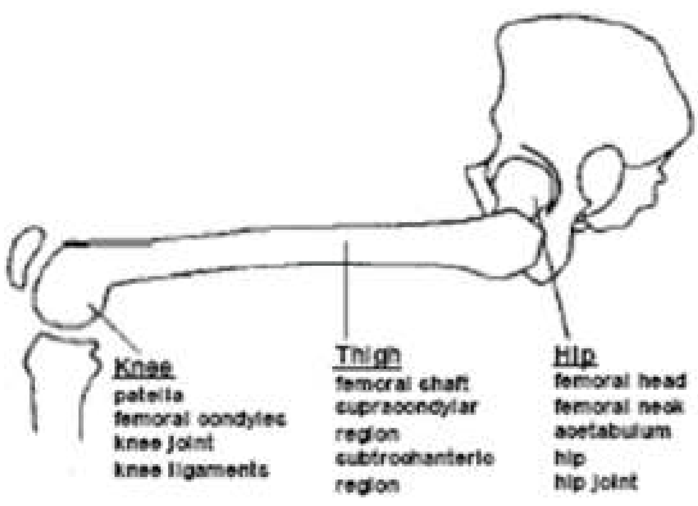

Figure 2.6. Bone structure of the KTH and common injuries associated with frontal crashes (Kuppa, 2002).

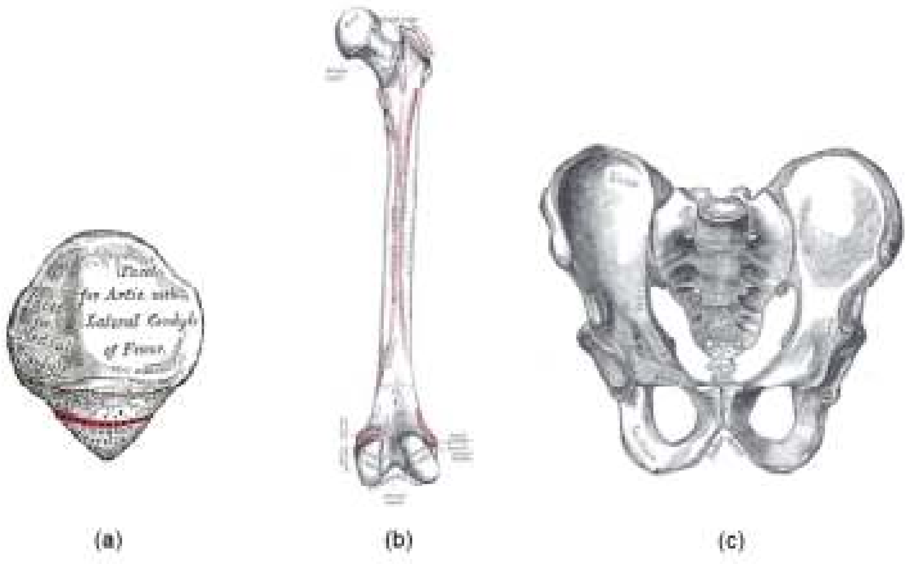

Figure 2.7. Individual bones of the KTH: (a) patella, (b) femur, and (c) pelvis (Gray, 1918).

This research assumes that the occupant of a vehicle is sitting in a neutral position, i.e. the thigh is neither adducted or abducted. With this assumption, the force from impact is typically transferred from the vehicle knee bolster via the patella to the femur and pelvis during frontal collisions (as previously shown in Figure 1.2). The force from impact produces high levels of axial force within the femur which may lead to injury mechanisms such as fracture of the femoral shaft or fracture of the femoral head and neck. Additionally, the axial force in the femur is transmitted to the pelvis through the acetabulum cup which is prone to fracture (Imberti et al., 2007).

It can be seen that the bone organization and geometry of the KTH region is very complex and difficult to replicate in a model. A 50th percentile KTH was previously developed and validated by Silvestri (2008) using LS-DYNA®. More detail concerning the modeling of the KTH is discussed later on in Section 6.1.

2.1.2 Muscle Organization

2.1.2.1 Muscle Types

The muscular system is an organization of contractile units that allow for the movement of the body. Muscles in essence convert chemical energy into mechanical work and heat thereby producing movement by means of contracting (Spence, 1986). Due to the large number of muscles in the body and their many variations, they are sorted into numerous muscle groups. There are three primary types of muscle in the body: skeletal muscle, smooth muscle, and cardiac muscle. These three muscle types are illustrated in Figure 2.8. Additionally, muscles may be classified as either voluntary or involuntary.

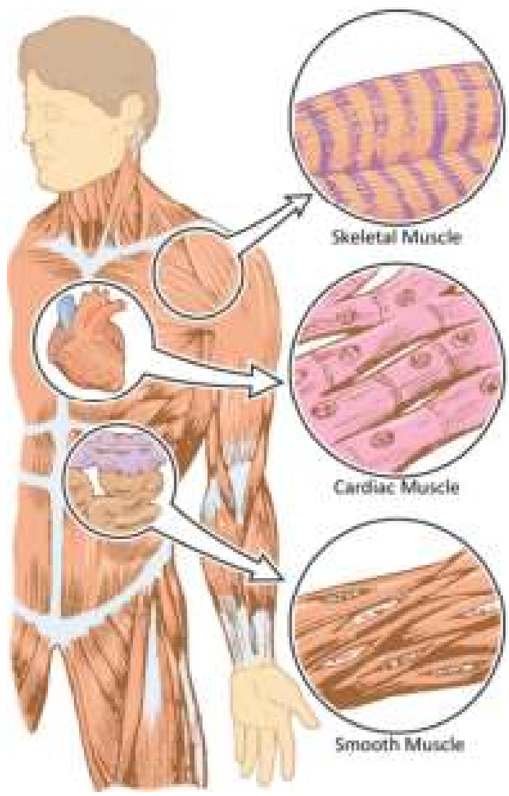

Figure 2.8. The three muscle types of the body (Calhoun Community College, 2009).

Skeletal muscles are voluntary muscles which are attached to the bones of the skeleton. The contraction of these muscles is consciously activated by the individual through the somatic nervous system and causes the movement of the bones and thus the movement of the body. The striated appearance of skeletal muscle is due to the alternating bands of light and dark stripes which indicate the unique cellular structure of the muscle. Skeletal muscles are commonly connected on both ends to strong fibrous attachments called tendons. The tendons, then, are anchored to the bones of the skeleton over a specific area. The end of the tendon attached to the more stationary part of the skeleton is called the origin, while the end attached to the more mobile part is called the insertion (Sherwood, 2007). Together, the muscle and tendon may be collectively called a muscle-tendon complex (MTC). A typical MTC is shown in Figure 2.9.

Figure 2.9. A muscle-tendon complex (National Institutes of Health, 2010).

Smooth muscle and cardiac muscle are both involuntary muscles in that they are not under the conscious control of the individual. Smooth muscles lack the striated appearance of skeletal muscle and typically form the walls of hollow structures in the body such as intestines and blood vessels. Cardiac muscle is similar to smooth muscle except that it has a striated appearance and forms the wall of the heart. (Gardner and Osburn, 1967; Spence, 1986)

The muscle type of interest concerning this research is skeletal muscle. The voluntary activation of skeletal muscles in the KTH may be initiated by an individual with the purpose of applying force to a brake pedal or bracing in the moments preceding a collision. As previously stated, the activated skeletal muscles are presumed to produce pre-loading effects on the KTH bones.

2.1.2.2 Muscle Organization

The KTH contains several skeletal muscle groups each of which have many functions. These functions include stabilizing the hip joint, providing support for the upper extremity, transmitting weight from the upper body to the legs, and moving the body by means of walking or running (Gardner and Osburn, 1967). This research focuses upon the muscle groups of the thigh since these muscles are presumed to have a significant pre-loading effect on the femur when they are activated with the intent of bracing or braking.

It is apparent that the muscles and bones of the foot, ankle, and lower leg (such as the tibia) play an imperative role in the actions of bracing and braking. Hence, it is unrealistic to exclude these muscles and bones from a comprehensive musculo-skeletal model with a primary purpose of investigating the effects from such actions. This research, however, focused specifically upon the muscles involved in pre-loading the femur (presumed to primarily be the muscle groups of the thigh) during bracing or braking. Therefore, the attainment of the architectural properties of these muscles and their transformation into an improved FE muscle model was the primary objective and was documented in detail. The attainment of the architectural properties of the muscles of the foot, ankle, and lower leg and their replication into FE muscle models is necessary for investigating pre-loading effects in those corresponding areas, but was considered to be negligible for investigating pre-loading effects on the femur. Therefore, it was decided to exclude those muscles in order to narrow the scope of the research while still obtaining reasonable results concerning the femoral axial force.

There are three primary muscle groups in the thigh. These groups include the medial compartment, the anterior compartment, and the posterior compartment. Table 2.1 provides an outline of the individual muscles belonging to each group while Figure 2.10 provides illustrations of these muscles. The medial muscles of the thigh have the primary function of adducting the thigh. The origins of these muscles are located on the pubic bone while the insertion points are located along the inside face of the femur. The anterior thigh muscles are located along the front of the thigh and primarily act in flexing the thigh. The origins of these muscles are located on various areas of the pelvis and lower spine while the insertion points are located at various locations along the front of the femur and even across the knee joint. The posterior muscles, also known as hamstring muscles, are located along the back of the thigh and primarily act in extending the hip joint and flexing the knee joint. The origins of these long muscles are located along the lower region of the pelvis while the insertion points are located at various locations along the femur and across the knee joint. A common attribute of these muscles is that they all have tendons crossing the knee joint. (Gardner and Osburn, 1967; Spence, 1996)

Table 2.1. Muscles of the thigh (Spence, 1986).

Group	Muscle
Medial compartment	Adductor magnus Adductor longus Adductor brevis Pectineus Gracilis
Anterior compartment	Sartorius Rectus femoris Vastus lateralis Vastus medialis Vastus intermedius
Posterior compartment	Biceps femoris Semitendinosus Semimembranosus

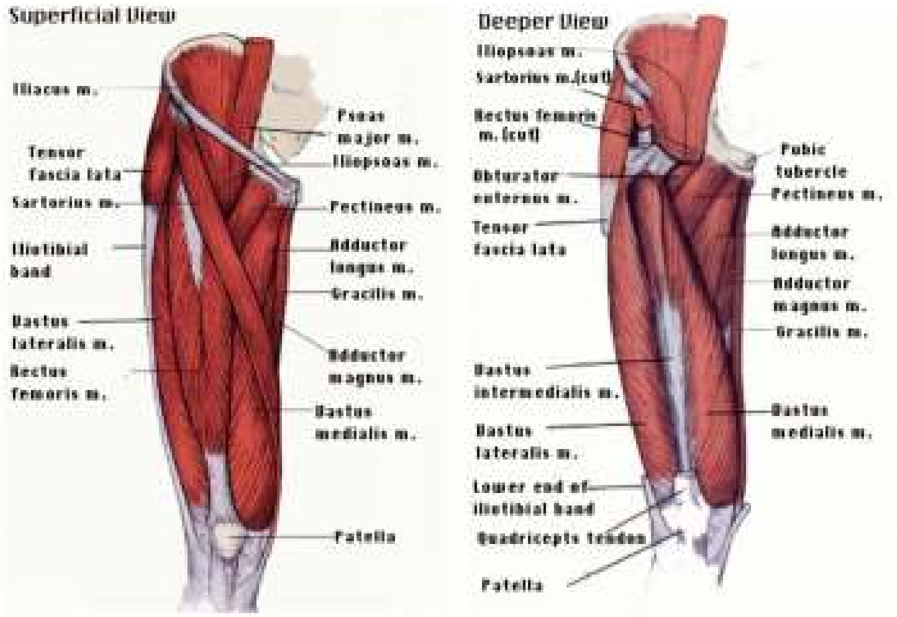

Figure 2.10. Muscles of the thigh (Medical Look, 2010).

2.1.2.3 Biological Structure and Functioning

The structure of skeletal muscle consists of thousands of cylindrical multinucleate cells called muscle fibers, which are grouped into bundles called fasciculus, and together form the overall muscle (Spence, 1986). These thin fibers have diameters of between 10 to 100 micrometers and have lengths of up to 2.5 feet. Each muscle fiber consists of several hundred to several thousand tiny threadlike components called myofibrils which themselves are composed of repeating segments called sarcomeres (Sherwood, 2007). Figure 2.11 shows a cross-sectional view of the various components of muscle tissue ranging from the overall muscle down to the myofibrils.

Muscle fibers possess a general orientation relative to the longitudinal axis of the muscle called the pennation angle. The cross-sectional area of the plane perpendicular to these fibers is called the physiological cross-sectional area (PCSA) (Lieber, 2002). The effect that the pennation angle and PCSA have on the force generating potential of a muscle is discussed in Section 4.

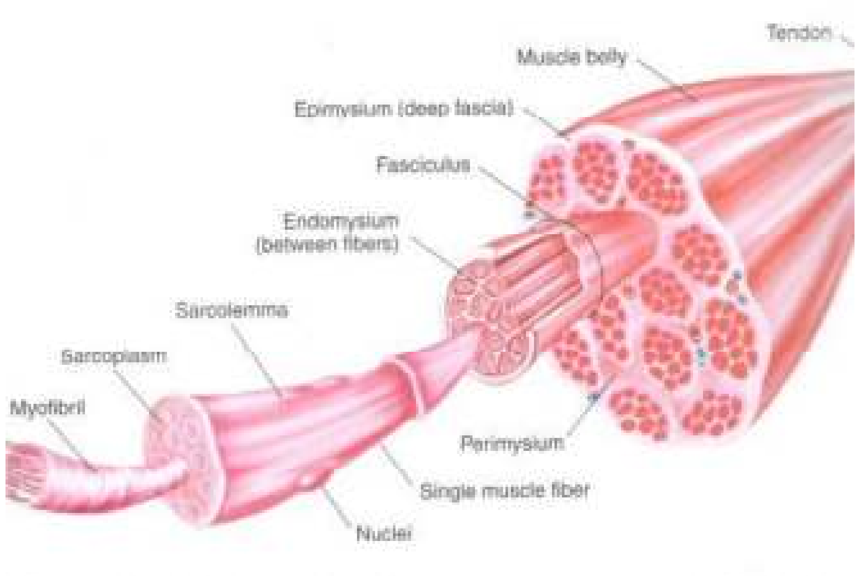

Figure 2.11. Various components of skeletal muscle tissue (Sports Fitness Advisor).

The sarcomeres are composed of myofilaments which are grouped as either thick filaments or thin filaments. The myofilaments are composed of proteins and are central to the process of muscle contraction. The thick filaments consist primarily of myosin proteins while the thin filaments consist of the proteins actin, tropomyosin, and troponin (Spence, 1986). The thick and thin filaments are structured parallel to each other, and when seen through cross section they form a hexagonal pattern similar to that of a honey comb. Bands of varying densities of myofilament exist longitudinally along each myofibril as shown in Figure 2.12. A network of tubules and membranes penetrates deep into the muscle fibers and encases each myofibril. The membranes are connected to the nervous system at locations known as neuromuscular junctions. It is at these junctions where individual motor neurons stimulate the individual myofibrils (Sherwood, 2007).

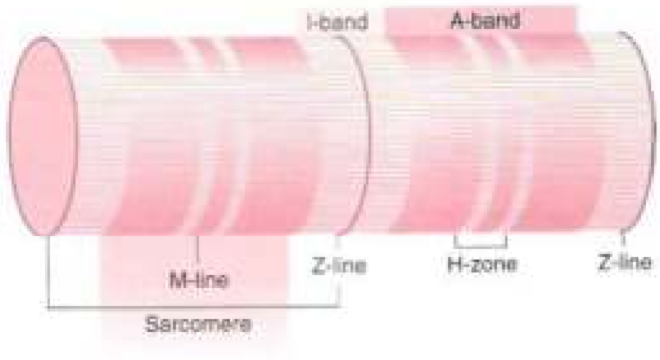

Figure 2.12. Detail of a single myofibril showing varying densities of myofilament (Sports Fitness Advisor).

It is well established that skeletal muscles are voluntary muscles whose function is to directly convert chemical energy into mechanical work and heat thereby causing the movement of bones by means of muscle contraction. This research concentrated exclusively upon the contractile properties of muscle and does not delve into the heat of shortening of muscle. However, Hill (1938) provides a well-documented account of experiments pertaining to the liberation of heat by activated frog muscle. There are two primary types of contraction (Sherwood, 2007). An isotonic contraction is when the tension induced in the muscle remains constant as the length of the muscle changes. In fact, there are two types of isotonic contractions. When the muscle shortens at a constant tension it is called concentric contraction. Conversely, when the muscle lengthens at a constant tension it is called eccentric contraction. An isometric contraction is when both the tension induced in the muscle and the length remains constant. Regardless of contraction type, skeletal muscles are consciously activated by the individual through the somatic nervous system.

The currently accepted theory of muscle contraction is the sliding-filament theory first proposed by H.E. Huxley in 1953 (Huxley, 2000). According to the theory, the contraction of muscle begins with the stimulation of motor neurons which causes the neuron to release a chemical known as acetylcholine (Hatze, 1981; Spence, 1986). This chemical causes a nerve impulse to radiate throughout the network of tubules and induces the release of calcium ions by the membranes. The release of calcium ions causes the bond between the troponin and actin in the thin filaments to weaken and therefore allows binding sites on the actin to become exposed to the myosin on the thick filament. Bulbous heads on the myosin (cross-bridges) reorient themselves to bond to the actin and produce movement of the thick filaments toward the thin filaments. Repetitions of this cycle cause the thin filaments to slide past the thick filaments and move to the center of the sarcomere. Figure 2.13 shows a schematic setup of sliding thin and thick filaments, and Figure 2.14 displays a detailed view of a single thick filament.

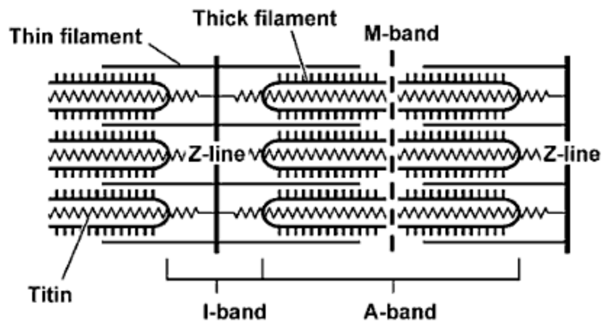

Figure 2.13. Schematic of sliding thin and thick filaments (Kumar, 2004).

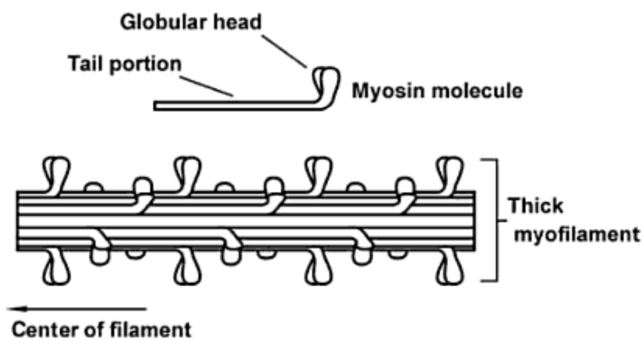

Figure 2.14. A single thick filament primarily composed of myosin proteins (Kumar, 2004).

The energy required for these activities is supplied by the splitting of adenosine triphosphate (ATP) into adenosine diphosphate (ADP) (Sherwood, 2007). The sliding of filaments in effect causes the myofilaments to shrink and the sarcomeres to contract. As a result, the thousands of muscle fibers cooperatively contract and the muscle as a whole contracts.

It was previously stated that skeletal muscle is consciously activated by the individual via the somatic nervous system. At the sub-cellular level, individual motor neurons stimulate individual myofibrils which initiate the muscle contraction process. This activation of muscle may vary from different levels ranging from zero activation to full activation. Additionally, the activation of muscle requires a certain period of time and thus may be visually represented by a time vs. activation curve denoted by A(t). An activation level of zero implies that no nerve impulses are being generated by the neuromuscular junctions, and thus the force being produced by the muscle is zero (passive muscle). A full activation level, conversely, implies that nerve impulses are being generated by the neuromuscular junctions and that the muscle is producing its maximum force (active muscle). The time for skeletal muscle to reach full activation from rest is typically very rapid (Hill, 1951).

Skeletal MTCs are commonly attached to bones across joints which in effect form lever systems (Sherwood, 2007). In these systems, the joints serve as fulcrums and the bones serve as levers. As the MTC contracts across the joint, the bone possessing the insertion end of the tendon is effectively rotated about the joint in the direction of the contraction. The flexion of the elbow joint is a typical example of this mechanism as shown in Figure 2.15. In this case the biceps muscle is the flexor and its contraction causes the flexion of the elbow joint. The flexion is terminated and the elbow undergoes extension by the contraction of the triceps muscle which acts as the extensor.

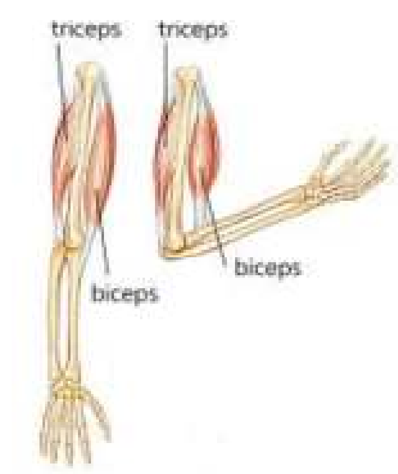

Figure 2.15. Flexion of the elbow joint (NSHS, 2009).

There exists a fundamental relationship between the muscle force and its contraction velocity and length (Sherwood, 2007). It is noted that each muscle of the body possesses unique force vs. velocity and force vs. length relationships. The force generated in a muscle depends upon the shortening velocity and length of the muscle at any given time. Additionally, the force generated is dependent upon the activation level of muscle and other physiological properties such as PCSA. The force gradually increases as the velocity of shortening gradually decreases. Also, the force varies depending upon the length of the muscle and maximum force is developed when the muscle is at an optimal length. The importance of these force-velocity and force-length relationships becomes apparent when developing scientific models of muscle.

2.2 Muscle Modeling

2.2.1 Hill-based Models

The present understanding of muscle structure and functioning has allowed for the development and continued improvement of scientific models of muscle. Most muscle models are Hill-based models which describe the behavior of active and passive muscles. Approximate solutions to equations of these models may be solved, and the resulting outputs utilized to create finite element models of muscle. The resulting finite element models may then be employed in many useful applications ranging from the determination of underlying medical conditions to the design of safer vehicle interiors.

The challenge of modeling biological structures is summarized by Oomens et al. (2003) in their paper concerning finite element modeling of skeletal muscle. Muscle tissue is known to possess nonhomogeneous material properties as previously established in the description of muscle structure. Also, muscles have a complex geometry in that they do not have a uniform cross-sectional area along their axis and may not have a straight alignment between their attachments to the skeleton. Finally, muscle tissue (mammalian skeletal muscle is implied) is known to exhibit nonlinear material behavior in that the relationship between applied stress and strain is nonlinear. These properties, however, may be described using Hill-based models.

A Hill-based model in its basic form may be described as utilizing a contractile element (CE) in series with a nonlinear elastic element (SE) to represent an active muscle. An elastic element (PE) is added in parallel to the other two elements to represent a passive muscle (Stojanovic and Kojic, 2007). A schematic of this configuration is shown in Figure 2.16.

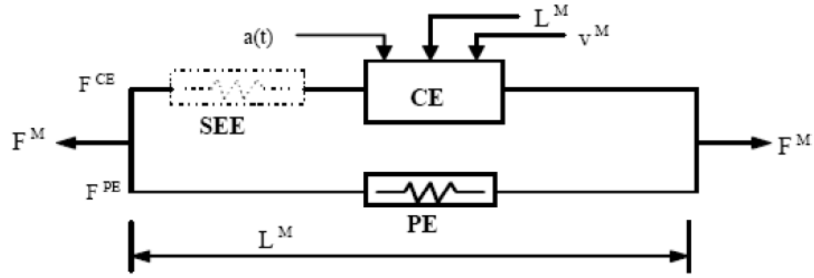

Figure 2.16. Typical Hill-based MTC model (LSTC, 2007).

Together these three elements, which may collectively be considered a black box, provide a model of the muscle-tendon complex (MTC) for both active and passive states (Olivetti, 2006). In the case of an active muscle, data including muscle length, contraction velocity, and activation level is input into the CE which then produces a corresponding contractile force. This muscle force is further influenced by the behavior of the SE. In the case of a passive muscle, the behavior of the muscle is governed entirely by PE with no influence by the CE and SE. The key aspect of the model is that the force and velocity of the contractile element is governed by Hill's characteristic force-velocity equation,

$$(F + a)\,(V + b) = c \qquad (1)$$

which may be rearranged as,

$$F = (c / (V + b)) - a \qquad (2)$$

where F is the muscle force, v is the muscle contraction velocity, and a, b, and c are unique constants. The characteristic equation describes the relationship between the force induced in a muscle to its shortening velocity and may be graphically represented as a force vs. velocity curve denoted by F(V). As previously mentioned, the force gradually increases as the velocity of contraction gradually decreases. As the force generated decreases the contraction velocity approaches a maximum value (V_{max}). The constants in the equation are unique for each individual or muscle being modeled. Thaller and Wagner (2004) note that although generalized values obtained from experiments on muscle are often used for the constants, it is necessary to measure the movement of a specific muscle in order to obtain more accurate values of the constants. Nevertheless, Hill (1938) concluded that the equation very accurately conforms to experimental results, and specifically to experiments performed on muscles of English frogs.

Hill (1939) later found constants of the characteristic equation for human skeletal muscles by conducting experiments on human arm muscles with an inertia wheel.

A relationship between the muscle force and length also exists (MacIntosh et al., 2006). This relationship is as equally important as the force-velocity relationship in governing the behavior of the contractile element. When the length of the muscle is relatively short, the active force developed is small. As the length of the muscle increases and approaches its optimal length (L_o), the force developed reaches a maximum value called the peak isometric force (F_{max}). Muscle lengths beyond the optimal length cause the force developed to decrease. As with the force-velocity relationship, the force-length relationship may be graphically represented as a force vs. length curve denoted by F(L). Additionally, F(L) curves are unique to each muscle, and thus generic curves are typically used in models.

Together, the F(V) and F(L) curves govern the contractile behavior of a Hill-based model. Generic F(V) and F(L) curves are shown in Figure 2.17. The F(V) and F(L) curves may be combined to form a three-dimensional force-velocity-length function denoted by F(V, L). A generic F(V, L) function is shown plotted in Figure 2.18. Realistically, it is very difficult to describe muscle forces while considering the three varying parameters of activation, velocity, and length. In fact, no constitutive law has yet been established to describe muscle forces while taking into account these parameters (Nigg et al., 2000). However, for the purpose of this research, many assumptions were made in order to produce reasonable results. Some of these assumptions include conjectured activation curves and the use of generic force-length and force-velocity curves.

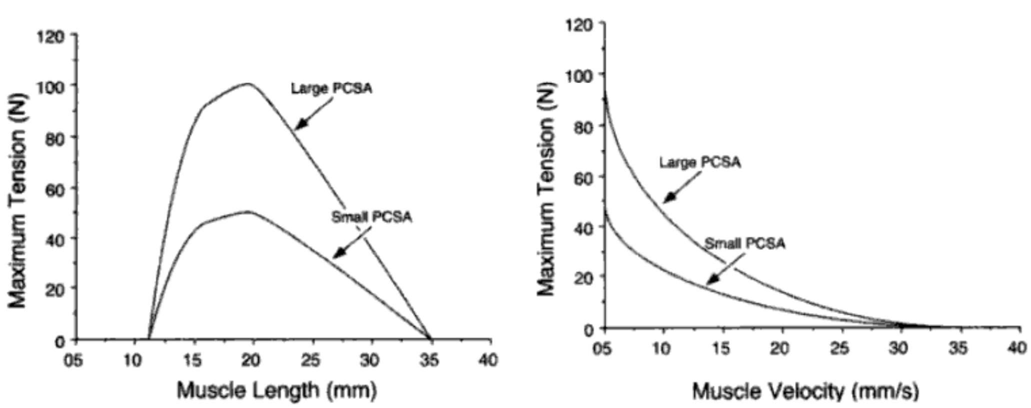

Figure 2.17. General force-length and force-velocity curves for skeletal muscle (Lieber, 2002).

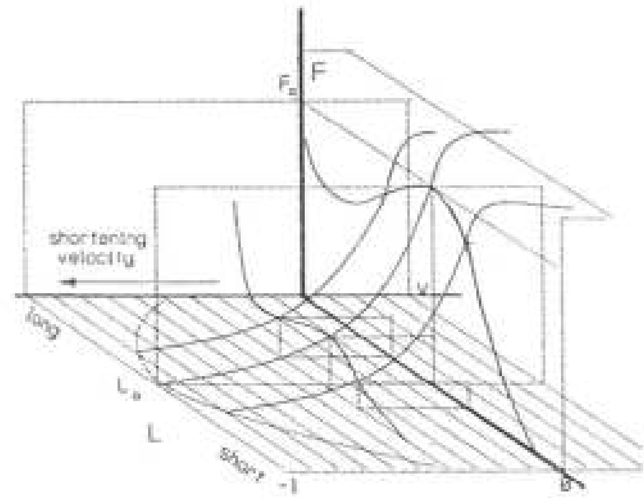

Figure 2.18. Generic force-velocity-length function (Winters and Savio, 1990).

It has been established that the force generating potential of muscle at any given time is dependent upon the muscle length and contraction velocity. However, the force potential also depends upon additional properties of muscle. For the purpose of this research, the generic curves were normalized so that the outputs of the curves could be utilized as multiplying factors in calculating the muscle force at any given time.

It must be noted that the muscle activation has an effect on the shape and magnitudes of the curves depending upon the level of activation. Due to the lack of literature concerning these effects for specific muscles, normalized levels of activation were used as scaling factors, in conjunction with the normalized generic curve outputs, in calculating the muscle force at any given time.

Hill-based models are valid for both macroscopic and microscopic modeling of muscles. A macroscopic model may be created by employing a single black box to model a single MTC. A more complex model may be created by employing many black boxes to model individual muscle fibers or even individual sarcomeres (Thaller and Wagner, 2004). A PE is necessary to model the properties of a passive muscle, i.e. when the muscle is not neurally stimulated or is put into tension due to external forces. Specifically, the PE seeks to replicate the elastic behavior of muscle structures other than the force-producing sarcomeres which include connective tissue sheaths and the fluid through which the sarcomeres move (Hatze, 1981).

When a muscle is neurally stimulated, internal tension is produced which is caused by the contraction of the sarcomeres. This tension is transferred to the tendons on both ends of the muscle through SEs. Flitney and Hirst (1970), and Morgan (1977) produced conclusive evidence that a major part of the functioning of the SE takes place within the cross-bridges (as cited in Hatze, 1981, p. 19). It is also known that the tendons are responsible for a significant part of the SE functioning. The actual mechanism for muscle contraction is the CE which may model either the contractile process of the muscle as a whole or individual muscle fibers and sarcomeres. Different arrangements of the previously discussed elements have been proposed. The Voigt model utilizes a PE in parallel with a damper both of which are placed in series with a SE, while the Maxwell model utilizes a PE in parallel with both a damper and SE in series. These models were later modified to better represent mammalian skeletal muscle by replacing the damper with a CE (Hatze, 1981). These arrangements and their variations are used by most models to replicate concentric MTC contraction.

2.2.2 Finite Element Modeling of Muscle

Currently, FE analysis programs are capable of integrating Hill-based models into computer simulations of muscle functioning. One such FE program is called LS-DYNA which was developed by Livermore Software Technology Corporation (LSTC, 2007). Olivetti (2006) utilized DYNA3D, the precursor to LS-DYNA, to investigate the role of muscle contraction in the femoral-pelvic joint region as part of research concerning the injury mechanisms to the knee-thigh-hip (KTH) during frontal collisions. Specifically, a finite element model of the lower extremities developed at the Lawrence Livermore National Laboratory (LLNL) was modified for the purpose of the research. Discrete one-dimensional Hill-based spring elements were utilized to model the actual muscles for both passive and active states (Figure 2.19).

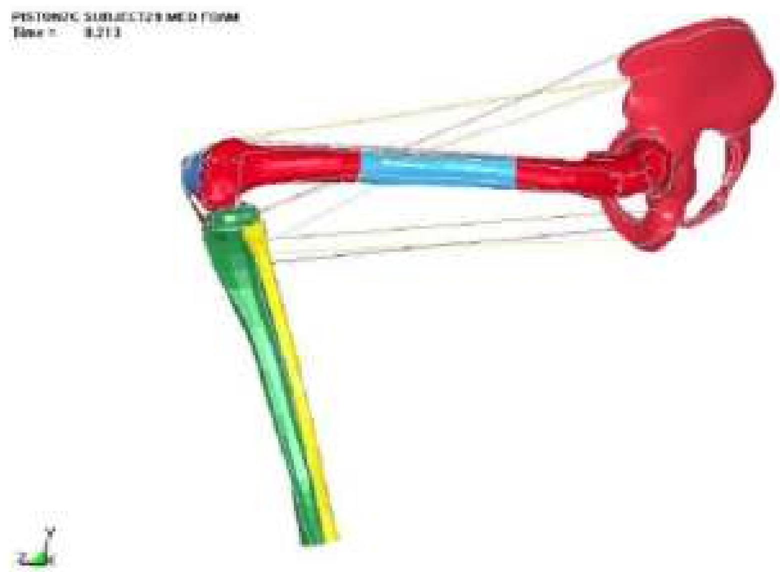

Figure 2.19. Modified LLNL KTH containing Hill-type muscle elements (Olivetti, 2006).

Normalized F(V) and F(L) curves, originating from Hill's experiments, were input into the model which then governed the behavior of the discrete elements. As previously stated, each muscle possesses unique F(V) and F(L) relationships. However, a single set of generic curves were utilized for all muscles due to the lack of literature pertaining to specific F(V) and F(L) relationships for human skeletal muscle. The F(V) and F(L) curves yielded a three-dimensional force-velocity-length curve that governed the behavior of the CE of each spring element (LSTC, 2007). An activation curve was then developed to represent the response of the body's anticipation of a collision, i.e. the level of neural activation of muscles as a function of time (A(t) curve). The F(V), F(L), and A(t) curves, then, together provided guidance for how the discrete spring elements should behave. In effect, each discrete spring element acted as a single Hill-based black box model of the MTC.

After running simulations Olivetti concluded that the role of active and passive muscles in pre-loading bones in the femoral-pelvic region during a frontal collision was less influential on injury mechanisms than originally presumed. Olivetti acknowledged that there were several shortfalls to utilizing one dimensional discrete elements in DYNA3D that may have led to less accurate simulations. Specifically, the elements were unable to represent muscle mass and complex lines of action. Additionally, the use of one dimensional elements meant that the connections of the MTC to bone were restricted to a limited number of nodes causing unrealistic loading distributions. In reality, the MTC is connected to bone over large origin and insertion sites.

Imberti et al. (2007) further investigated the role of muscle forces in the KTH during frontal collisions. Specifically, the effect of active leg and thigh muscles contracting due to the act of applying force to a brake pedal was investigated. It was similarly presumed that the contraction of muscles produces a compressive pre-load force in the bones to which the muscles are attached and may increase the risk of injury in this region during frontal collisions. An existing FE model of a 50th percentile KTH developed and validated by Silvestri (2008) was utilized to investigate these forces. Geometric and dynamic properties of the muscles involved during braking were found and input into the model. The resulting forces, stresses, and lengths of each muscle were then obtained from FE simulations.

Chang et al. (2008) also developed a FE model of the KTH with lower-extremity muscles to investigate the effects of muscle forces on KTH injuries in frontal crashes. The model was based upon an existing KTH model that was originally developed by TASS of the Netherlands using the Mathematical Dynamic Model (MADYMO) software package. Improvements to the original model were made by converting the MADYMO model into LS-DYNA code, re-meshing the geometry, and integrating Hill-type muscle elements into the geometry. The model included 35 Hill-type muscles utilizing Material 156 with mass derived from the muscle volume. The model was then validated against data obtained from experiments pertaining to individual components of the KTH such as the femur. Muscle activation data was obtained from literature and used to activate the Hill-type muscles during the FE simulations. The results of muscle tension on the KTH was then observed. The FE simulations indicated that active muscles have a definite effect upon the KTH fracture patterns during frontal collisions. However, the data obtained was not conclusive enough to make a definite claim as to whether or not the muscle tension increased the probability of KTH injuries. As with the experiments performed by Olivetti (2008), the primary reason for the inconclusiveness from the FE simulations may be traced to the limits of the FE muscle models themselves. Additionally, the general lack of specific activation patterns in literature pertaining to the muscles of the lower extremity contributed to the limits of simulations.

Hill-type muscle elements were again utilized by Hardin et al. (2003) to model human skeletal muscle in order to investigate the effect of muscles on foot and ankle forces during an automobile collision. Instead of a 3D model, a 2D musculo-skeletal model (Figure 2.20) with six muscle groups was developed and simulated in a car crash.

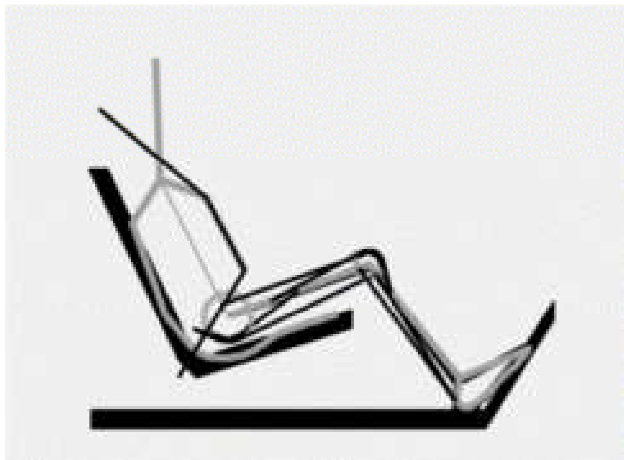

Figure 2.20. 2D Musculo-skeletal model (Hardin et al., 2003).

Three separate models were simulated including a model containing no muscles, a model containing muscles with minimum activation, and a model containing muscles with maximal activation. Unlike the inconclusive results obtained from previous research concerning the KTH, it was concluded that the foot and ankle forces were indeed dependent upon muscles forces. Furthermore, it was found that the activation level of muscle could aggravate injuries to the foot and ankle during collisions. This is the result predicted by previous research concerning the KTH but which has been thus far difficult to demonstrate. Although the research pertained to foot and ankle forces, it may presumed that a similar test setup pertaining to the KTH could be developed.

In a move away from using purely one dimensional discrete elements, a 3D solid element muscle model was developed by Hedenstierna (2008) to investigate the effect of muscles in neck injury prevention (Figure 2.21). Discrete one-dimensional Hill-based elements were combined in series and parallel with solid elements possessing hypo-elastic material properties. This combination is called a Super positioned Muscle Finite Element (SMFE). It was hoped that a 3D muscle model would allow for the compressive stiffness, mass inertia, and contact interfaces between muscles to be accurately simulated. Despite some instabilities, the SMFE model was concluded to be an improvement over purely one-dimensional muscle models in terms of contractile movement and muscle mass representation.

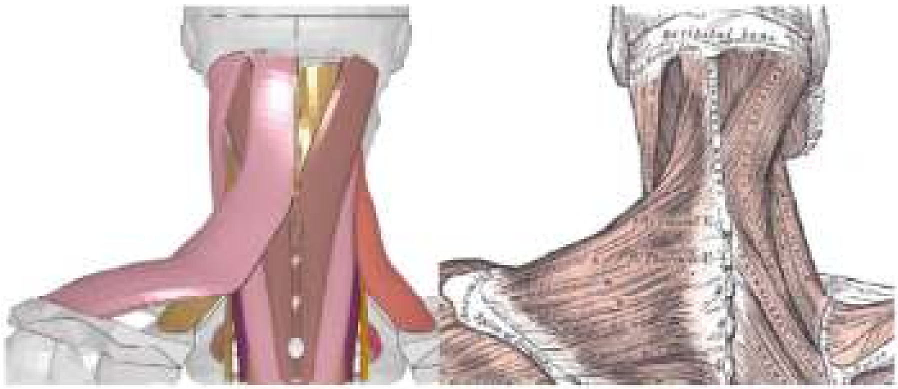

Figure 2.21. 3D solid element muscle model (Hedenstierna, 2008).

III. Objective and Methodology

The objective of this research was to develop an improved FE model of mammalian skeletal muscle using LS-DYNA and to integrate it into an existing musculo-skeletal model of a 50th percentile KTH developed and validated by Silvestri (2008) so as to further investigate the role of active muscle forces on the injury mechanisms of the KTH complex (Figure 3.1). The research concentrated on investigating the pre-load forces from the muscle groups of the thigh on the femur. It was hoped that an improved FE model of muscle may overcome the shortfalls experienced in previous models and allow for more accurate simulations.

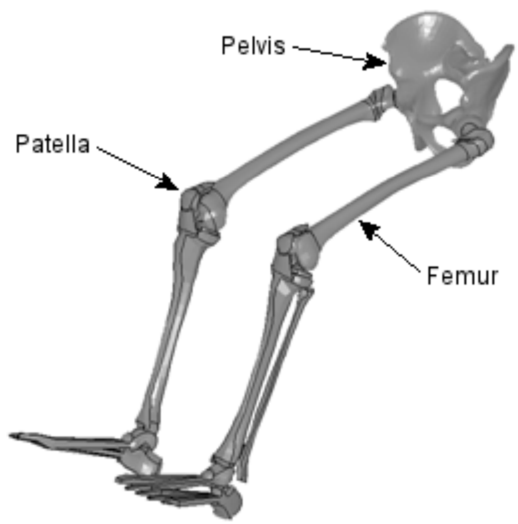

Figure 3.1. Skeletal FE model of a 50th percentile KTH.

The following tasks were performed in order to achieve the aforementioned objective.

Task 1: Review Muscle and Bone Organization of the KTH Complex

The muscle and bone organization of the KTH was reviewed. Additionally, the biological structure and functioning of mammalian skeletal muscle was assessed. The focus was concentrated on the muscles and bones assumed to be involved with the action of braking or bracing during a frontal collision. It was presumed that the muscle groups of the thigh were significantly involved in these actions.

Task 2: Review the State of the Art of Muscle Modeling

The state of the art of scientific models of muscle was reviewed. Namely, Hill-based muscle models were assessed. Additionally, the implementation of Hill-based models in FE musculo-skeletal models was reviewed.

Task 3: Obtain Muscle Properties from Literature

The physical and dynamic properties of each muscle group reviewed in Task 1 were obtained from literature. These properties were used when developing FE models of muscle and implementing them into the existing 50th percentile KTH model. These properties included the following:

- Mass
- Density
- Optimal muscle length
- Muscle fiber length
- Pennation angle
- Physiological cross sectional area (PCSA) of each muscle
- Maximum contraction velocity
- Peak isometric force
- Locations of origin/insertion points
- Tension-velocity (TV) curves
- Tension-length (TL) curves
- Activation curves

Task 4: Explore the Use of Different Elements and Materials in LS-DYNA for Use in Muscle Models

Many FE musculo-skeletal models created in LS-DYNA utilize discrete one-dimensional Hill-based spring elements to model muscles. The material most commonly associated with this discrete element is Material Type 15 for spring elements. The utilization of truss (beam) elements in conjunction with Material Type 156 was investigated as an alternative option. Additionally, an SMFE muscle was developed by combining shell elements with one-dimensional contractile elements in series and parallel. This model was investigated as a potentially more complex alternative to purely one-dimensional models. The shell elements possessed hypo-elastic properties while the 1D elements were Hill-based truss elements. The use of a 3D muscle model was aimed to provide a more accurate model of muscle and overcome the shortcomings of previous 1D models.

Task 5: Compare and Adjust the Dynamic Behavior of Three Muscle Models to Manual Calculations

The three muscle models explored in Task 4 were integrated into a control model configuration and simulated for the purpose of obtaining such data as contraction velocity and contraction force as functions of time. The properties of a specific muscle obtained from Task 3 were input into each of the three muscle models prior to testing. Additionally, manual calculations were performed to obtain data presumed to be representative of the way real muscle behaves. The data from the FE muscle simulations was then compared to the manual calculations. Appropriate adjustments were made to the FE muscle models so that their behavior conformed to the manual calculations. These adjustments were documented for future use.

Task 6: Compare and Contrast the Performance of the Spring, Truss, and SMFE Muscle Models

An FE model that replicated the flexion and extension of the knee was developed for the purpose of further investigating the spring, truss, and SMFE models under the same circumstances. Levers replicated the femur and tibia bones which were connected by a joint in order to replicate the knee joint. The model included a flexor muscle and an extensor muscle possessing properties obtained in Task 3. The first setup analyzed the flexion of the knee joint and thus contained one flexor muscle. The second setup analyzed the extension of the knee joint and contained one flexor and one extensor muscle. The adjustments obtained from Task 5 were then input into each of the muscle models. Each muscle model was then integrated into each of the control models for individual FE simulations. The simulation results from each model were to be compared to each other. The most effective muscle model was then selected for further development. It was presumed that the SMFE model would be the most effective muscle model.

Task 7: Integrate Selected Muscle Model into Existing KTH Model

The selected muscle model was further developed into the muscle groups of the thigh. The properties of these muscle groups (obtained in Task 3) were utilized to accurately develop and integrate the muscle models into the existing 50th percentile KTH.

Task 8: Perform Braking/Bracing Simulations

Frontal crash simulations of the KTH model with the improved muscle model were performed with LS-DYNA. The axial forces in the femur were obtained from impact simulations with passive muscles and different combinations of active muscles. These results were compared with experimental data obtained from sled tests. Additionally, the fracture mechanisms of the femur were investigated. A discussion and conclusion followed the completion of FE simulations. It was hoped that clearer results could be obtained concerning the effect of the active muscle groups of the thigh on femoral axial forces and fracture mechanisms during frontal collisions.

A flowchart of the methodology used is shown in Figure 3.2.

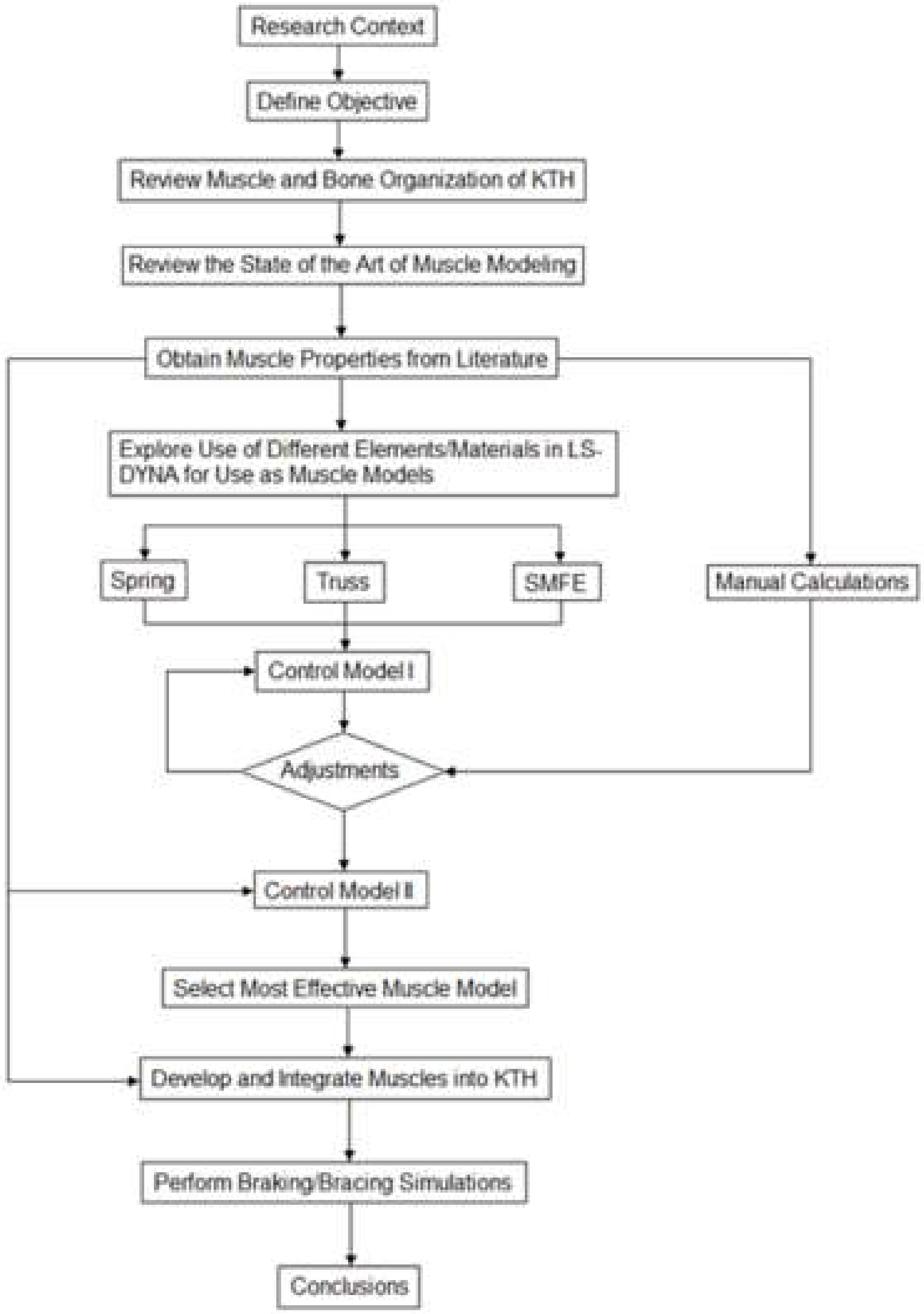

Figure 3.2. Flowchart of methodology.

IV. Architectural Properties of the Muscles of the Thigh

Physical and dynamic properties of the muscle groups of the thigh (previously listed in Table 1) were obtained from literature. These properties were required in order to develop and integrate FE models of muscle into the existing KTH model. These properties included the mass, density, optimal muscle length (L_o), muscle fiber length (FL), pennation angle (θ), PCSA, maximum contraction velocity (V_{max}), and peak isometric force (F_{max}) for each muscle. Additionally, the general locations of the origin and insertion points of each MTC on the associated bones along with their functions were obtained from literature.

The mass of a muscle is calculated by multiplying its volume by its density. The density of mammalian muscle is usually taken to be approximately 1.056 g/cm^3 (Lieber, 2002). The muscle volume is determined by a number of factors including fiber length and PCSA.

It is noted that the fiber length differs from the muscle length (ML). The fiber length is the length of each cylindrical multinucleate muscle cell. The optimal fiber length refers to the mean length of muscle fiber when the sarcomeres are at a length capable of producing maximal contractile force. The muscle length, on the contrary, refers to the length of the overall muscle. The optimal fiber length is coupled to the optimal muscle length (L_o) at which the force generating potential of the muscle is at its maximum. The ratio of muscle fiber length to muscle length (FL / ML) typically ranges from 0.2 to 0.6 (Lieber, 2002). The muscle force being generated at any given time is dependent upon the muscle length and is described by a F(L) function.

The angle at which the muscle fibers are aligned relative to the longitudinal axis (also called the force-generating axis) of the muscle was previously referred to as the pennation angle. There exist three general types of muscles organized according to the fiber pennation angle (Lieber, 2002). Muscles in which all the fibers are oriented in the same direction as the force-generating axis are called longitudinally arranged muscles. Muscles with fibers which are all oriented at the same angle (normally ranging from 0^o to 30^o) relative to the force-generating axis are called unipennate muscles. Finally, muscles with fibers oriented in multiple directions are called multipennate muscles. Figure 4.1 illustrates examples of these three muscle types.

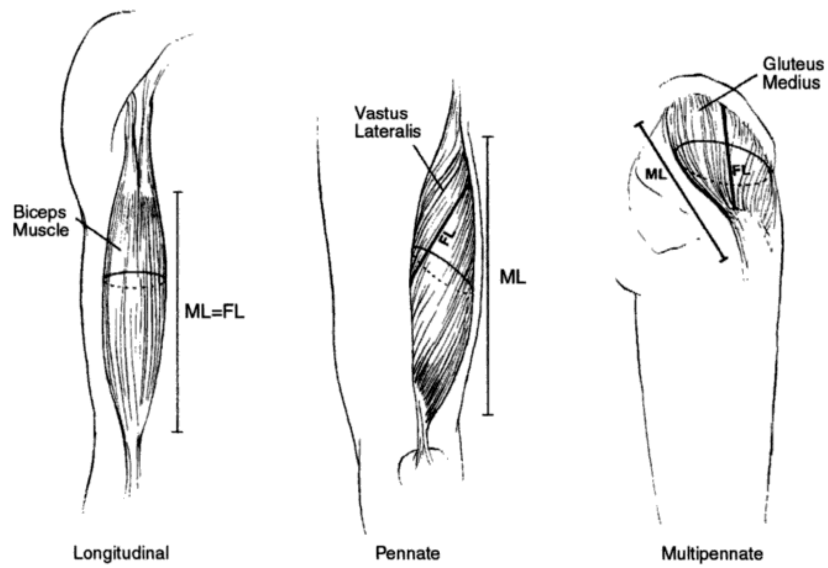

Figure 4.1. Muscle types organized according to pennation angle (Lieber, 2002).

The PCSA and muscle fiber length are two important geometrical parameters concerning the functioning of muscles. The PCSA actually refers to the cross sectional area of the plane perpendicular to the muscle fibers since the fibers' orientation may be slightly different from the longitudinal axis of the muscle (pennation angle). It is known that the force in a muscle is proportional to its PCSA. Furthermore, excursions by a muscle are proportional to its fiber length. It is found, then, that muscles with large PCSAs and short FLs (i.e. quadriceps femoris) are capable of generating large contractile forces but small excursions. On the contrary, muscles with small PCSAs and long FLs (i.e. posterior muscles) are capable of large excursions but small forces (Lieber, 2002).

The contraction velocity of muscle fibers (V_f) is the same as the contraction velocity of muscle along its force-generating axis (V_m) for longitudinally arranged muscles because of a pennation angle of 0^o. However, V_f differs from V_m for unipennate and multipennate muscles. It can be deduced that the muscle contraction velocity, fiber contraction velocity, and pennation angle (θ) are related by the following equation:

$$V_m = V_f \cos \theta \qquad (3)$$

The maximum fiber contraction velocity of muscle ($V_{f\text{-}max}$) is usually taken to be 2 muscle lengths per second for slow fibers and 8 muscle lengths per second for fast fibers (Olivetti, 2006). The maximum contraction velocity of muscle along the force-generating axis

(V_{max}) may be calculated by simply substituting $V_{f\text{-}max}$ for V_f in (3). The muscle force being generated at any given time is dependent upon the contraction velocity and is described by a F(V) function.

The force generated by muscle fibers (F_f) is dependent upon the activation level of muscle, as well as the muscle length and contraction velocity. It was previously mentioned that the accommodation of muscle length and contraction velocity produces a three-dimensional force-velocity-length function. It is noted that for longitudinally arranged muscles F_f is the same as the force generated by the muscle (F_m) due to a pennation angle of 0^o. F_f differs from F_m for unipennate and multipennate muscles because of varying pennation angles. It can be deduced that the value of F_f at any given time is calculated by taking the product of the PCSA and a stress constant s. This outcome is in turn multiplied by the output of the three-dimensional normalized generic force-velocity-length function. Finally, this outcome is scaled by multiplying it by the normalized A(t) output as shown in equation (4). F_m is then obtained by multiplying F_f by the cosine of the pennation angle as shown in equation (5):

$$F_f = A(t) \cdot F(V, L) \cdot s \cdot PCSA \qquad (4)$$

$$F_m = \cdot F_f \cdot \cos\theta \qquad (5)$$

It is important to note that the function F(V, L) outputs the normalized muscle fiber force at a contraction velocity V_f / $V_{f\text{-}max}$ and a muscle length ML / L_o. A(t) is the normalized activation ranging from 0 to 1. The constant s represents typical values of stress induced within activated mammalian skeletal muscle and ranges from 20 – 40 N/cm^2 with a median value of approximately 25 N/cm^2 (Kumar, 2004). The peak isometric force (F_{max}) may be calculated by simply inputting a full activation level for A(t) (i.e. 1) and setting F(V, L)= 1.

The architectural properties of the muscle groups of the thigh are outlined in Table 4.1. The maximum contraction velocities were calculated with equation (3) using a maximum fiber contraction velocity of 5 muscle lengths per second The peak isometric forces for each muscle were calculated with equations (4) and (5) using an s value of 25 N/cm^2. The locations of the origin and insertion points for each muscle as well as their functions are summarized in Table 4.2.

Table 4.1. Architectural properties of the muscle groups of the thigh (Lieber, 2002).

Muscle	Mass (g)	FL (cm)	L_o (cm)	Pennation angle (˚)	PCSA (cm^2)	V_{max} (cm/s)	F_{max} (N)
Adductor magnus	229	11.5	30.5	0.0	18.2	152.50	455.00
Adductor longus	63.5	10.8	22.9	6.0	6.8	113.87	169.07
Adductor brevis	43.8	10.3	15.6	0.0	4.7	78.00	117.50
Pectineus	26.4	10.4	12.3	0.0	2.9	61.50	72.50
Gracilis	35.3	27.7	33.5	3.3	1.8	167.22	44.93
Sartorius	61.7	45.5	50.3	0.0	1.7	251.50	42.50
Rectus femoris	84.3	6.6	31.6	5.0	12.7	157.40	316.29
Vastus lateralis	220	6.57	32.4	5.0	30.6	161.38	762.09
Vastus medialis	175	7.03	33.5	5.0	21.1	166.86	525.49
Vastus intermedius	160	6.83	32.9	3.3	22.3	164.23	556.58
Biceps femoris	128	8.53	34.2	0.0	12.8	171.00	320.00
Semitendinosus	76.9	15.8	31.7	5.0	5.4	157.90	134.49
Semimembranosus	108	6.27	26.2	15	16.9	126.54	408.10

Table 4.2. Locations of origin/insertion points and functions of muscles of the thigh (University of Washington Radiology, 2008).

Medial compartment		
Adductor magnus 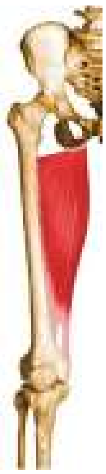	<u>Origin</u> Inferior pubic ramus, ischial ramus, and inferolateral area of ischial tuberosity <u>Insertion</u> Gluteal tuberosity of femur, medial lip of linea aspera, medial supracondylar ridge, and adductor tubercle	<u>Functions</u> Powerful thigh adductor; superior horizontal fibers also help flex the thigh, while vertical fibers help extend the thigh
Adductor longus 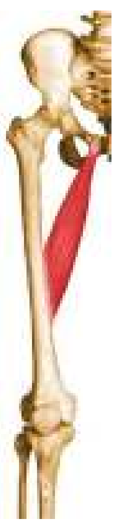	<u>Origin</u> Anterior surface of body of pubis, just lateral to pubic symphysis <u>Insertion</u> Middle third of linea aspera, between the more medial adductor magnus and brevis insertions and the more lateral origin of the vastus medialis	<u>Functions</u> Adducts and flexes the thigh, and helps to laterally rotate the hip joint
Adductor brevis 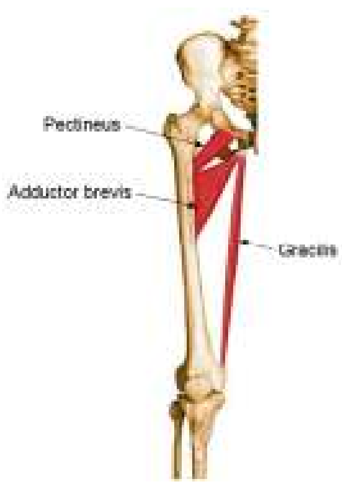	<u>Origin</u> Anterior surface of inferior pubic ramus, inferior to origin of adductor longus <u>Insertion</u> Pectineal line and superior part of medial lip of linea aspera	<u>Functions</u> Adducts and flexes the thigh, and helps to laterally rotate the thigh

Medial compartment		
Pectineus 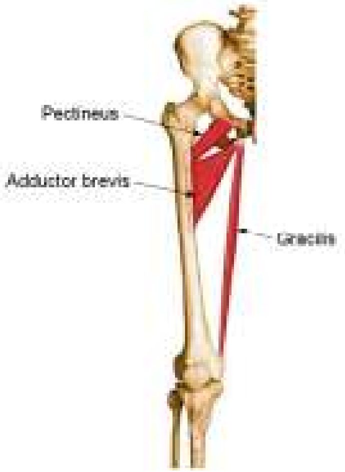	<u>Origin</u> Pecten pubis and pectineal surface of the pubis <u>Insertion</u> Pectineal line of femur	<u>Functions</u> Adducts the thigh and flexes the hip joint
Gracilis 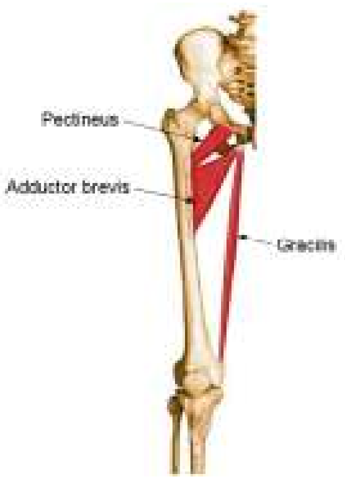	<u>Origin</u> Inferior margin of pubic symphysis, inferior ramus of pubis, and adjacent ramus of ischium <u>Insertion</u> Medial surface of tibial shaft, just posterior to sartorius	<u>Functions</u> Flexes the knee, adducts the thigh, and helps to medially rotate the tibia on the femur

Anterior compartment		
Sartorius 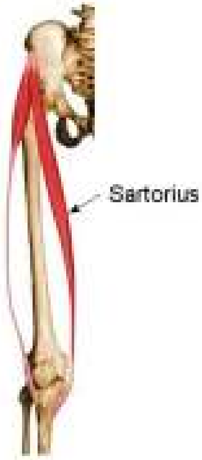 	<u>Origin</u> Anterior superior iliac spine <u>Insertion</u> Superior aspect of the medial surface of the tibial shaft near the tibial tuberosity	<u>Functions</u> Flexes and laterally rotates the hip joint and flexes the knee
Rectus femoris 	<u>Origin</u> Straight head from anterior inferior iliac spine; reflected head from groove just above acetabulum <u>Insertion</u> Base of patella to form the more central portion of the quadriceps femoris tendon	<u>Functions</u> Extends the knee
Vastus lateralis 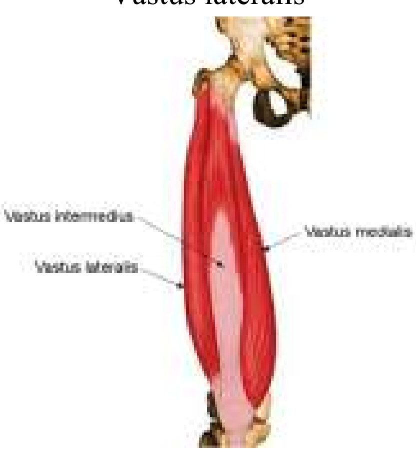 	<u>Origin</u> Superior portion of intertrochanteric line, anterior and inferior borders of greater trochanter, superior portion of lateral lip of linea aspera, and lateral portion of gluteal tuberosity of femur <u>Insertion</u> Lateral base and border of patella; also forms the lateral patellar retinaculum and lateral side of quadriceps femoris tendon	<u>Functions</u> Extends the knee

Anterior compartment		
Vastus medialis 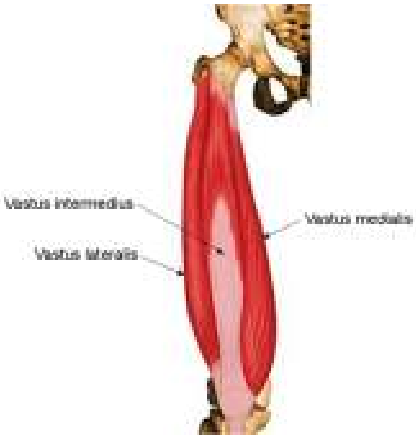	<u>Origin</u> Inferior portion of intertrochanteric line, spiral line, medial lip of linea aspera, superior part of medial supracondylar ridge of femur, and medial intermuscular septum <u>Insertion</u> Medial base and border of patella; also forms the medial patellar retinaculum and medial side of quadriceps femoris tendon	<u>Functions</u> Extends the knee
Vastus intermedius 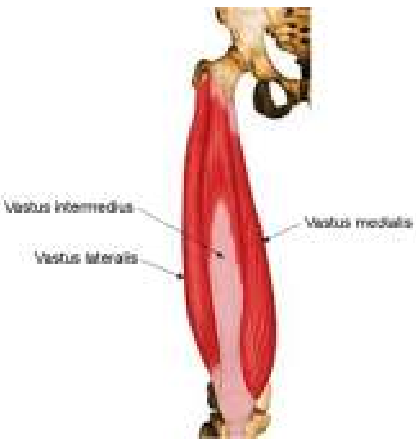	<u>Origin</u> Superior 2/3 of anterior and lateral surfaces of femur; also from lateral intermuscular septum of thigh <u>Insertion</u> Lateral border of patella; also forms the deep portion of the quadriceps tendon	<u>Functions</u> Extends the knee

Posterior compartment		
Biceps femoris 	<u>Origin</u> Common tendon with semitendinosus from superior medial quadrant of the posterior portion of the ischial tuberosity <u>Insertion</u> Primarily on fibular head; also on lateral collateral ligament and lateral tibial condyle	<u>Functions</u> Flexes the knee, and also rotates the tibia laterally; long head also extends the hip joint
Semitendinosus 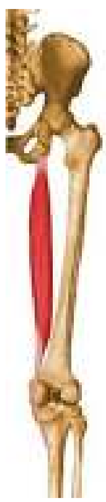	<u>Origin</u> From common tendon with long head of biceps femoris from superior medial quadrant of the posterior portion of the ischial tuberosity <u>Insertion</u> Superior aspect of medial portion of tibial shaft	<u>Functions</u> Extends the thigh and flexes the knee, and also rotates the tibia medially, especially when the knee is flexed
Semimembranosus 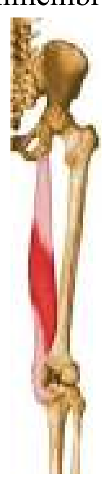	<u>Origin</u> Superior lateral quadrant of the ischial tuberosity <u>Insertion</u> Posterior surface of the medial tibial condyle	<u>Functions</u> Extends the thigh, flexes the knee, and also rotates the tibia medially, especially when the knee is flexed

V. Development of Muscle Models

This section outlines the utilization of the finite element software LS-DYNA to develop and simulate FE models as well as the process used in developing an improved FE muscle model.

5.1 Implementation in LS-PrePost and LS-DYNA

LS-DYNA is a powerful tool for developing and conducting finite element analyses. Its enormous capability is drawn from its extensive array of material types and calculation routines. Over the past few decades, LSTC has continuously developed and added new capabilities to the software such as new material models and element types (LSTC, 2007). The resources offered by LS-DYNA allow for extremely complex systems such as vehicles or musculo-skeletal models to be developed, simulated, and analyzed in great detail.

Perhaps the greatest challenge in conducting FE analyses with LS-DYNA is the actual development of a model and getting it to run without errors. The process of developing a FE muscle model was no exception. The physical and dynamic properties of the muscle groups of the thigh had to be brought from idealization to realization. This process involved experimentation with various element types and material models so as to develop a FE muscle model that correlated to the properties and behaviors of real muscle. The most accurate and effective combination was then further refined into a final FE muscle model. These steps required an interface through which the known properties of muscle could be input and simulated. LS-PrePost is a tool that serves as this interface and was used in conjunction with LS-DYNA in order to create and edit FE models.

All of the work performed on a FE model in LS-PrePost is stored in a file with a .k file extension. The .k file may then be opened using LS-PrePost or a text editor. Opening the .k file using LS-PrePost allows editing of the model to be performed on a graphical interface. The geometry and non-geometric properties of a model may be viewed and edited as desired. Opening the .k file using a text editor allows for more detailed editing of the model to be performed.

The geometric and non-geometric properties of a FE model in LS-PrePost and LS-DYNA are defined by components called cards (Figure 5.1). Each card consists of a group of text characters which require a specific format in which geometric and non-geometric properties of a model may be input. These cards may be added or edited using LS-PrePost or a text editor as previously described. When used correctly, the cards provide information for LS-DYNA to perform numerical calculations on the model. The duration of time that LS-DYNA requires to perform the FE analysis depends upon the complexity of the model and the speed of the computer that is running the simulation.

```
*PART
$# title
spring_muscle
$#     pid     secid       mid     eosid      hgid      grav    adpopt      tmid
         3         2         5         0         0         0         0         0
```

Figure 5.1. Example of a *PART card. The input location "pid" refers to the part identification number, "secid" references the section identification card, and "mid" references the material identification card.

As the simulation is running, LS-DYNA outputs files called d3plots. The d3plots contain results at specific incremental states of the model from the FE analysis. These files may then be opened using LS-PrePost from which an animation of the model may be viewed. Furthermore, results such as stresses, forces, displacements, velocities, etc. may be acquired from the d3plots.

The geometry of a typical FE model consists of nodes of which are assigned unique position coordinate values. The nodes, in turn, are assigned to elements which collectively form a solid or shell mesh. The mesh, in turn, defines the basic geometry of a model. One-dimensional discrete elements or beam elements may be defined by nodes as well. Non-geometrical properties (i.e. density, elastic modulus, initial velocity, contact, etc.) may then be assigned to the geometric properties. This is all accomplished through the utilization of cards. A FE model may then be completely developed and simulated by utilizing LS-PrePost, a text editor, and LS-DYNA.

Consistent units are required in LS-DYNA. For this research, units of length were measured in millimeters (mm), units of time were measured in seconds (s), units of mass were measured in tons (1000 kg), and units of force were measured in Newtons (N).

LS-DYNA version 971 was used for running all the simulations for this research. The computers used for the simulations were "Sunfire X2200M series" with two dual core AMD Opteron 2220 2.8 GHz CPUs and 12 GB of RAM. (Silvestri, 2008) The time step utilized was 5.00e-7 seconds. The computation duration ranged anywhere from two to 24 hours depending upon the complexity of the simulation.

5.2 Evaluation of Three Different Muscle Models

Three different muscle models were evaluated based upon their conformity to the properties and behavior of mammalian skeletal muscle. Two different FE control models were developed in LS-DYNA to provide settings on which the three muscle models could be evaluated on an equal basis. The most accurate and effective muscle model was then selected for further development.

5.2.1 Control Model I

The specific purpose of the first control model was to compare the properties and behavior of the three different FE muscle models to the properties and behavior of mammalian skeletal muscle. It is nearly impossible to completely isolate and obtain the properties and behavior of a single active muscle (Siegmund et al., 2007). Therefore, manual calculations were performed in order to obtain results that could be compared to the FE muscle model results. This was done with the presumption that the results from the manual calculations most closely represented the behavior of a single active muscle.

The control model resembled a general undamped single-degree-of-freedom (SDOF) spring-mass system. One control model was constructed for each of the three muscle models. For each control model, the muscle model of interest was attached to a fixed anchor plate on one end and attached to a 2 kg mass on the other end as shown in Figure 5.2. The 2 kg mass was arbitrarily chosen to represent an object that the muscle could perform work on. The mass was free to move only along the longitudinal axis of the muscle model and its movement was dependent upon the contractile behavior of the muscle model. The material of the anchor plate and mass was modeled as steel with elastic properties. The fineness of the mesh used for the anchor plate and mass was selected based on the specific purpose of the control model. A uniform mesh with medium fineness was deemed to be acceptable since the parameters being tested pertained strictly to the muscle model and not to the anchor plate or mass. A series of trials demonstrating the muscle contraction were then performed for each muscle model.

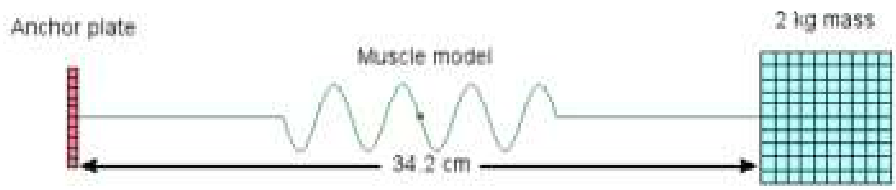

Figure 5.2. Profile view of Control Model I.

The first muscle model selected for evaluation was a discrete one-dimensional Hill-based spring element coupled with Material Type 15. A single spring element was utilized to model a single MTC. This model allowed for the input of initial muscle length, maximum shortening velocity, and peak isometric force. Additionally, generic F(V) and F(L) curves, along with a custom A(t) curve, were referenced which then governed the contractile behavior of the model.

The second muscle model selected for evaluation was a one-dimensional truss element (beam element) used in conjunction with Material Type 156. As with the spring element, a single truss element was typically utilized to model each MTC. This model allowed for the input of muscle density, cross-sectional area, initial stretch ratio, maximum strain rate, peak isometric stress, and a damping constant. Additionally, F(V), F(L), and A(t) curves were referenced accordingly.

The third muscle model selected for evaluation was an SMFE shell element model. SMFE shell element models utilize 2D shell elements in combination with one-dimensional contractile elements in series and parallel. A similar SMFE combination was previously developed by Hedenstierna (2008) in a 3D solid element muscle model. Shell elements were utilized instead of solid elements due to the substantial decrease in complexity in forming general muscle geometry. This is because it is extremely difficult to construct 3D structures in LS-PrePost without expending considerable amounts of time. The shell elements possessed hypo-elastic properties while the 1D elements were truss elements. Three shell muscle models with varying levels of mesh complexity were tested. The first shell model consisted of four shell elements in parallel with four truss elements. The second shell model contained two serial sets of four shell and truss elements in parallel. The third shell model contained six serial sets of four shell and truss elements in parallel.

The configurations of the spring and truss element control models are shown in Figure 5.3. The configurations of the three shell element control models are shown in Figure 5.4.

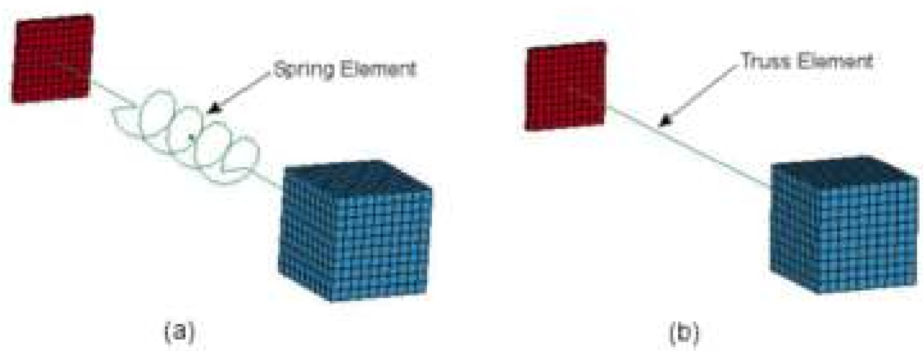

Figure 5.3. Configurations of the (a) spring and (b) truss element control models.

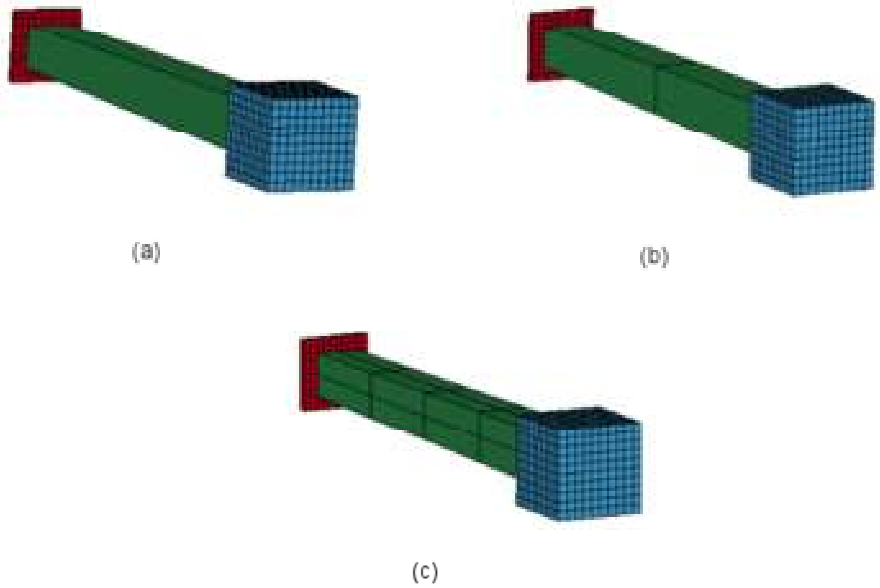

Figure 5.4. Configurations of the (a) first, (b) second, and (c) third shell element models.

The primary factors for comparing the behavior of the muscle models to skeletal muscle were the contraction velocities and muscle forces. Specifically, the resultant velocities, V(t), of the insertion point on the mass in each of the FE simulations was compared to manually calculated resultant velocity values of the insertion point on the mass in a similar undamped SDOF spring-mass configuration. V(t) was equivalent to the contraction velocity because the origin of the muscle, located on the anchor plate, was fixed while the insertion point was free to move through space depending upon the contractile behavior of the muscle model. Similarly, the resultant muscle forces, F(t), in each of the FE simulations was compared to manually calculated resultant muscle forces in a similar undamped SDOF spring-mass configuration. It is important to note that identical A(t) curves were utilized for both the FE analyses and the corresponding manual calculations.

In a real configuration, the contraction velocity partially depends upon the neural activation level of muscle. However, as previously mentioned, it is nearly impossible to completely isolate and obtain the response of an individual active muscle through experiments. This was the primary reason for manually calculating the contraction velocities based upon the known properties of the muscle of interest as a means for comparing values. The properties for each FE muscle model were then adjusted accordingly in order to conform to the manually calculated velocity and force values. This was done under the presumption that the manual calculations most closely represented the behavior of a real muscle in a similar configuration. The enacted changes were documented and considered during the determination of the most accurate and effective muscle model.

The biceps femoris of the posterior compartment was chosen as the muscle of interest. Properties including mass, density, optimal muscle length, pennation angle, PCSA, maximum contraction velocity, and approximate peak isometric force were previously acquired for this muscle (Table 4.1). Also, normalized generic F(V) and F(L) curves were obtained from literature and were utilized throughout this research. A custom activation function, A(t), was formed and used for the analysis of the biceps femoris in both the manual calculations and the FE control model simulation. Electromyographic recordings performed by Siegmund et al. (2007) on neck muscles show that skeletal muscle activation levels may vary rapidly over short periods of time. For simplification purposes, steadily increasing activation curves were utilized throughout this research. The normalized generic F(V), F(L), and A(t) curves employed are shown in Figures 5.5, 5.6, and 5.7.

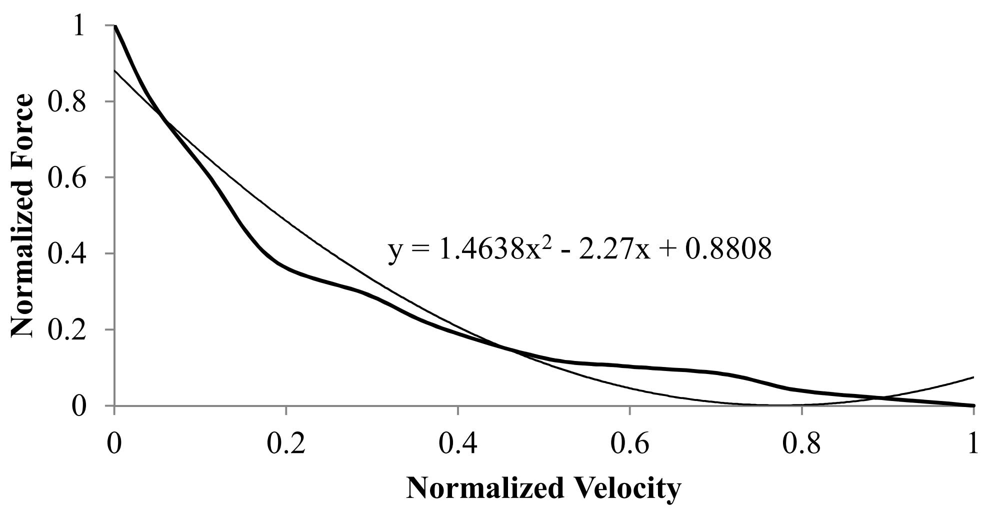

Figure 5.5. Normalized generic force-velocity curve.

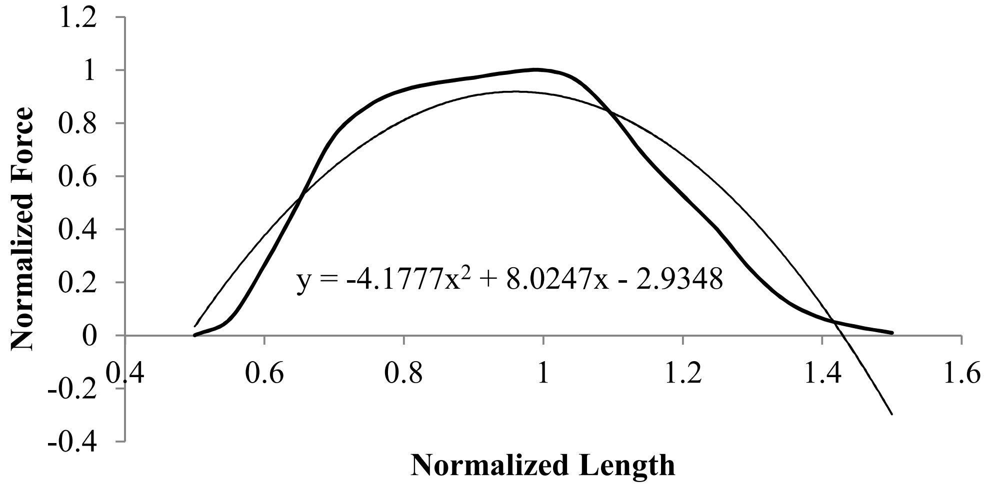

Figure 5.6. Normalized generic force-length curve.

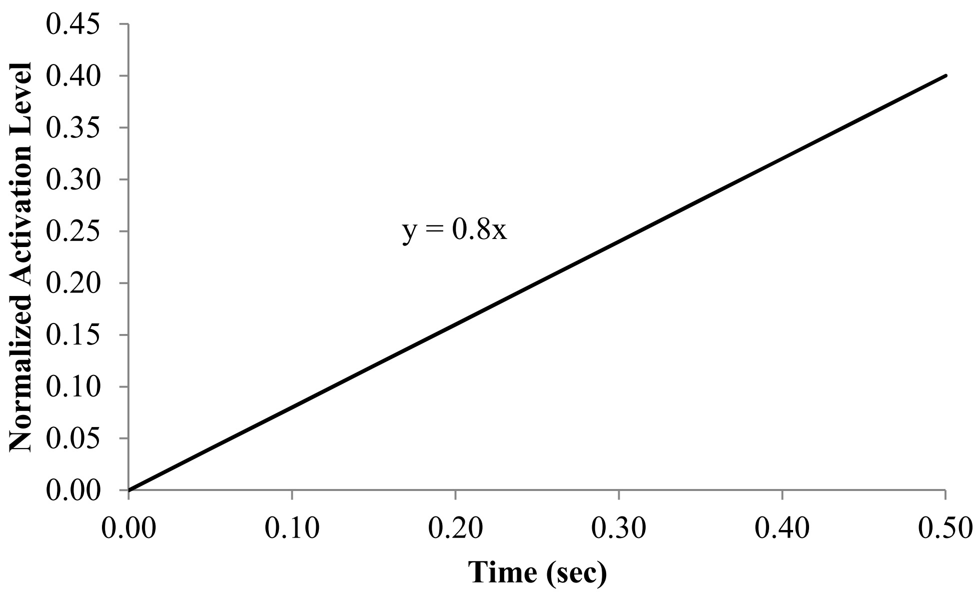

Figure 5.7. Normalized activation curve.

The properties of the biceps femoris as well as the F(V), F(L), and A(t) curves were input accordingly into each of the FE muscle models. It is noted that each of the muscle models accompanied different properties of the biceps femoris. For example, the truss model allowed for the PCSA to be input while the spring model did not. Several types of cards were utilized to define the parameters for each muscle model. Among these, the *SECTION_DISCRETE, *SECTION_BEAM, and *SECTION_SHELL cards were used to define the section properties of the spring, truss, and shell elements, respectively. The *DEFINE_CURVE card was used to define the F(V), F(L), and A(t) curves for each model. These properties, along with several other parameters, were consolidated and referenced accordingly in the *PART card for each model. Figure 5.8 displays the cards utilized to define some of the material properties for each model.

(a)
```
*MAT_SPRING_MUSCLE_TITLE
spring_muscle_material
$#     mid        lo      vmax        sv         a      fmax        tl        tv
         5       342      1710     0.000        -1       320        -2        -3
       0.0       0.9      4.00
```

(b)
```
*MAT_MUSCLE_TITLE
truss_muscle_material
$#     mid        ro       sno       srm       pis       ssm       cer       dmp
         5 1.056E-09       1.0         5      0.25       0.5         1         0
$      alm       sfr       svs        tv       ssp
        -1       1.0        -2        -3        -2
```

(c)
```
*MAT_OGDEN_RUBBER
$#     mid        ro        pr         n        nv         g      sigf
         2 1.056E-09       0.3         2         0
$#     sgl        sw        st     lcid1      data     lcid2    bstart     tramp
         4         2         2         1                   2
```

Figure 5.8. Material cards utilized for the (a) spring, (b) truss, and (c) shell element models.

It can be seen in the *MAT_SPRING_MUSCLE card that property inputs of the biceps femoris including optimal muscle length "lo", maximum contraction velocity "vmax", and maximum contractile force "fmax" were defined. Additionally, F(V), F(L), and A(t) curves were referenced under the "tv", "tl", and "a" input locations, respectively. The *MAT_MUSCLE card accommodated different material properties such as maximum strain rate "srm" and peak isometric stress "pis". The *MAT_OGDEN_RUBBER card for the shell material accommodated such parameters as Poisson's ratio. In all cases, the material density "ro" was set as the density of mammalian muscle, which is 1.056 g/cm^3, or 1.056 x 10^{-9} tons/mm^3.

Each of the FE muscle models were then simulated in LS-DYNA and the resulting contraction velocities and muscle forces over time were obtained from the analyses. The properties of the biceps femoris and the F(V), F(L), and A(t) curves were also used for manually calculating the contraction velocities and forces for the undamped SDOF spring-mass system.

The use of a shell element muscle model was subject to much preliminary experimentation. It was found that truss elements rather than spring elements provided the most stable SMFE combination. The formation of such a combination first involved the creation of a shell mesh shaped into the desired geometry. Much difficulty may be encountered in creating geometrically complex surfaces in LS-DYNA while retaining the fineness of a mesh. Hence, a relatively simple prismatic shape with a square cross section was utilized for the purpose of this control model. The fineness of mesh, then, was increased for each subsequent shell model as previously described instead of increasing the complexity of the geometry itself. Truss elements were then attached to the nodes in parallel and in series to each other along the longitudinal axis of the shell geometry. Each truss element was then assigned identical F(V), F(L), and A(t) curves. The detailed properties of each individual truss element (i.e. PCSA and Peak isometric stress) then depended upon the number of truss elements in a cross section of the overall shell muscle model. For example, in the first shell model the nominal PCSA of the biceps femoris was distributed equally among four truss elements since four truss elements pass through the cross section of the shell model at any given location. Different shell materials were then tested in order to determine which material provided the greatest stability to the shell during contraction.

Manual calculations were performed in order to obtain estimated contraction velocities and forces to compare to the FE control model results. It can be seen in Figures 5.5 and 5.6 that second order polynomial functions were fitted to the normalized F(V) and F(L) curves as shown in equations (6) and (7). The activation function is shown in equation (8).

$$F(V) = 1.464V^2 - 2.27V + 0.881 \qquad (6)$$

$$F(L) = -4.18L^2 + 8.02L - 2.93 \qquad (7)$$

$$A(t) = 0.8t \qquad (8)$$

Equations F(V) and F(L) were combined by taking the product of the two to form a normalized generic three-dimensional force-velocity-length function denoted by F(V, L) shown in equation (9). F(V,L) is shown plotted in Figure 5.9. It can be seen from the plot that inputting values of muscle length and contraction velocity into F(V,L) outputs a corresponding value of muscle force.

$$F(V,L) = -6.12V^2L^2 + 11.74V^2L - 4.29V^2 + 9.49VL^2 - 18.21VL + 6.65V - 3.68L^2 + 7.07L - 2.58 \quad (9)$$

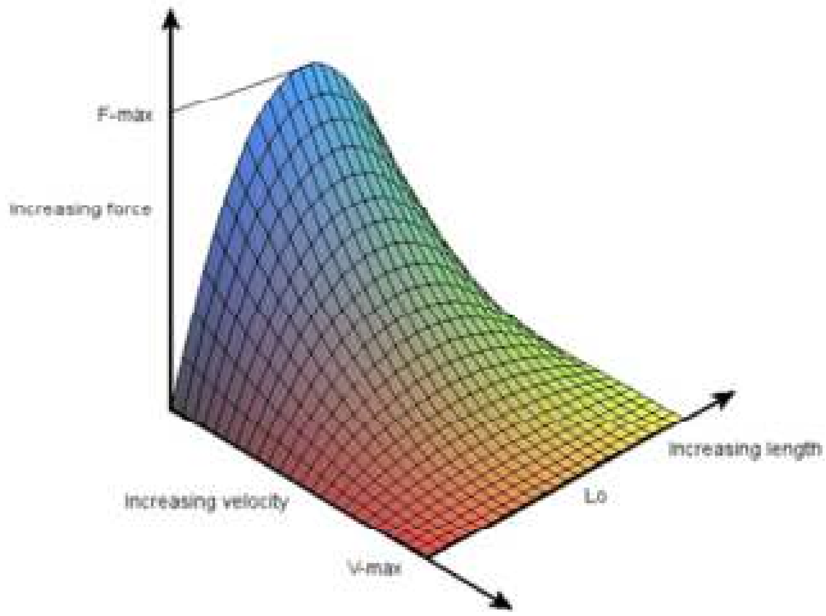

Figure 5.9. Plot of normalized generic three-dimensional force-velocity-length function.

The behavior of the biceps femoris was modeled as an undamped single-degree-of-freedom (SDOF) spring-mass system as shown in Figure 5.10. A characteristic equation of motion for the contraction of the muscle was developed and solved for by using the constant velocity method (Biggs, 1964). This method is typically utilized for dynamic analysis of tall buildings. However, it may be applied to simplified spring-mass systems such as this case. The resulting contraction velocities and muscle forces over time were then obtained from the analysis.

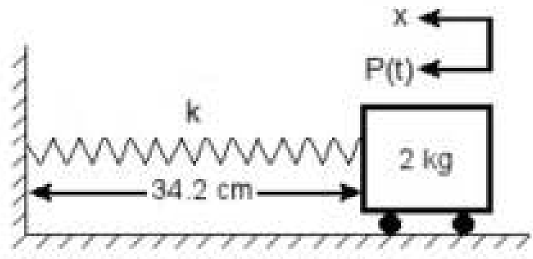

Figure 5.10. Undamped SDOF spring-mass system.

The equation of contractile motion of the biceps femoris was found by taking into account the mass, stiffness, and forcing function,

$$m \cdot x'' + k \cdot x = P(t, x', L) \qquad (10)$$

where x" is the contractile acceleration, x' is the contractile velocity, and x is the displacement of the end of the muscle from its initial length (in this case, the initial length was presumed to be the optimal length, L_o). It is important to note that the mass, m, included both the mass of the muscle and the 2 kg mass. Realistically, a varying portion of the mass of the muscle contributes to the muscle force. The stiffness, k, is the approximate axial stiffness of the muscle and varied depending upon the length of the muscle. The forcing function, P(t, x', L), is the muscle force generated depending upon the activation, contractile velocity, and muscle length.

As previously mentioned, muscle tissue is nonhomogeneous and exhibits nonlinear material behavior. However, for the purpose of simplifying the manual calculations, the muscle material was modeled as a uniform linearly elastic material. With this taken into account, the axial stiffness of the biceps femoris was given by,

$$k = (PCSA \cdot E) / L \qquad (11)$$

and the length of the muscle, L, in terms of the optimal length and change in length at any time was given by:

$$L = L_o - x \qquad (12)$$

Finally, the forcing function, $P(t, x', L_o - x)$, was formed by combining equations (4), (5), and (12):

$$P(t, x', L_o - x) = A(t) \cdot F(x', L_o - x) \cdot s \cdot PCSA \cdot \cos\theta \qquad (13)$$

The contractile acceleration, given by equation (14), was found by rearranging equation (10). By substituting equations (11), (12), and (13) into equation (14), equation (15) was formed:

$$x'' = (P(t) / m) - (k / m) \cdot x \qquad (14)$$

$$x'' = [(A(t) \cdot F(x', L_o - x) \cdot s \cdot PCSA \cdot \cos\theta) / m] - [(PCSA \cdot E) / (m \cdot (L_o - x))] \qquad (15)$$

By specifying an initial muscle length and a presumed initial contraction velocity, the contraction velocities and muscle forces over time were obtained by applying the constant velocity method to solve the equation of motion. The muscle force at each time step was dependent upon the activation level as well as the muscle length and velocity from the previous time step. The muscle force then defined a new muscle length and velocity depending upon the stiffness of the muscle, which then defined the muscle force for the subsequent time step. This cycle was repeated by utilizing a spreadsheet program. The iterations were performed until the amount of contraction velocity and muscle force data was deemed reasonable to compare to the FE analyses results. A schematic of the iterative process is shown in Figure 5.11.

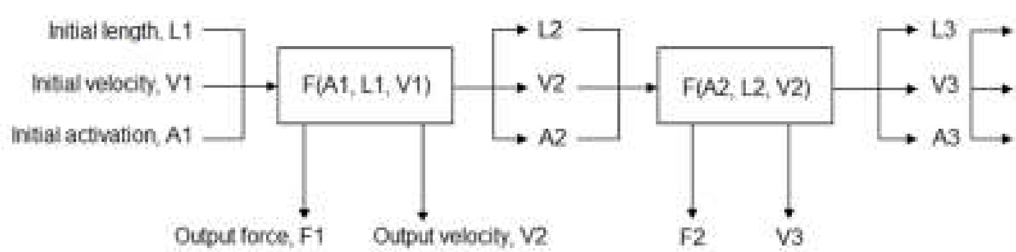

Figure 5.11. Schematic of iterative process.

Table 5.1 shows the properties of the biceps femoris along with the properties accommodated by each of the FE muscle models prior to any adjustments as well as the SDOF spring-mass system. Figure 5.12 displays the plots of the resulting contraction velocities over time for each of the muscle models as well as from the manual calculations. Figure 5.13 displays the plots of the muscle forces over time for each of the analyses as well as from the manual calculations. Data was obtained over a time ranging from 0 to 0.25 seconds. Results from the third shell model were excluded because it was deemed to be too unstable for any practical use.

Table 5.1. Initial properties of muscle models (Lieber, 2002).

Property	Biceps Femoris	Spring	Truss	Shell 1	Shell 2	Shell 3	Spring-Mass System
Mass (g)	128	-	-	125	125	125	128
Density (g/cm^3)	1.056	-	1.056	1.056	1.056	1.056	-
L_o (cm)	34.2	34.2	-	-	-	-	34.2
Pennation angle (˚)	0	-	-	-	-	-	0
PCSA (cm^2)	12.8	-	12.8	12.8	12.8	12.8	12.8
V_{max} (cm/s)	171	171	-	-	-	-	171
Maximum strain rate (s^{-1})	5	-	5	5	5	5	-
F_{max} (N)	320	320	-	-	-	-	-
Peak isometric stress (N/cm^2)	25	-	25	25	25	25	-

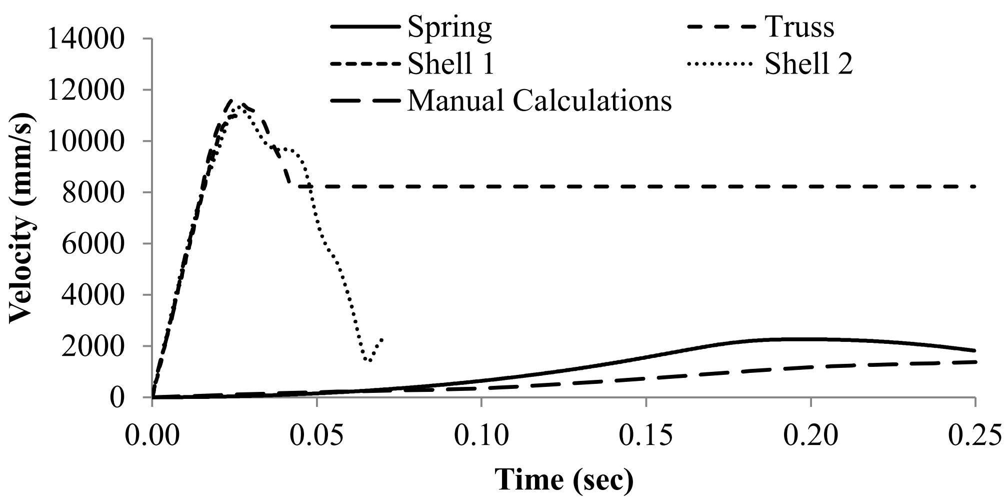

Figure 5.12. Contraction velocities of all muscle models and from manual calculations.

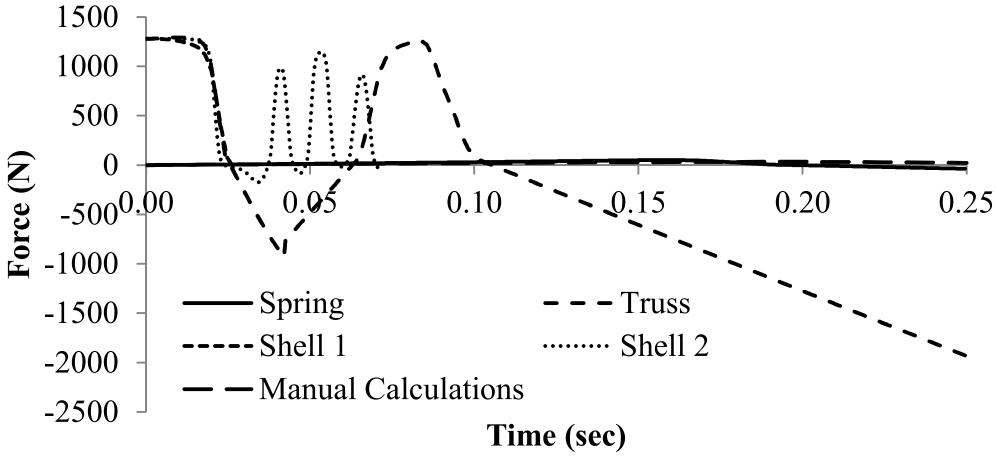

Figure 5.13. Contractile forces of all muscle models and from manual calculations.

The most outstanding differences between the spring and truss element models were that the truss element model produced much greater contraction velocities and muscle forces than the spring element model. The spring element model contracted for approximately 0.25 seconds before the FE model failed while the truss element model contracted for approximately 0.025 seconds before failure. Upon activation, the contraction velocity of the spring element model steadily rose to a peak of 2.25 m/s about 0.2 seconds after activation before it steadily decreased. The contraction velocity of the truss element model rose linearly to a peak of 11 m/s before the FE model failed at 0.025 seconds after activation. In this respect, the contractile velocity function of the spring element model most closely matched the contractile velocity function from the manual calculations without any adjustments being made to the original properties of the spring element model. However, it was found that the original properties of the of the truss element model could be adjusted to better conform to the manual calculations results.

The spring element model produced a contractile force which steadily rose to 50 N about 0.17 seconds after activation before it quickly fell to zero at 0.2 seconds after activation. The truss element model immediately produced a constant contractile force of 1250 N which gradually fell to zero between 0.02 and 0.025 seconds after activation. As in the previous case, the contractile force function of the spring element model most closely matched the contractile force function from the manual calculations without any adjustments being made to the original properties of the spring element model. Again, the original properties of the truss element model could be appropriately adjusted to output a matching contractile force function. Figure 5.14 demonstrates the contraction of the spring and truss element models.

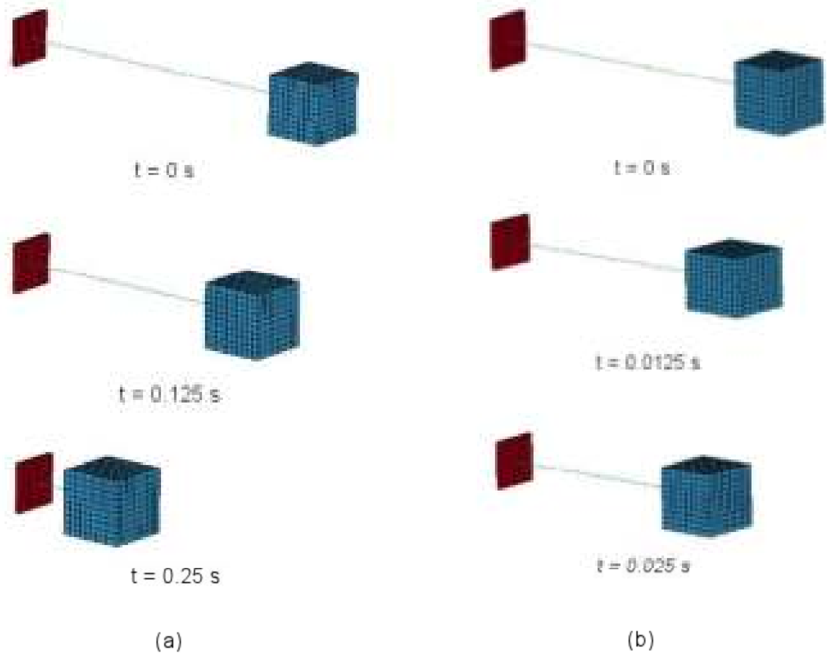

Figure 5.14. Contraction of spring and truss element models.

It was concluded that the SMFE combination using shell and truss elements was the most effective muscle model. Using shell and spring elements produced unstable model behavior. The first and second shell muscle models proved to be much more stable than the third shell muscle model which possessed a more refined mesh along with more truss elements. During simulations the third shell muscle model exhibited extremely unstable behavior in that the contracting truss elements caused the shell material to tear apart immediately after initial activation (Figure 5.15). Therefore, the behaviors and implications of the first and second shell muscle models are primarily discussed.

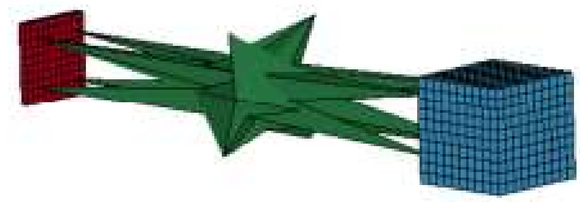

Figure 5.15. Failure of third shell element muscle model.

Material Type 77 (Ogden rubber) and Material Type 1 (elastic material) were primarily tested for use as the shell material. It was concluded that these two materials enabled the most stable muscle behavior. Figures 5.12 and 5.13 displays results for the shell element models utilizing Ogden rubber. The results for the shell elements utilizing elastic material are not shown because the results are nearly identical to the results utilizing Ogden rubber. The Ogden rubber material defined in LS-DYNA possesses hyperelastic and viscoelastic properties thus making it more suitable for replicating the physical properties of muscle (Hedenstierna, 2008). The elastic material is isotropic which contradicts the fact that mammalian skeletal muscle is nonhomogeneous. However, the resulting dynamic behavior of the SMFE model including contraction velocity and force was deemed to be more important than the physical properties of the model. Therefore, the use of elastic material for the shell material was judged to be acceptable. It was plausible that the Ogden and elastic material could be utilized interchangeably. Figure 5.16 shows the contraction of the first shell element model utilizing Ogden rubber as the shell material.

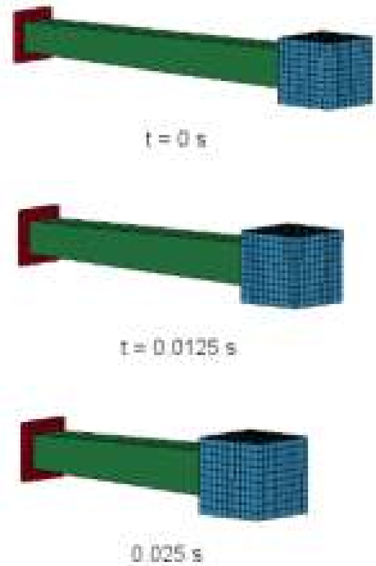

Figure 5.16. Contraction of first shell element model.

The SMFE combination allowed for considerable flexibility in terms of adjusting muscle activation, length, contraction velocity, and force. The initial biceps femoris properties that were input into the first and second shell muscle models (Table 5.2) output resulting contraction velocities and forces that differed from the manual calculation results (Figures 5.12 and 5.13). The contraction velocities of the first and second shell element models are nearly identical to each other and to the contraction velocities of the truss element model, but are approximately 100 times greater than values obtained from the manual calculations. Additionally, the contractile forces produced by both shell element models are nearly identical to each other and to the truss element model, but are approximately 10 times greater than the force values obtained from the manual calculations. These properties were adjusted appropriately for both Ogden rubber and the elastic material to output results approximating the manual calculation results and were retained for use in subsequent muscle models (presuming the adjustments are generally the same for different muscles).

Specifically, for both Ogden rubber and elastic material the defined PCSA of each truss element was decreased 50-fold from 3.2 cm^2 (recall that a total PCSA of 12.8 cm^2 distributed equally among four truss elements is 3.2 cm^2) to 0.06 cm^2 in order to significantly lower the contraction velocities and forces of the shell element models to approximately match the manual calculations. Hence, the total truss PCSA required for any subsequent shell element model using

Ogden rubber or elastic material should be approximately 1/50 that of the actual PCSA of the muscle being modeled. Figures 5.17 and 5.18 show the resulting contraction velocities and forces for the first shell element model using Ogden rubber as the shell material after modifications. Although the reduction in total truss PCSA allowed the resulting behavior of the SMFE combination to conform much better to the manual calculations results, the differences between the two results were still evident in the initial influence of the activation levels. The initial SDOF spring-mass behavior appeared to conform to the influence of the activation curve, while the initial SMFE behavior seemed to be influenced much less by its corresponding activation curve. For example, the contractile force value induced by the truss elements was initially nonzero even though the activation level started off at zero. This unresolved behavior was presumably due to a preload force inherent to the properties of the truss elements. However, due to the conformity of the SMFE behavior to the SDOF spring-mass behavior in terms of scaling and peak values, the unresolved issue pertaining to initial activation behavior was deemed to be minor since this research focused upon the preload force of muscle at full activation.

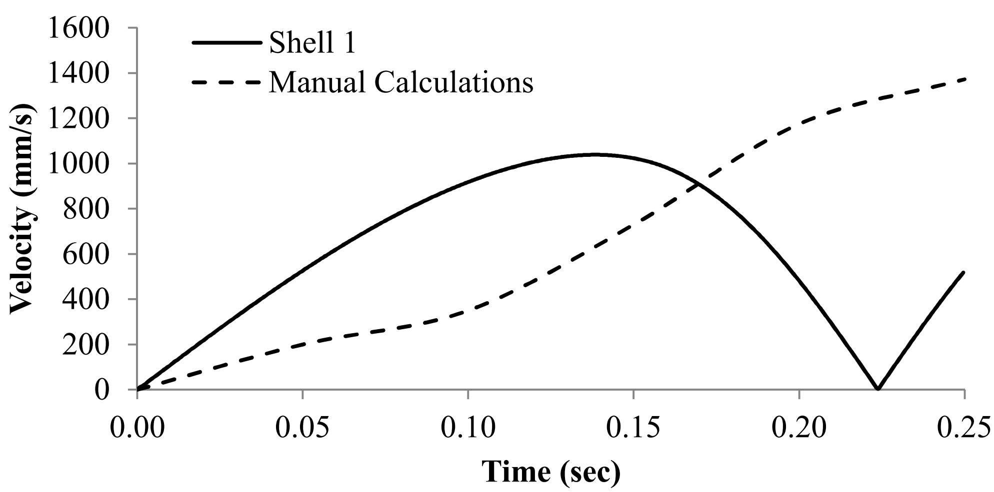

Figure 5.17. Contraction velocities of first shell element model after modifications and from manual calculations.

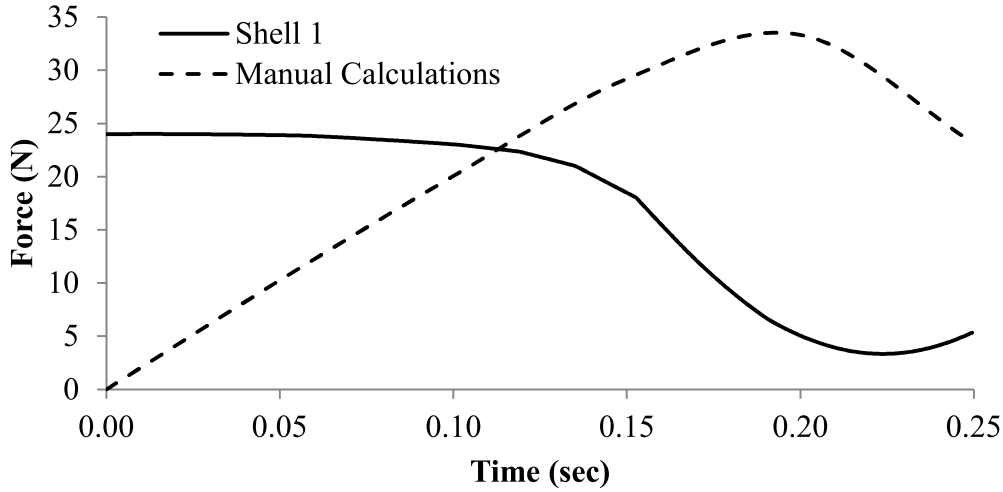

Figure 5.18. Contractile forces of first shell element model after modifications and from manual calculations.

Other advantages of the SMFE combination are that the use of shells allows for the inclusion of muscle mass and indirect lines of action. For example, a muscle that crosses a joint could potentially be modeled by first creating the nonlinear shell structure in the approximate shape of the muscle, and then integrating truss elements in series and parallel. Furthermore, the SMFE combination allows for more realistic origin and insertion points to be simulated since the projection of the shell on a bone surface produces stresses (albeit non-uniform) over a greater region than a single point produced by a 1D element. These advantages were further built upon and demonstrated in the second control model.

5.2.2 Control Model II

The second control model provided a highly simplified replication of the flexion and extension of the knee joint. The flexion of the knee involves a group of muscles generally known as the posterior thigh muscles (flexors) which pull the tibia toward the femur about the knee joint. The extension of the knee involves a group of muscles generally known as the anterior thigh muscles (extensors) which pull the tibia away from the femur about the knee joint (Spence, 1986). The flexor muscles are generally located behind the femur (posterior) while the extensor muscles are generally located in front of the femur (anterior) (McGinnis, 2005). The primary objective of the second control model was to allow for a comparison between the properties and behaviors of the spring, truss, and shell muscle models rather than producing an accurate and realistic simulation of the knee joint.

Two solid rectangular bars, which represented the femur and tibia bones, were connected at their mutual ends by a joint. Each bar had a length of 45 cm, a height of 3 cm, and a width of 1.5 cm. These dimensions were chosen to broadly mimic the actual dimensions of average femur and tibia bones. The femur bone was completely constrained while the tibia bone was free to rotate about the joint. The two bars were composed of elastic material with the same density of bone (approximately 1.90 g/cm^3) (Cameron et al., 1999). The adjacent ends of each bar were composed of rigid material in order for the joint to function properly in LS-DYNA. Overall, the control model provided a simplified femur-joint-tibia configuration for simulating the three muscle models. A profile view of the resulting control model is shown in Figure 5.19.

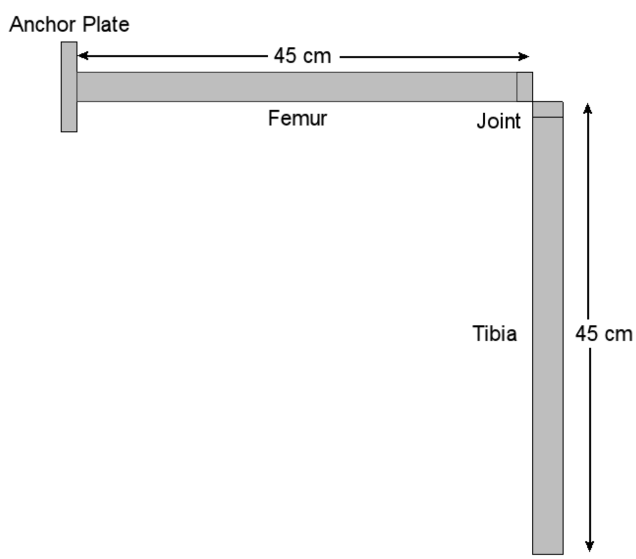

Figure 5.19. Profile view of Control Model II.

The properties and behaviors of a flexor muscle and an extensor muscle were obtained from literature. Specifically, the biceps femoris of the posterior compartment and the sartorius of the anterior compartment were chosen as the flexor and extensor muscles, respectively. Properties including mass, density, optimal muscle length, pennation angle, PCSA, maximum contraction velocity, and approximate peak isometric force were previously acquired for these muscles (Table 4.1). These properties were input accordingly into each of the muscle models, along with the adjustments previously determined in the investigation of Control Model I, for both the flexor and extensor muscles. Specifically, the total truss PCSA for the truss elements were adjusted accordingly.

Two types of simulations were performed, considering three different types of FE muscle models (spring element, truss element, and SMFE shell element), for a total of six runs. The first type of simulation included only representation of the flexor muscle (biceps femoris), to allow for investigation of knee flexion by activation of the flexor muscle without the influence of the extensor muscle. The setup of the second type of simulation considered both the flexor muscle and the extensor muscle (sartorius), to allow for investigation of knee extension by activation of extensor muscle along with the influence of the passive flexor muscle. The activation of the flexor muscle was disabled while the activation of the extensor muscle was enabled for the second test setup. Additionally, the stresses in the insertion point regions were investigated for each type of simulation. It is noted that the active muscles in all cases utilized activation curves identical to the activation curve utilized in the Control Model I section (Figure 5.7).

Figure 5.20 shows the configurations of each of the control models containing their respective muscle models for both types of simulations. It can be seen that in each case the first setup included the flexor muscle below the femur with its origin located on the anchor plate and its insertion point located just below the knee joint. The flexor muscle was activated for the first test setup. The second setup in each case included both the flexor muscle and the extensor muscle which spanned across the knee joint. The activation of the flexor muscle was disabled while the activation of the extensor muscle was enabled for the second setup.

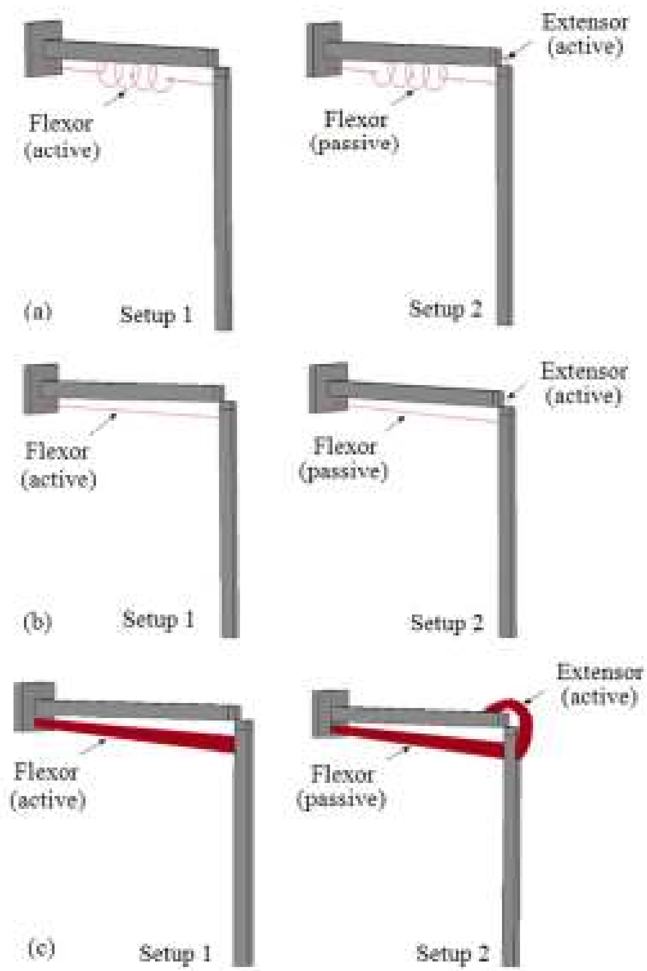

Figure 5.20. Configurations with (a) spring, (b) truss and (c) shell element muscle models.

Tables 5.2 and 5.3 show the properties of the biceps femoris and sartorius, respectively, along with the corresponding properties accommodated by each of the three FE muscle models. Figure 5.21 displays the plots of the resulting contraction velocities over time for the spring and truss flexor muscle models in the first type of simulation (flexion). Figure 5.22 displays the plots of the muscle forces over time for the spring and truss flexor muscle models in the first type of simulation. Data was obtained over a time ranging from 0 to 0.08 seconds for the flexion of the knee. Figure 5.23 displays the plots of the resulting contraction velocities over time for the spring and truss extensor muscle models in the second type of simulation (extension). Figure 5.24 displays the plots of the muscle forces over time for each of the extensor muscle models in the second type of simulation. Data was obtained over a time ranging from 0 to 0.16 seconds for the extension of the knee.

A wider time range was utilized for the collection of data from the shell model since this model is presumably the most effective model for further development. Hence, the results of the contraction velocity and muscle force for the shell model are plotted in separate figures. Figure 5.25 displays the plot of the resulting contraction velocity over time for the shell flexor muscle model in the first type of simulation (flexion). Figure 5.26 displays the plot of the muscle force over time for the shell flexor muscle model in the first type of simulation. Data was obtained over a time ranging from 0 to 0.2 seconds for the flexion of the knee. Figure 5.27 displays the plot of the muscle force over time for the shell extensor muscle model in the second type of simulation (extension). It is noted that the contraction velocity of the shell extensor muscle model was excluded due to unstable data plots. Data was obtained over a time ranging from 0 to 0.2 seconds for the extension of the knee.

Table 5.2. Biceps femoris muscle property inputs (Lieber, 2002).

Property	Biceps Femoris	Spring	Truss	Shell
Mass (g)	128	-	-	128
Density (g/cm^3)	1.056	-	1.056	1.056
L_o (cm)	34.2	45	-	-
Pennation angle (˚)	0	-	-	-
PCSA (cm^2)	12.8	-	0.256	0.256
V_{max} (cm/s)	171	171	-	-
Maximum strain rate (s^{-1})	5	-	5	5
F_{max} (N)	320	320	-	-
Peak isometric stress (N/cm^2)	25	-	25	25

Table 5.3. Sartorius muscle property inputs (Lieber, 2002).

Property	Sartorius	Spring	Truss	Shell
Mass (g)	61.7	-	-	62
Density (g/cm^3)	1.056	-	1.056	1.056
L_o (cm)	50.3	4.24	-	-
Pennation angle (˚)	0	-	-	-
PCSA (cm^2)	1.7	-	0.034	0.034
V_{max} (cm/s)	251.5	251.5	-	-
Maximum strain rate (s^{-1})	5	-	5	5
F_{max} (N)	42.5	42.5	-	-
Peak isometric stress (N/cm^2)	25	-	25	25

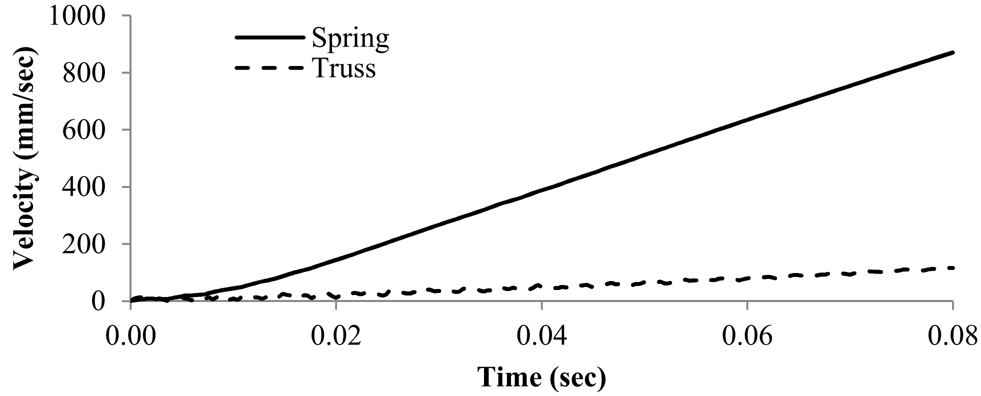

Figure 5.21. Contraction velocities of spring and truss flexor models.

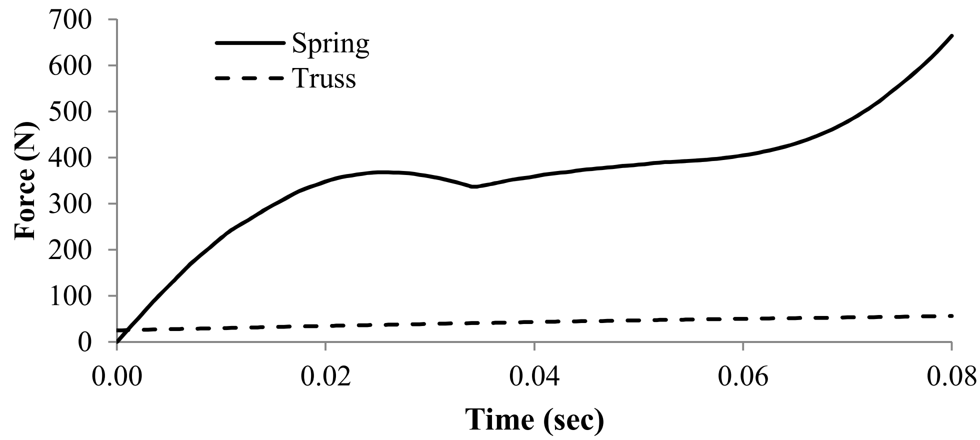

Figure 5.22. Muscle forces of spring and truss flexor models.

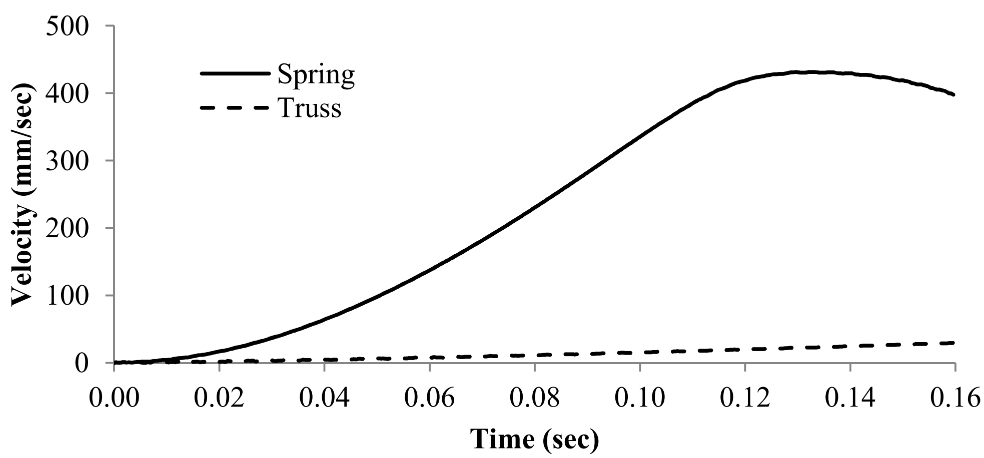

Figure 5.23. Contraction velocities of spring and truss extensor models.

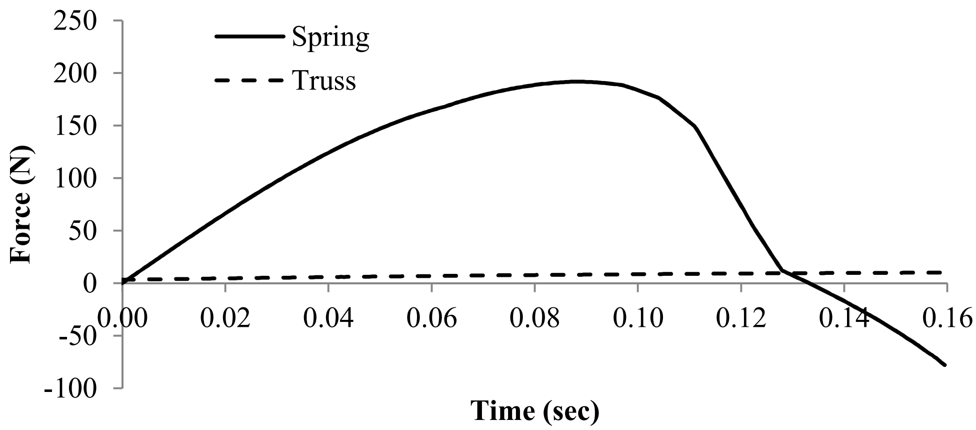

Figure 5.24. Muscle forces of spring and truss extensor models.

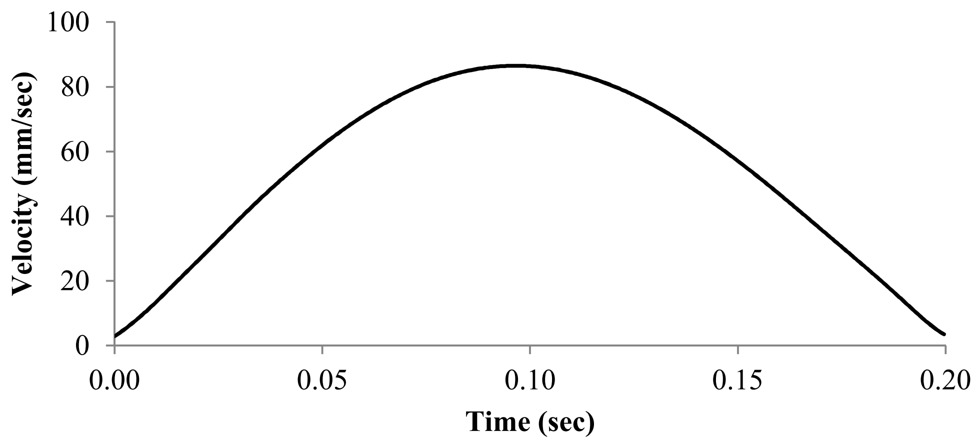

Figure 5.25. Contraction velocity of shell flexor model.

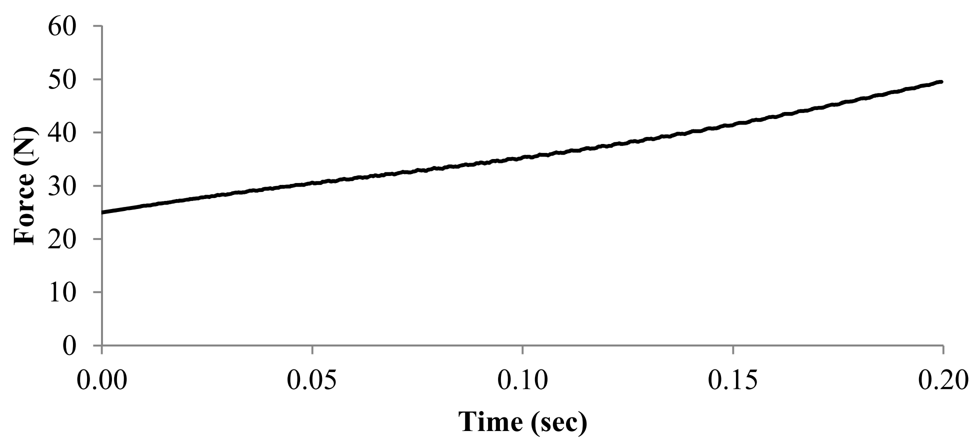

Figure 5.26. Muscle force of shell flexor model.

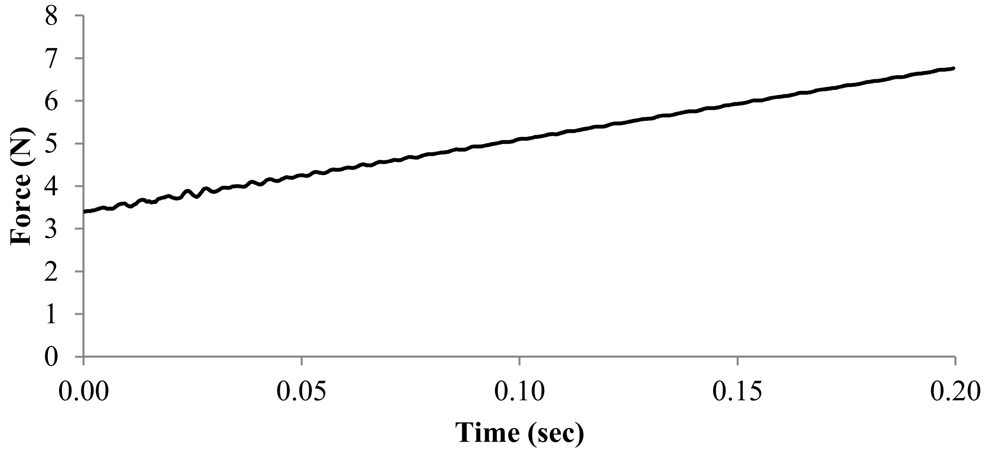

Figure 5.27. Muscle force of shell extensor model.

The differences between the results of the spring and truss models were evident despite the adjustments made to the truss model PCSA. These differences were to be expected due to the different properties and behaviors inherent to the two models. The contraction velocity functions of the flexor spring and truss element models for the first type of simulation were similarly shaped albeit on different scales. The contraction velocity of the spring model steadily rose to approximately 0.8 m/s at 0.08 seconds after activation, while the contraction velocity of the truss model rose to approximately 0.1 m/s at 0.08 seconds. The slightly unsteady contractile behavior exhibited by the truss model was presumed to be due to the rate of rotation allowed by the knee joint in LS-DYNA (*CONSTRAINED_JOINT_REVOLUTE card) when coupled with a truss discrete element.

The shape and scale of the muscle force functions of the flexor spring and truss element models for the first type of simulation varied substantially. The contractile force of the spring model steadily rose and plateaued at 350 N between 0.02 and 0.06 seconds after activation before it rose to 625 N at 0.08 seconds. The contractile force of the truss model steadily rose from an initial value of 25 N up to 55 N at 0.08 seconds after activation. Based on this data, it can be seen that the truss model exhibited much lower contractile velocities than the spring model and induced much less contractile force. Figure 5.28 demonstrates the flexion of the knee joint by the spring and truss element models in the first type of simulation.

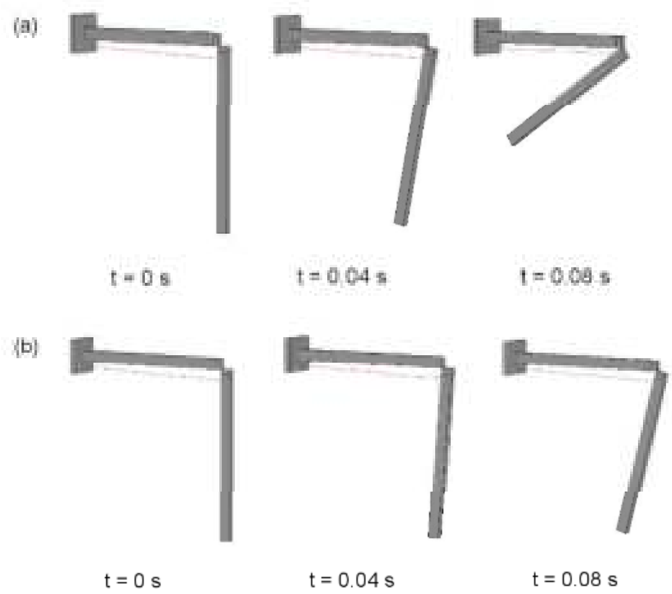

Figure 5.28. Flexion of knee joint with flexor (a) spring and (b) truss element models.

As previously mentioned, the extensor muscle for both the spring and truss models spanned across the knee joint from the femur to the tibia. An attempt was made to utilize the *CONTACT_GUIDED_CABLE card to allow for indirect lines of action. Using this card, a spring or truss element could presumably be "threaded" through a defined set of nodes, thus enabling contraction to occur about hinged or revolute joints. Unfortunately, the *CONTACT_GUIDED_CABLE card failed to perform properly in geometrically complex cases. As a result, only direct lines of action between origin and insertion points could be used. To overcome this problem, the extensor muscle was directly attached between nodes on the mutual ends of the femur and tibia mesh structures. However, this resulted in the length of the extensor muscle to fall far short of the actual length of the sartorius. Additionally, the actual locations of the origin and insertion points on the femur and tibia, respectively, could not be accurately replicated.

The contraction velocity of the extensor spring element model steadily rose to approximately 0.43 m/s at 0.125 seconds after activation and leveled off until 0.16 seconds. Additionally, the muscle force rose to a peak of 200 N at 0.08 seconds after activation before it rapidly decreased to zero at 0.13 seconds. The lower overall velocity of the extensor spring model when compared to the flexor spring model was concluded to be partially due to the resistance of the passive flexor model and the lower overall force induced by the extensor. As the active extensor muscle extended the knee joint, the passive flexor muscle resisted the extension.

It was discovered that the extension of the knee joint by the extensor truss element model was impossible to perform due to the presence of the passive flexor truss model. The resistance of the passive flexor muscle overcame the contractile force of the active extensor muscle and thus caused the knee joint to undergo flexion instead of extension. This effect was concluded to be due to the preload force inherent to truss elements which was previously encountered in the Control Model I section, and had important implications for the passive SMFE shell element model as will be shown later on. The flexor muscle was removed in order for the extensor muscle to perform the extension of the knee. With the exclusion of the flexor muscle, the contraction velocity of the extensor muscle steadily rose to 0.025 m/s at 0.16 seconds after activation, while the muscle force steadily rose from an initial value of 3 N to 10 N at 0.16 seconds after activation. Again, it can be seen that the truss model exhibited much lower contractile velocities and forces than the spring model even without the passive resistance of the flexor muscle. Figure 5.29 demonstrates the extension of the knee joint by the spring and truss element models in the second type of simulation.

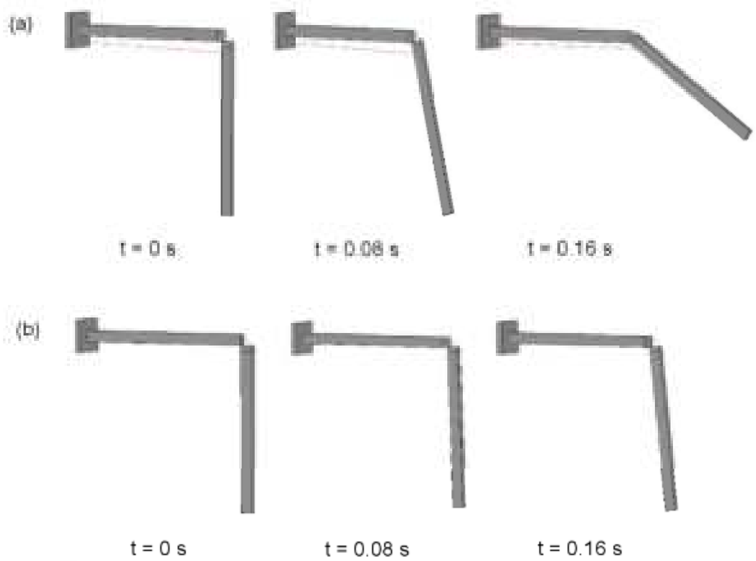

Figure 5.29. Extension of knee joint with extensor (a) spring and (b) truss element models.

The flexor SMFE shell element model consisted of a simple shell structure constructed of four interconnected shells giving the overall shell model a rectangular cross section (similar to the shell element model in the Control Model I section). The shell material utilized was Ogden rubber with a density of 1.056 g/cm^3 and a Poisson's ratio of 0.3. Each of the four shells possessed a thickness of 0.35 cm in order for the flexor muscle (biceps femoris) to have a mass of approximately 128 g. Four contractile truss elements were each attached to a corner node on each end of the shell so that each truss element's line of action was directed longitudinally along each of the four sides of the shell structure. Each truss element possessed a density of 1.056 g/cm^3. The total PCSA of the biceps femoris is 12.8 cm^3. Hence, in accordance with the PCSA adjustments determined in the Control Model I section, the total truss PCSA was 0.256 cm^2 (approximately 1/50 of the actual PCSA). Therefore, each of the four truss elements possessed a PCSA of 0.064 cm^2. The activation curve utilized for each truss element was identical to the activation curve utilized in the Control Model I section and the spring and truss models of Control Model II (Figure 5.7).

The time over which data was collected for the shell model ranged from initial activation to 0.2 seconds for both flexion and extension. The contraction velocity function of the flexor shell model was similarly shaped to a concave down quadratic function with a peak velocity of approximately 0.08 m/s at 0.1 seconds after activation. The contractile force of the flexor shell model rose from an initial value of 25 N up to 50 N at 0.2 seconds after activation. Contractile velocity and force data from 0 to 0.8 seconds was available for comparison between the spring, truss, and shell models. Based on the comparable data, it can be seen that the contractile velocity and force of the shell model is approximately identical to the truss model but much lower than the spring model. It was concluded, then, that the presence of the Ogden rubber shell material had very little influence on the dynamic properties of the muscle. The primary roles of the shells were to transmit and redistribute the stresses produced by the contractile elements throughout the muscle model, and to help transmit the stresses to the origin and insertion points. Additionally, the shells allowed for indirect lines of action by "guiding" the contractile action of the truss elements about joints.

The structure of the extensor SMFE shell element model was much more complex than the flexor shell model. Whereas the flexor muscle had a direct line of action, the extensor had an indirect line of action in that it acted around the knee joint. A relatively geometrically complex shell structure was therefore required. Several interconnected shells were utilized to form a hollow tube with a rectangular cross section. The overall structure was then formed into the shape of a horseshoe when viewed from profile (Figure 5.30a). One end of the shell structure was connected to a set of nodes near the end of the femur (origin) while the other end was connected to the top of the tibia (insertion). Several contractile truss elements were then integrated in series and parallel along the four edges of the shell structure (Figure 5.30b).

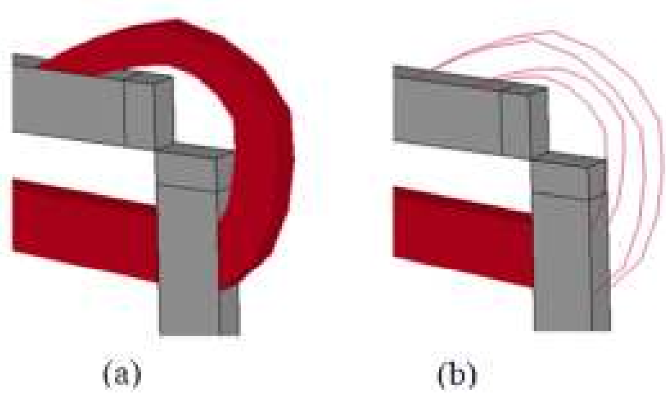

Figure 5.30. Extensor (a) shell and underlying (b) truss structures.

It was found from initial simulations that the use of Ogden rubber for shell models undergoing indirect lines of action failed to perform properly. Upon activation the contracting truss elements attempted to straighten out and in doing so caused the shells to tear apart. However, the use of elastic material overcame this problem. The use of elastic material was acceptable since it was previously found that the dynamic behavior of Ogden rubber and elastic material in an SMFE combination was nearly identical. Therefore, elastic material with a density of 1.056 g/cm^3 and a Poisson's ratio of 0.3 was utilized. A Young's modulus of 0.01 x 10^9 Pa pertaining to muscle was also input into the elastic material properties (Chen et al., 1996). The shells possessed a thickness of 0.65 cm in order for the extensor (sartorius) to have a mass of approximately 62 g. As with the flexor shell model, each truss element possessed a density of 1.056 g/cm^3.

The presence of contractile truss elements in the passive flexor shell model produced unwanted preload forces and caused the knee joint to unexpectedly contract. Therefore, the contractile truss elements were removed from the passive flexor shell model in order to allow the active extensor shell model to extend the knee joint. In this way, the passive resistance of the flexor was provided solely by the Ogden rubber shell structure. Ogden rubber with a density of 1.056 g/cm^3, a Poisson's ratio of 0.3, and a shell thickness of 0.35 cm was used for the passive flexor material. The behavior of passive shell muscle models was validated later on by utilizing the 50th percentile KTH model by Silvestri (2008) and experimental data from cadaver tests.

Initial test runs of the extensor shell model showed that the passive resistance of the flexor shell model prevented large extensions of the knee joint. This result was to be expected since the quadriceps muscle group within the anterior compartment are the primary muscles which perform the extension of the knee, of which the sartorius plays a minor role. Additionally, the geometry of the extensor shell model itself was not realistic in terms of replicating the geometry of the sartorius. Realistically, the sartorius has an origin point located on the pelvis rather than just above the knee joint. Furthermore, the behavior of the passive flexor had not yet been validated and may have caused unrealistic passive resistance.

The contractile forces produced by the extensor over time were consistent with the manual calculations from the Control Model I section. As mentioned before, the contraction velocities of the extensor were excluded due to unstable data plots. The modification of the total truss PCSA to a value other than that of 1/50 of the actual muscle PCSA presumably causes the shell model to behave unlike a real muscle and was thus not a viable option to produce greater knee joint extensions. It was presumed that the addition of all the anterior compartment muscles would have produced a realistic extension of the knee joint. However, as mentioned before, the primary objective of the second control model was to allow for a comparison between the properties and behaviors of the spring, truss, and shell element models rather than producing an accurate and realistic simulation of the knee joint. The flexion of the knee joint by the flexor shell model is shown in Figure 5.31a. The extension of the knee joint by the extensor shell model is shown in Figure 5.31b without the inclusion of the flexor for the purpose of demonstrating large extensions that would not have been otherwise possible with the inclusion of the flexor.

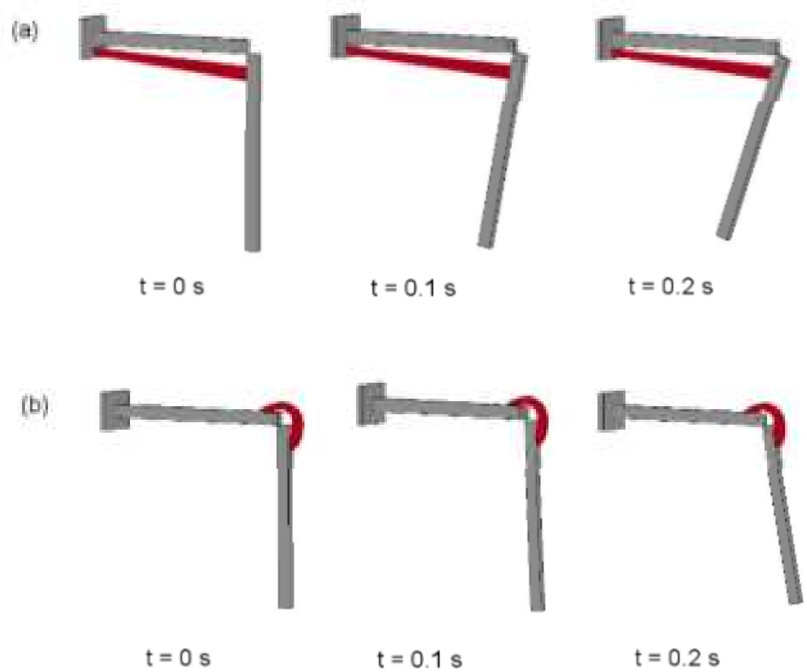

Figure 5.31. (a) Flexion and (b) extension of knee joint with shell element models.

The magnitude of stress in the region of an origin or insertion point is a function of the amount of force being induced by the attached muscle. The stress distributions on the isotropic elastic bars were presumably unrealistic since real bone possesses orthotropic material properties. The FE analyses demonstrated the varying stress distributions produced by each muscle model. The simplified bone models were compensated for in the 50th percentile KTH model by Silvestri (2008), which possesses much more realistic models of bones. Figure 5.32 shows Von Mises stress distributions on the flexor insertion region for each muscle model at the approximate midpoint of flexion. Figure 5.33 shows the stress distributions on the extensor insertion region at the approximate midpoint of extension.

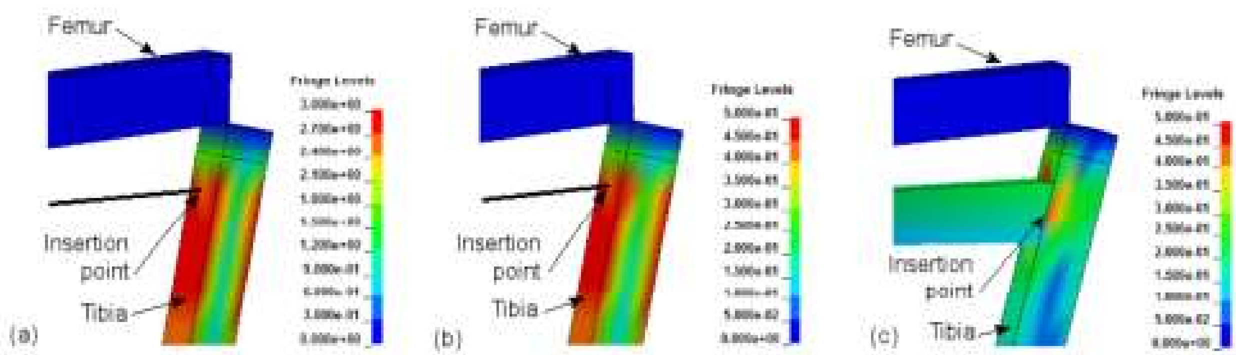

Figure 5.32. Von Mises stress distribution (N/mm^2) at insertion sites for (a) spring, (b) truss and (c) shell flexor model.

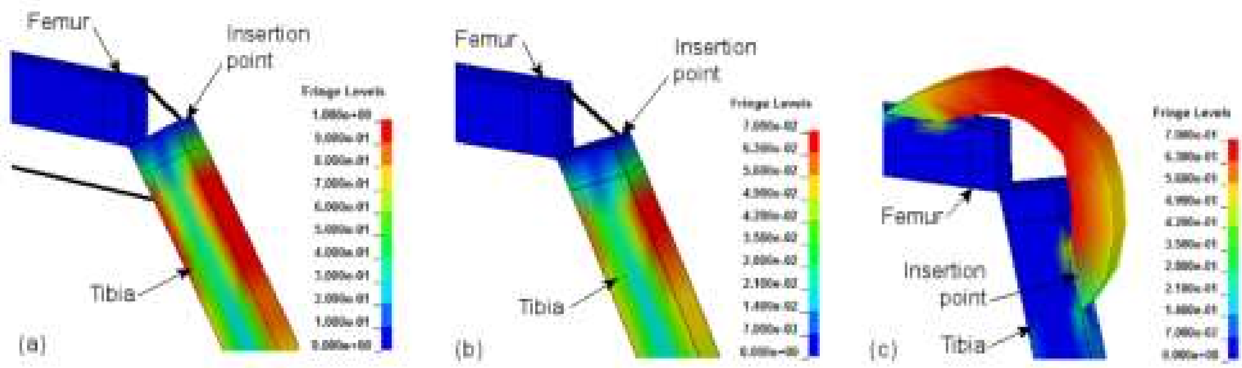

Figure 5.33. Von Mises stress distribution (N/mm^2) at insertion sites for (a) spring, (b) truss and (c) shell extensor model.

The stress distribution caused by each muscle model varied considerably. The spring and truss models produced peak stress areas concentrated primarily below the actual insertion point for both flexion and extension actions. This concentration of stress was most likely due to the contraction of the muscle producing bending stresses within the tibia. The red areas were indicative of the extreme fibers of the tibia undergoing stress from the flexure.

The shell model produced smaller magnitudes of stress over a less concentrated area. As expected, the stress gradually decreased as the distance from the insertion point gradually increased. The force produced by the contractile truss elements was not only inherently distributed due to the presence of four truss elements, but was further distributed by the presence of the shell elements which served to partially transmit the force from the truss elements to the tibia. It is presumed that this mechanism for transmitting force from the MTC complex to the bone is much more realistic than simply utilizing one dimensional contractile elements. In this way, realistic stress distributions on the origin and insertion points on bone were reproduced.

It was found that the most realistic muscle model was the SMFE combination using shell elements and contractile truss elements. For active muscles having direct lines of action, the shell material should be constructed of Ogden material with a density of 1.056 g/cm^3 and a Poisson's ratio of 0.3. The shell thickness should be appropriately proportioned so that the overall mass of the shell structure is approximately identical to the actual mass of the muscle being modeled. The contractile truss elements should be connected on each end to nodes on the origin and insertion points and should have a line of action coincident with the longitudinal edges of the shell structure. The total truss PCSA should be 1/50 that of the PCSA of the muscle being modeled and should be distributed equally among all of the truss elements. The remaining dynamic properties of the muscle being modeled should then be appropriately input into the truss properties. For active muscles having indirect lines of action, the shell material should be constructed of elastic material with a density of 1.056 g/cm^3, a Poisson's ratio of 0.3, and a Young's modulus of 0.01 x 10^9 Pa. Contractile truss elements should be arranged in series and parallel along the entire length of the longitudinal edges of the shell structure. Again, the total truss PCSA should be 1/50 that of the PCSA of the muscle being modeled and should be distributed equally among all of the truss elements. The remaining dynamic properties of the muscle being modeled should then be appropriately input into the truss properties. For passive muscles, the contractile truss elements should be removed leaving only the shell structure. Figure 5.34 shows a schematic of the properties that are input into the SMFE combination.

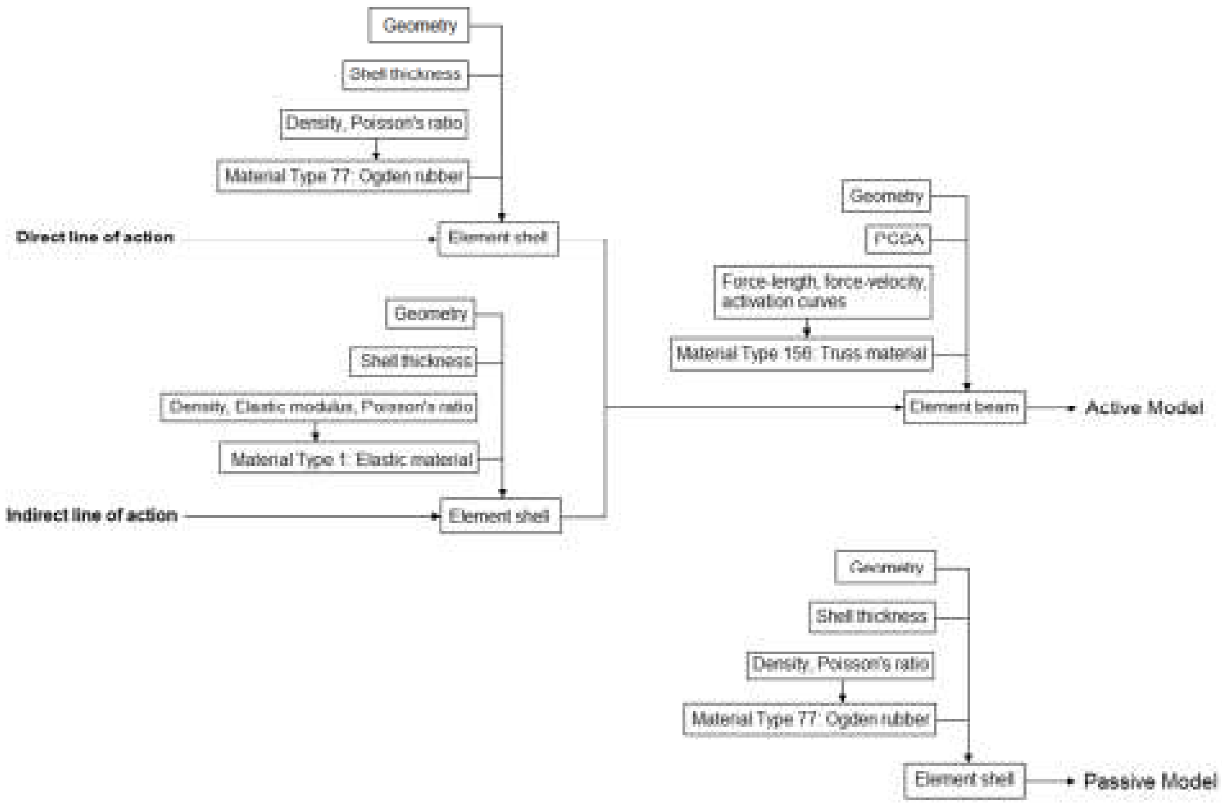

Figure 5.34. Schematic of property inputs for SMFE shell element model.

VI. Integration of Muscle Model into Existing KTH Model

This section outlines the characteristics of the existing KTH model as well as the process used in developing and integrating the muscles of the thigh into the KTH using the SMFE shell element model.

6.1 Overview of KTH Model

The 50^{th} percentile KTH finite element model draws its origins from a KTH model developed by LLNL as part of sponsored research with the National Highway Traffic Safety Administration (NHTSA) (Perfect et al., 1997). The LLNL KTH model was developed using DYNA3D and the FE pre-processor Truegrid (Silvestri, 2008). The model included the bone structure of the KTH represented by homogenous and isotropic solid elements as well as soft tissue representation. Additionally, the model included representation of muscles, tendons, and ligaments modelled with 1D spring elements. The model was sophisticated enough to investigate complex dynamic loading scenarios during crash simulations.

Silvestri (2008) improved upon the LLNL KTH model by consolidating prior research on bones, muscles, and ligaments and incorporating the research into the existing model. Specifically, a more refined mesh of the bones was created and the criteria of bone failure was added. Also, a ligament model presented by Farnese (2006) was integrated into the model. Muscles were represented by discrete one-dimensional Hill-based spring elements previously investigated and utilized by Olivetti (2006). Further improvements included flesh modeling and the modification of a knee bolster, pedal, and seat as well as seat belts to simulate the interior of a vehicle (Figure 6.1). The knee bolster consisted of a foam pad facing the occupant backed by a steel plate. Importantly, the DYNA3D analysis code was converted and made compatible for use in LS-DYNA.

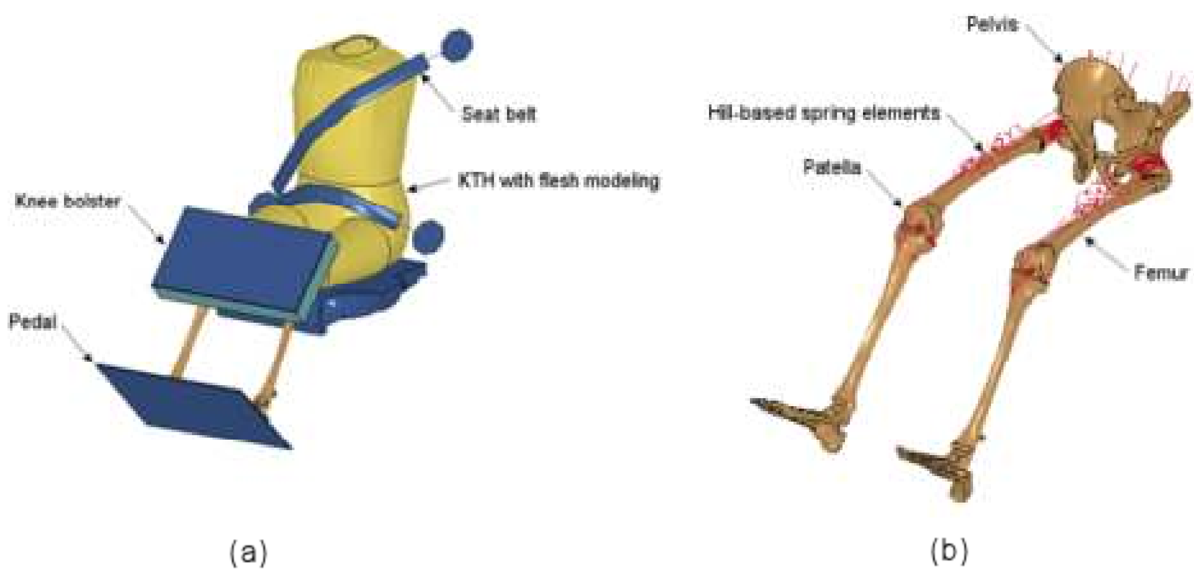

Figure 6.1. KTH with (a) flesh modeling, knee bolster, pedal, seat, and seat belts, and (b) underlying KTH musculo-skeletal model.

The KTH model was validated against cadaver sled tests performed by Rupp (2002). Specifically, the femoral axial force and the failure mechanisms observed were validated against the femoral axial force and failure mechanisms observed in the sled tests. Only passive properties of muscle were utilized although active muscles were later utilized to a limited extent.

6.2 Integration of SMFE Shell Element Model into KTH

The architectural properties of the muscle groups of the thigh were utilized to create corresponding SMFE shell element models of the muscles in a process previously outlined in Figure 5.34. Some of the muscles, such as vastus lateralis, vastus medialis, and vastus intermedius, were lumped into a single SMFE shell element model in order to simplify the process of integrating the muscles into the KTH. Other muscles, such as the biceps femoris and rectus femoris, were individually represented by an SMFE shell element model. A method was developed to easily deactivate specific muscles by turning the corresponding truss definitions in the *ELEMENT_BEAM card into comments. The muscles could then be reactivated by simply removing the comment notations.

Additional muscles (i.e. muscles of the foot, ankle, lower leg, etc.) were excluded from the KTH model in order to limit the scope of the research. This was considered to be acceptable since the parameters being investigated (i.e. axial forces and stress regions) were confined to the femur. It was assumed that active muscles besides those in the thigh would overwhelmingly affect the regions in which they were located while not largely affecting the femur. Hence, their exclusion would not have adverse effects on the resulting data concerning the femur.

The maximum strain rate and peak isometric stress for each muscle were input as 5 s^{-1} and 25 N/cm^2, respectively. The densities of the shell material (Ogden rubber or elastic material) and the truss elements were input as 1.056 g/cm^3. The total truss PCSA was input as 1/50 that of the actual PCSA of the muscle. The shell thickness for each muscle was adjusted in order for the shell structure to have a mass that was approximately the actual mass of the muscle being modeled. The thicknesses ranged anywhere from 0.1 cm to 1.0 cm.

Table 6.1 displays depictions of the muscles of the thigh along with the corresponding FE model representations.

Table 6.1. Real muscles and corresponding FE models (University of Washington Radiology, 2008).

Muscle	SMFE Shell Model
Adductor magnus	
	
Adductor longus	
	

<table>
<tr><td colspan="2">Adductor brevis</td></tr>
<tr><td>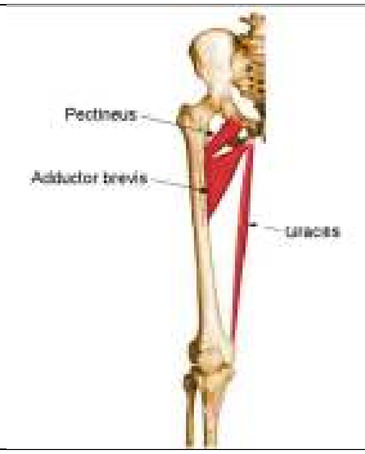
</td><td>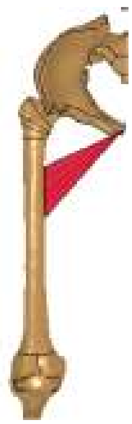</td></tr>
<tr><td colspan="2">Pectineus</td></tr>
<tr><td>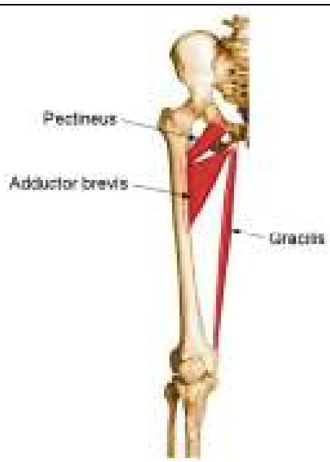
</td><td></td></tr>
<tr><td colspan="2">Gracilis</td></tr>
<tr><td>
</td><td></td></tr>
</table>

<table>
<tr><td colspan="2">Sartorius</td></tr>
<tr><td>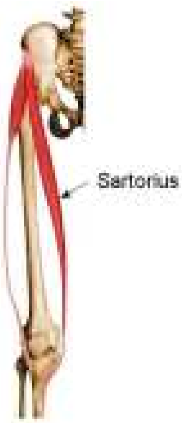
</td><td>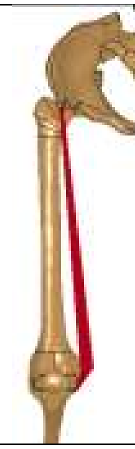</td></tr>
<tr><td colspan="2">Rectus femoris</td></tr>
<tr><td></td><td></td></tr>
<tr><td colspan="2">Vastus lateralis / Vastus medialis / Vastus intermedius</td></tr>
<tr><td>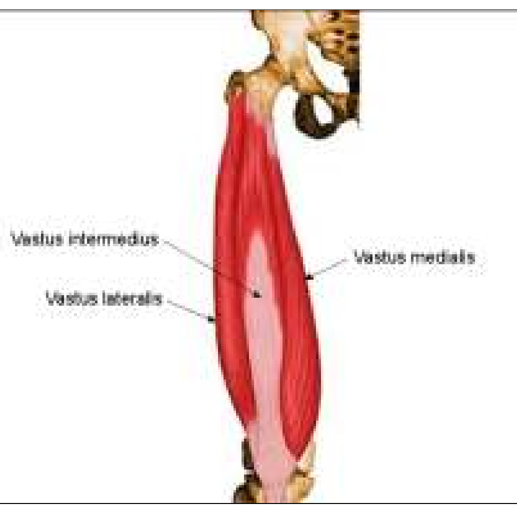
</td><td></td></tr>
</table>

Biceps femoris	
	
Semitendinosus	
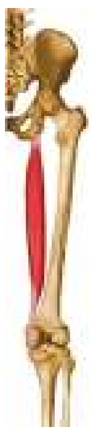	
Semimembranosus	
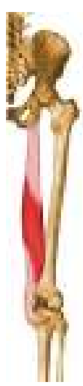	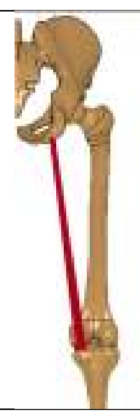

VII. Impact Simulations

This section outlines the general setup used for the FE impact simulations and the methods in which cadaver tests were performed from literature. Additionally, the procedures used in investigating the femoral axial forces and fracture mechanisms during impact simulations with passive and active muscles are outlined.

7.1 General Simulations Setup

The objective of the impact simulations were to replicate cadaver sled tests performed by Rupp (2002). As previously mentioned, this research assumed that the occupant of a vehicle was sitting in a neutral position with the thigh neither adducted or abducted (Figure 7.1). Furthermore, it was assumed that the type of crash was a pure frontal impact.

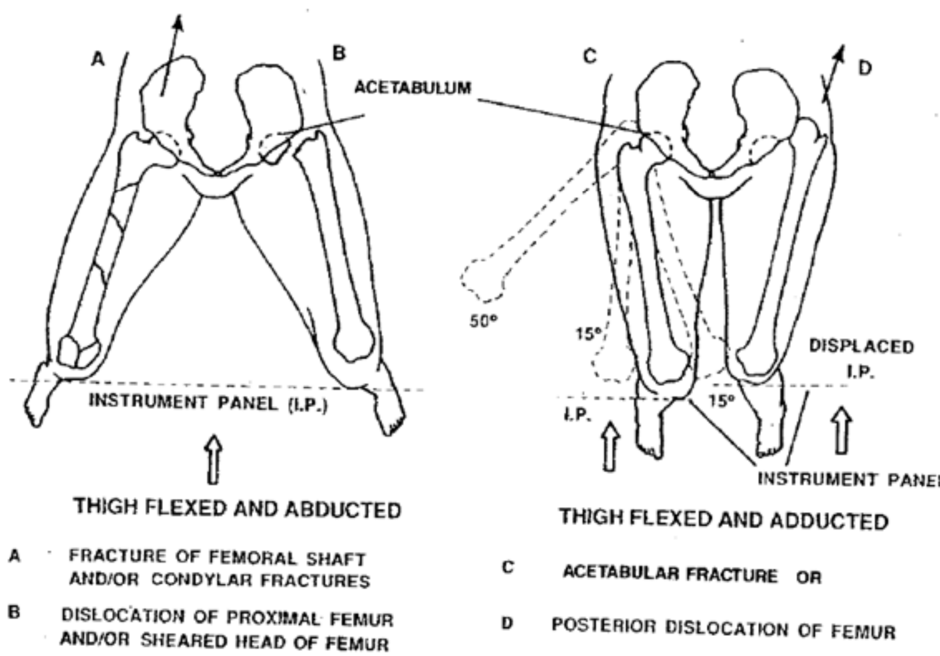

Figure 7.1. Thigh positions during pure frontal impacts and associated injury mechanisms (Hyde, 1992)

For each frontal impact simulation, the entire KTH model along with the knee bolster, pedal, seat, and seat belts were given an initial velocity of 13.41 m/s (30 mph) in order to replicate the parameters of the sled tests. The initial velocity was defined using the *INITIAL_VELOCITY card. The initial distance between the knee bolster and the patella on the KTH was set to approximately 3.8 cm. A prescribed deceleration curve was then applied to the knee bolster, pedal, seat, and seat belts to simulate a frontal collision by using the *BOUNDARY_PRESCRIBED_MOTION_SET_ID card. The inertia of the KTH caused it to impact the knee bolster with initial contact on the patella. The impact force was then transmitted through the patella to the femur and then to the pelvis via the acetabulum cup. The general pre-simulation configuration is shown in Figure 7.2.

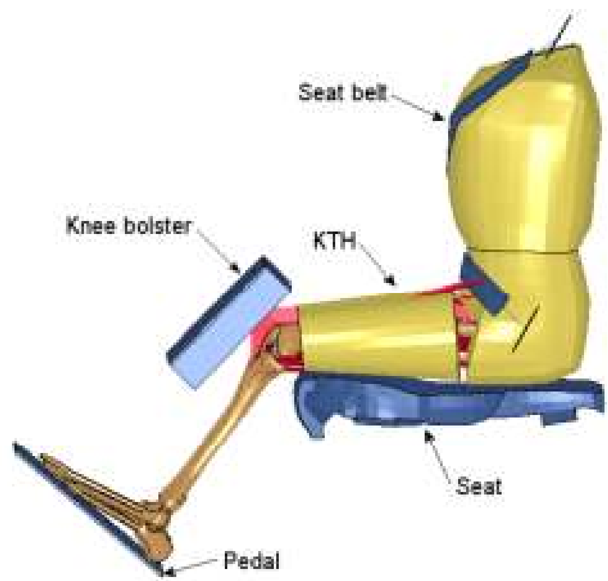

Figure 7.2. Typical pre-simulation configuration of KTH along with knee bolster, pedal, seat, and seat belts.

The axial femoral forces were obtained by using the *DATABASE_CROSS_SECTION_SET card. This card referenced a set of cross sections on the left femur and output time histories of the axial femoral forces to a SECFORC ASCII file by using the *DATABASE_SECFORC card. For this research, a cross section located at the midpoint on the left femur was used for data collection (Figure 7.3). The resulting time history plots were then filtered for clarity and exported to a spreadsheet program for final compilation. Appendix A displays some of the important cards used for a typical impact simulation.

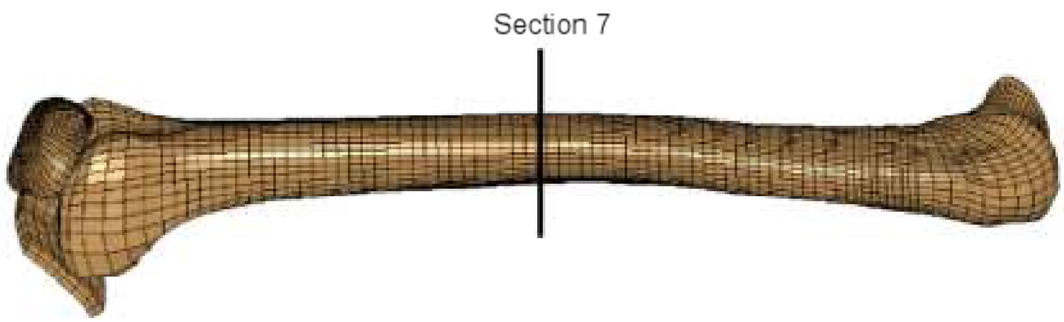

Figure 7.3. Location of cross section on left femur used for data collection.

A necessary parameter in the investigation of car crashes is the driver reaction time. The driver reaction time is the sum of the brake reaction time and the brake engagement time. The brake reaction time is the time it takes for a driver to recognize a hazard on the road ahead and to actually begin applying the brakes (i.e. time to initiate muscle activation). A standard value of the brake reaction time is 1.5 seconds. The brake engagement time is the time required to actually depress the brakes and for the brakes to engage (i.e. time to reach full muscle activation level). A standard value of the brake engagement time is 0.3 seconds. The duration of the overall driver reaction time is affected by many variables such as the age of the driver and urgency of the situation. (Green, 2000) For this research, it was assumed that a full muscle activation level was achieved prior to impact. In other words, the overall driver reaction time was assumed to have already passed and that the driver's muscles involved with braking were fully activated at the start of each impact simulation (Figure 7.4). This was done in order to significantly reduce the computation time required for each impact simulation. The deceleration curve was therefore applied immediately upon the start of each impact simulation. Each simulation was set to run for 0.8 seconds with a time step of 5.00e-7 seconds.

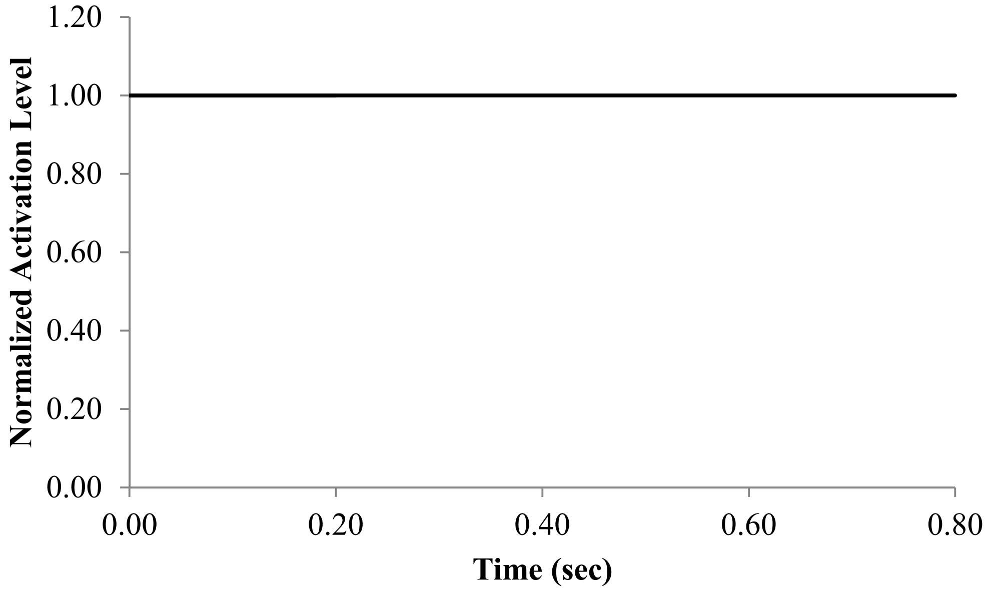

Figure 7.4. Activation curve used for the muscles of the thigh.

Following the integration of all of the muscles of the thigh into the KTH, several frontal impact simulations were performed. First, a series of simulations were performed to compare the behavior of the KTH with passive muscles to the cadaver sled tests. The muscles of the cadaver were inherently passive and therefore provided an acceptable comparison to the FE KTH model containing passive muscles. Specifically, the axial femoral forces observed in the FE simulations were compared to the axial femoral forces observed in the sled tests. The femoral fracture mechanisms were also investigated by observing Von Mises stress regions.

Next, additional sets of simulations were performed with active muscles. It is unclear as to exactly which muscles in the thigh are active during the actions of braking or bracing. Furthermore, the level of activation of those muscles during braking or bracing is uncertain. (Olivetti, 2006; Siegmund et al., 2007) Therefore, different combinations of muscles were activated in order to simulate those actions. As previously mentioned, it was assumed that the muscles being activated achieved a full activation level prior to impact. The femoral axial forces due to the collision and the pre-loading effects from the active muscles were then obtained. Additionally, the femoral fracture mechanisms were investigated by observing high stress areas. As previously stated, it was discovered that the level of axial force induced in the femur is a relatively good indicator of the probability of KTH injuries in general. Hence, the newly obtained femoral axial forces were presumed to be more realistic and therefore more accurate in indicating the probability of KTH injuries.

7.2 Overview of NHTSA Cadaver Tests

The cadaver sled tests were performed by the University of Michigan Research Institute (UMRI) as research sponsored by NHTSA. The purpose of the tests were to investigate the forces and fracture mechanisms within the KTH bones when impacted at different angles of flexion and adduction (Silvestri, 2008). A total of thirty seven tests were performed.

The physical test setups consisted of a cadaver positioned on a seat and strapped in with seat belts. The cadaver and seat along with a knee bolster replica were mounted on a sled (Figure 7.5). The thighs were positioned at varying angles of flexion and adduction for each test. The sled was then accelerated to a target velocity and then rapidly decelerated by a system of shock absorbers in order to replicate a frontal vehicle collision. Load cells mounted on the cadaver recorded the force, displacement, and acceleration time histories of the specimen as it impacted the knee bolster (Silvestri, 2008). For this research, the data collected from a load cell mounted on the left femur was used as a comparison to the data obtained from the FE impact simulations previously described (Figure 7.6). In terms of fracture mechanisms of the femur, the most common failure observed from the tests were femoral neck fractures. In fact, fractures of the femoral neck accounted for 64% of all fracture mechanisms of the femur (Silvestri, 2008).

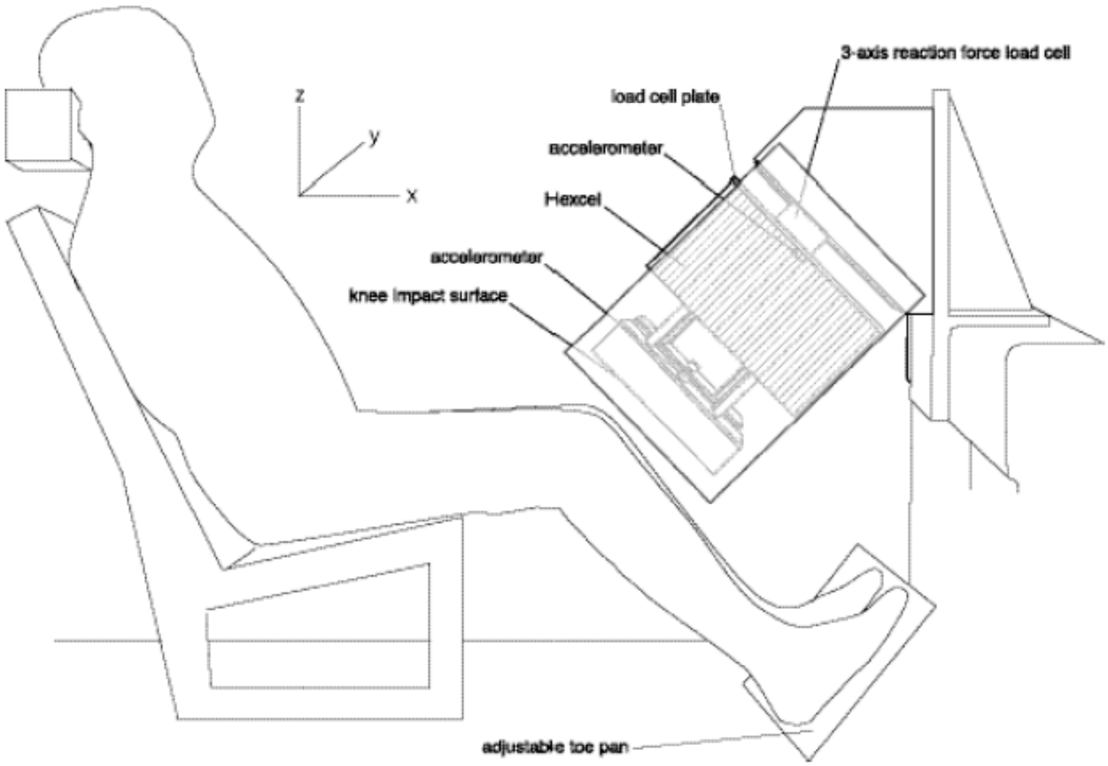

Figure 7.5. NHTSA sled test configuration (Rupp, 2002).

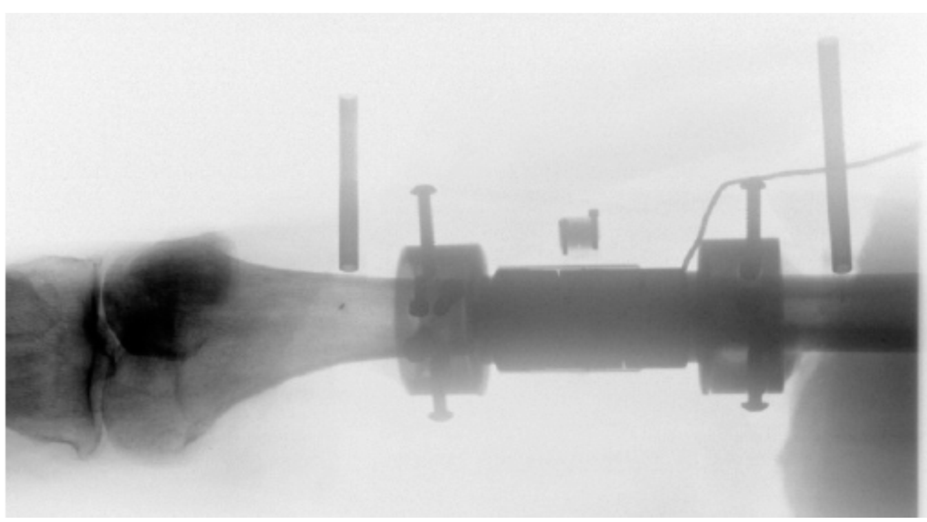

Figure 7.6. X-ray of load cell mounted on cadaver femur (Rupp, 2002).

The sled test of interest was referenced as test number NB0221 and was performed in March 2002. For this test the cadaver was positioned in a neutral position and the knee bolster replica was constructed of blue floatation foam. The cadaver was a 73 year old male with a mass of 100 kg. The target velocity of the sled was 30 mph and the target force was 8000 N. (Rupp, 2002) Figure 7.7 shows the pre-test and post-test setup of the sled test.

(a) (b)

Figure 7.7. (a) Pre-test setup and (b) post-test setup (Rupp, 2002).

7.3 Passive Muscles

The effect of the presence of passive muscles of the thigh on the femoral axial force as well as the fracture mechanisms during frontal collisions was first investigated. The SMFE shell element muscle models were set to passive by removing the contractile truss elements leaving only the mass of the shell elements. Several impact simulations were then performed and the femoral axial force as a function of time was obtained from the left femur and compared to the femoral axial force obtained from cadaver sled test number NB0221 performed by Rupp (2002). Figure 7.8 shows the KTH model containing all of the inactive muscles of the thigh prior to impacting the knee bolster while Figure 7.9 shows the KTH model upon impact with the knee bolster.

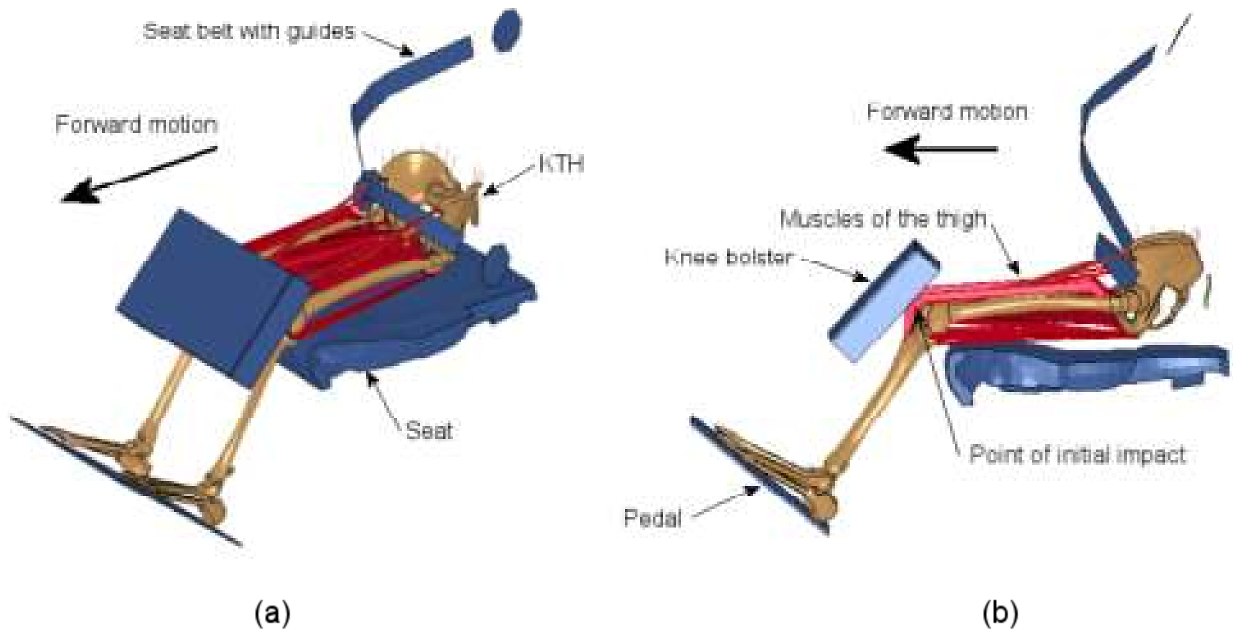

Figure 7.8. (a) Isometric view and (b) side view of the KTH model with muscles of the thigh (flesh modeling not shown for clarity).

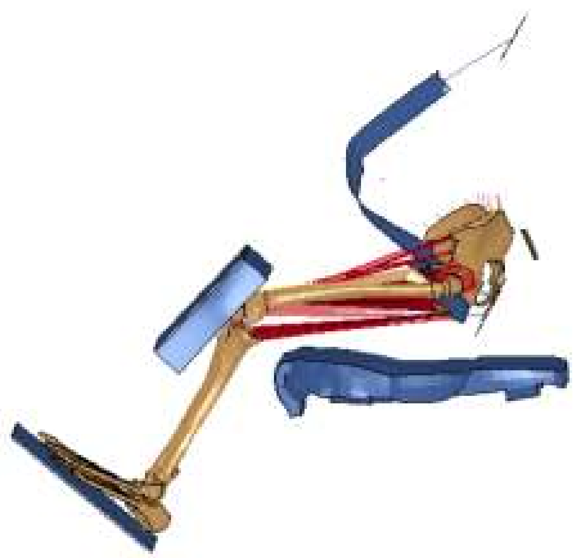

Figure 7.9. KTH model upon impact (flesh modeling not shown for clarity).

Plots of the femoral axial forces obtained from the impact simulations with inactive muscles along with the femoral axial forces obtained from cadaver test NB0221 are shown in Figure 7.10. It can be seen that the axial force of the left femur on the KTH model began to rise substantially at approximately 0.01 seconds after the start of the simulation. The axial force continued to rise steadily until the simulation terminated at approximately 0.03 seconds due to unresolved failed element errors. Fortunately, an adequate amount of data was obtained for comparison to the NB0221 test before the failure. The time at which the NB0221 axial force time history plot began to substantially rise was shifted in order to match the time at which the KTH femoral axial force began to substantially rise (0.01 seconds). With this adjustment it can be seen that the NB0221 femoral axial force rose at a lower rate than the KTH femoral axial force. This may be attributed to the extra mass that the SMFE shell element muscle models added to the overall mass of the KTH model causing the system to have a greater momentum.

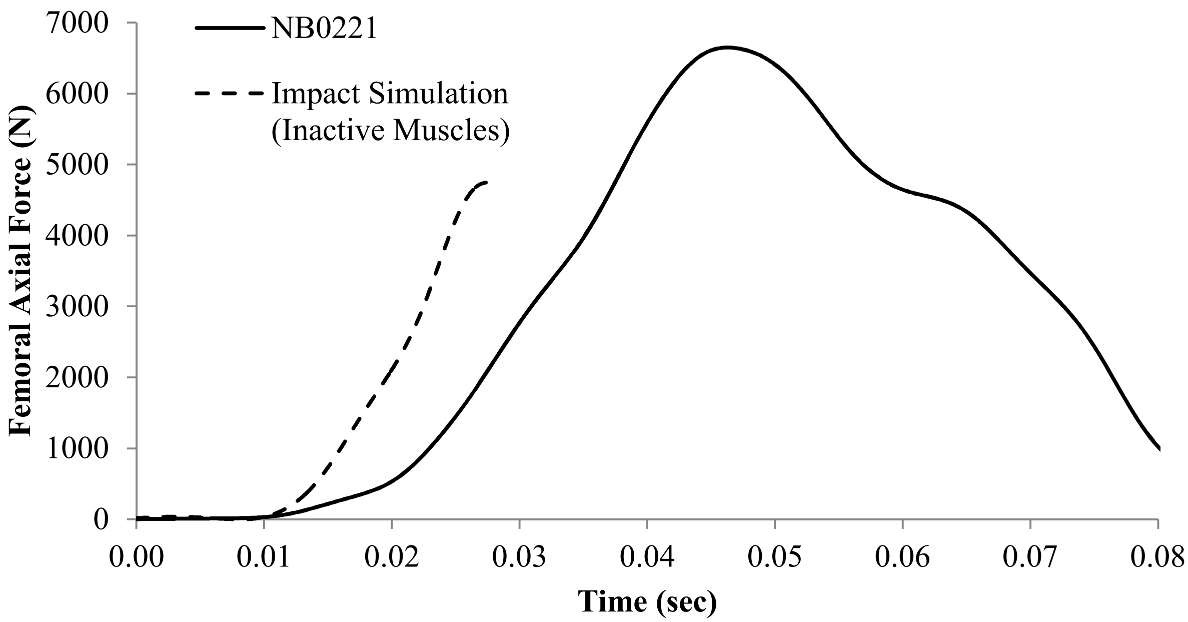

Figure 7.10. Femoral axial forces as functions of time during frontal collisions (with passive muscles).

Common injury mechanisms of the femur caused by high levels of axial force include fracture of the femoral shaft and fracture of the femoral head and neck. These fractures occur when the stresses on the femur exceed 190 MPa, which is the ultimate compressive strength of femoral cortical bone (Nahum and Melvin, 2002; Silvestri, 2008). Time history plots of the Von Mises stress of several elements on the left femur of the KTH were obtained from the impact simulations. The locations of the elements of interest are shown in Figure 7.11 with the corresponding time history Von Mises stress plots shown in Figure 7.12.

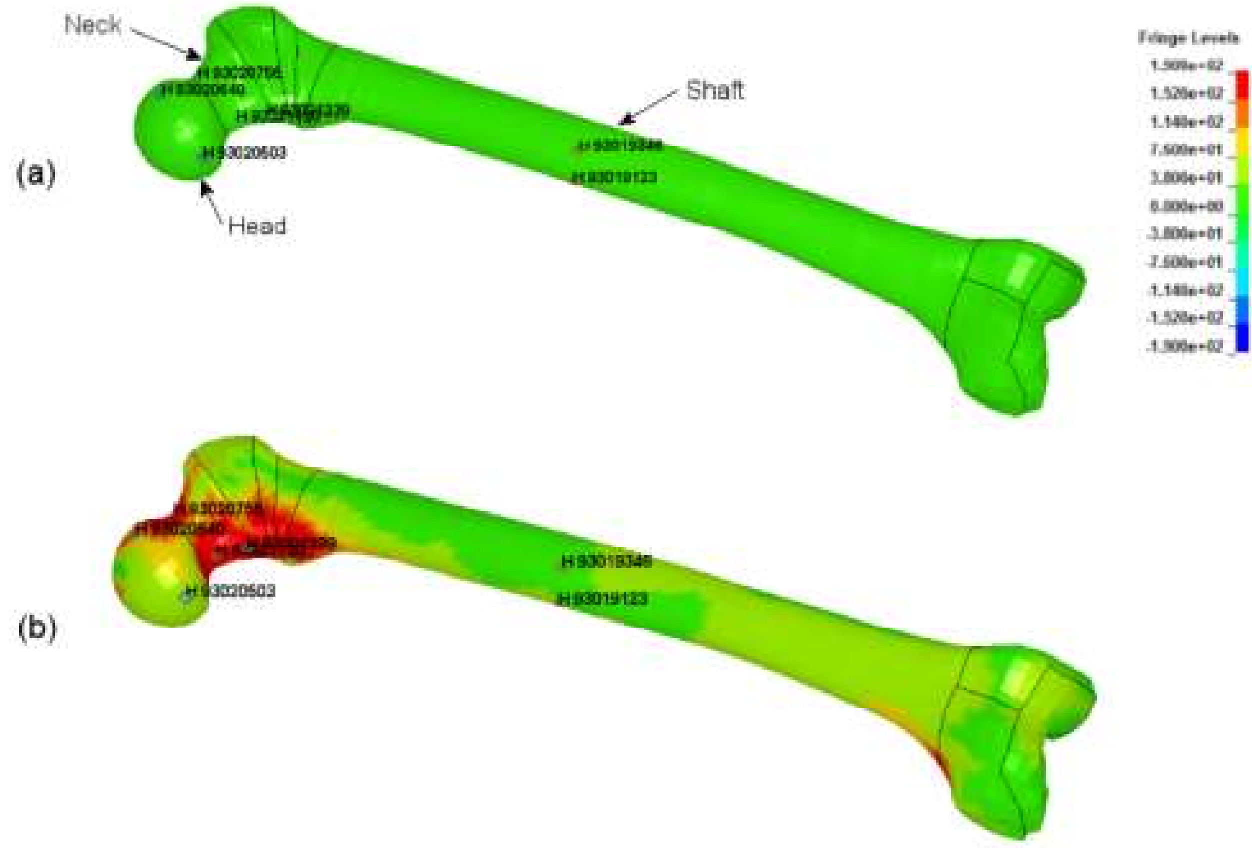

Figure 7.11. Locations of elements of interest on left femur (a) prior to impact and (b) at time of initial fracture with (passive muscles).

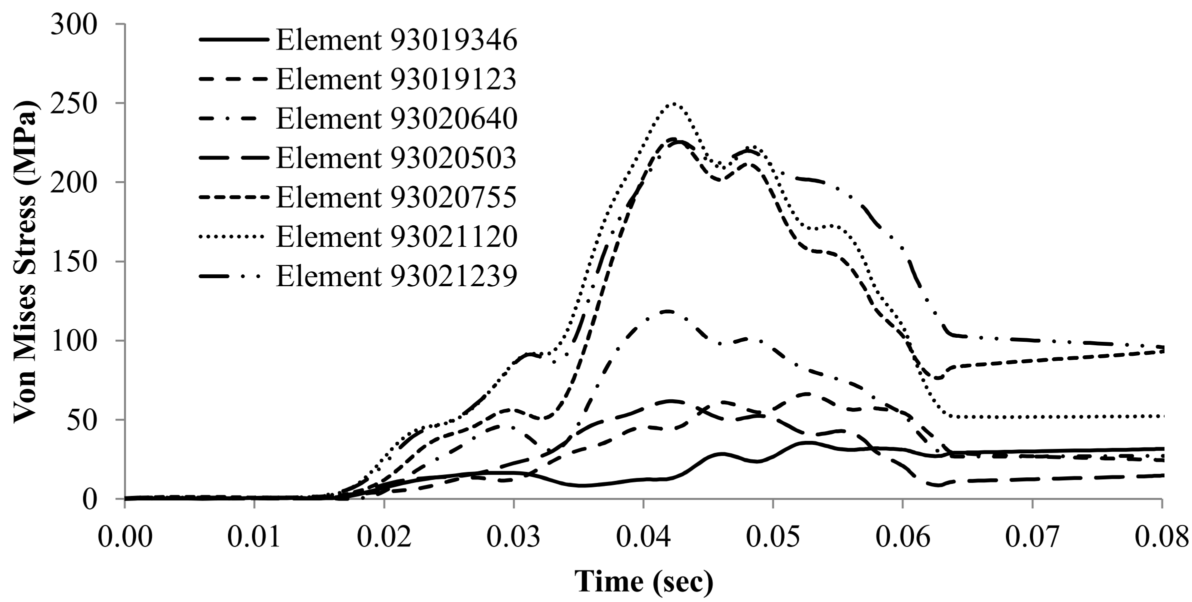

Figure 7.12. Von mises stresses of elements as functions of time with (passive muscles).

It can be seen that the elements of interest were located on the expected areas of failure (i.e. femoral shaft, neck, and head). Initial fracture occurred at Element 93021120, located on the femoral neck, at approximately 0.037 seconds after the start of the simulation. Fracture next occurred at Elements 93021239 and 93020755 which were also located on the femoral neck. The Von Mises stress of the remaining elements located on the femoral head and shaft never exceeded 190 MPa. Hence, the injury mechanism of the femur was wholly due to the fracture of the femoral neck, which is in agreement with the common fracture mechanisms of the femur observed in the sled tests.

The pelvis is another region of the KTH susceptible to fracture during frontal collisions. The acetabulum cup is especially prone to fracture since the axial forces from the femurs are transferred to the pelvis at this junction. However, this research focused primarily upon the pre-load forces from the muscle groups of the thigh on the femur. Therefore, a significant proportion of the muscle groups attached to the pelvis were not integrated into the KTH model. Although Von Mises stresses on the pelvis could have been obtained from the current KTH model, it was concluded that the absence of such a substantial portion of pelvic muscles would have produced uncertain stress results.

7.4 Active Muscles

The effect of active muscles of the thigh on the femoral axial force as well as the fracture mechanisms during frontal collisions was next investigated. Three impact simulations were performed with different combinations of the muscles of the thigh postulated to be active during the actions of braking or bracing. All of the active muscles were activated according to the activation curve previously shown in Figure 7.4. The femoral axial forces as functions of time were then obtained from the left femur and compared to the femoral axial forces obtained from the passive muscle simulations and from cadaver sled test number NB0221 conducted by Rupp (2002).

The four muscles of the quadriceps muscle group located in front of the thigh were activated for Impact Simulation #1. The quadriceps are typically used in exercises such as squat and dead lift (Glenn, 2010). It was assumed that the thrusting motion by the lower extremities involved in squatting was similar to the pushing motion involved in braking or bracing. The quadriceps muscles along with various combinations of muscles from the medial compartment were activated for Impact Simulations #2 and #3. Table 7.1 displays the muscles of the thigh which were activated for each of the three impact simulations. Figure 7.13 shows the corresponding KTH muscle configurations with the active muscles highlighted in blue.

Table 7.1. Activated muscles of the thigh.

Impact Simulation	Muscles Activated
1	Rectus femoris Vastus lateralis Vastus medialis Vastus intermedius
2	Adductor brevis Pectineus Gracilis Sartorius Rectus femoris Vastus lateralis Vastus medialis Vastus intermedius
3	Adductor magnus Adductor longus Sartorius Rectus femoris Vastus lateralis Vastus medialis Vastus intermedius

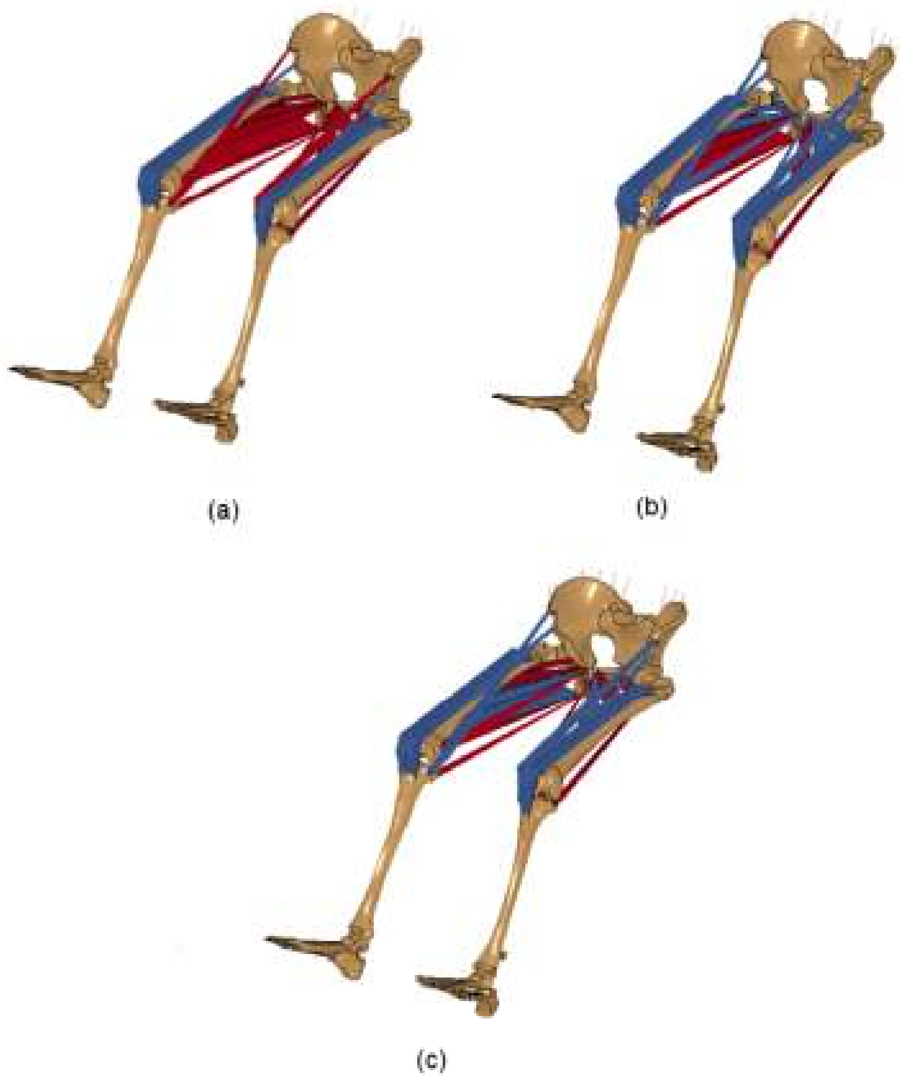

Figure 7.13. Activated muscles of the thigh for (a) Impact Simulation #1, (b) Impact Simulation #2, and (c) Impact Simulation #3 (knee bolster, pedal, seat, seat belt, and flesh modeling not shown for clarity).

Plots of the femoral axial forces obtained from the three impact simulations with active muscles along with the femoral axial forces obtained from the passive muscle simulations and cadaver sled test are shown in Figure 7.14. As with the impact simulations with passive muscles, the three impact simulations with active muscles were also subject to unresolved failed element errors. Despite this, plots showing the initial trend of axial forces were obtained. It can be seen that the femoral axial forces for the FE simulations rose at higher rates than the NB0221 test. Again, this may be attributed to the added mass of the SMFE shell element muscle models. It can also be seen that the femoral axial forces were highest for the impact simulations with active muscles with the highest values being attributed to Impact Simulations #1 and #2. Furthermore, during the span of time prior to the axial forces from the NB0221 test and the impact simulation with passive muscles substantially rising (i.e. before t = 0.01 seconds), axial forces from Impact Simulations #1, #2, and #3 were already present. Specifically, the axial forces from Impact Simulations #1 and #2 were approximately 300 N higher during that time duration. This data suggests that the active muscles in those simulations were in fact inducing pre-load forces in the femur prior to collision. If the data is compared with the NB0221 test, the pre-load force accounts for approximately 7% of the total femoral axial force from the NB0221 test at the time of initial fracture.

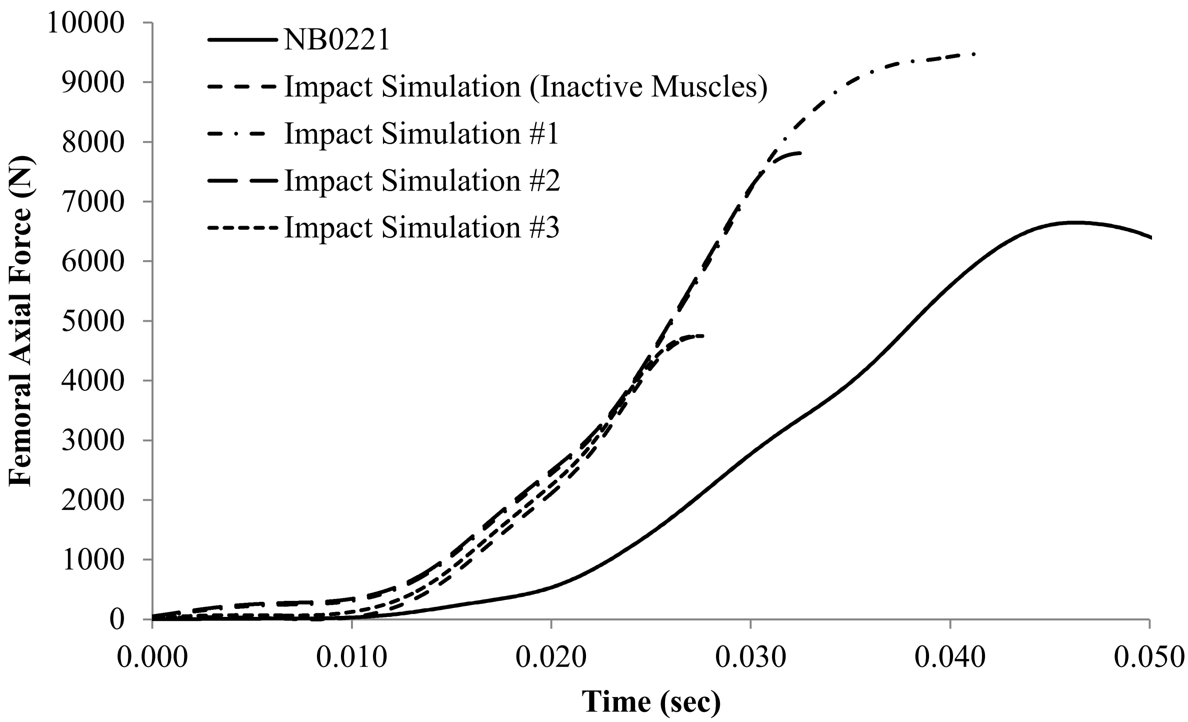

Figure 7.14. Femoral axial forces as functions of time during frontal collisions (with active muscles).

Time history plots of the Von Mises stress of several elements on the left femur of the KTH were obtained from Impact Simulation #1 since this simulation produced the most extreme axial forces. The locations of the elements of interest are shown in Figure 7.15 with the corresponding time history Von Mises stress plots shown in Figure 7.16. It can be seen that Element 93021120, located on the femoral neck, exceeded the fracture limit of 190 MPa at approximately the same time as when the same element exceeded the fracture limit with passive muscles (t = 0.037 seconds). Close observation shows that the stress plot of Element 93021120 from Impact Simulation #1 is slightly smoother than the stress plot of the same element with passive muscles. This suggests that the pre-load force from the active muscles served to slightly stabilize the rise in stress within the femur.

The critical stress pattern on the femur appeared to be narrowly concentrated on and near the femoral neck. On the contrary, the critical stress pattern from the impact simulation with passive muscles was more broadly distributed on the femoral neck and spread to the top of the femoral shaft. It may be postulated that the origin locations of the active vastus lateralis, vastus medialis, and vastus intermedius muscles, located near the femoral neck, caused the stress distribution to be directed towards the neck. Hence, it can be seen that the presence of active muscles resulted in the same injury mechanism as with passive muscles, except that the active muscles simply directed the stress to a more concentrated area on the femoral neck.

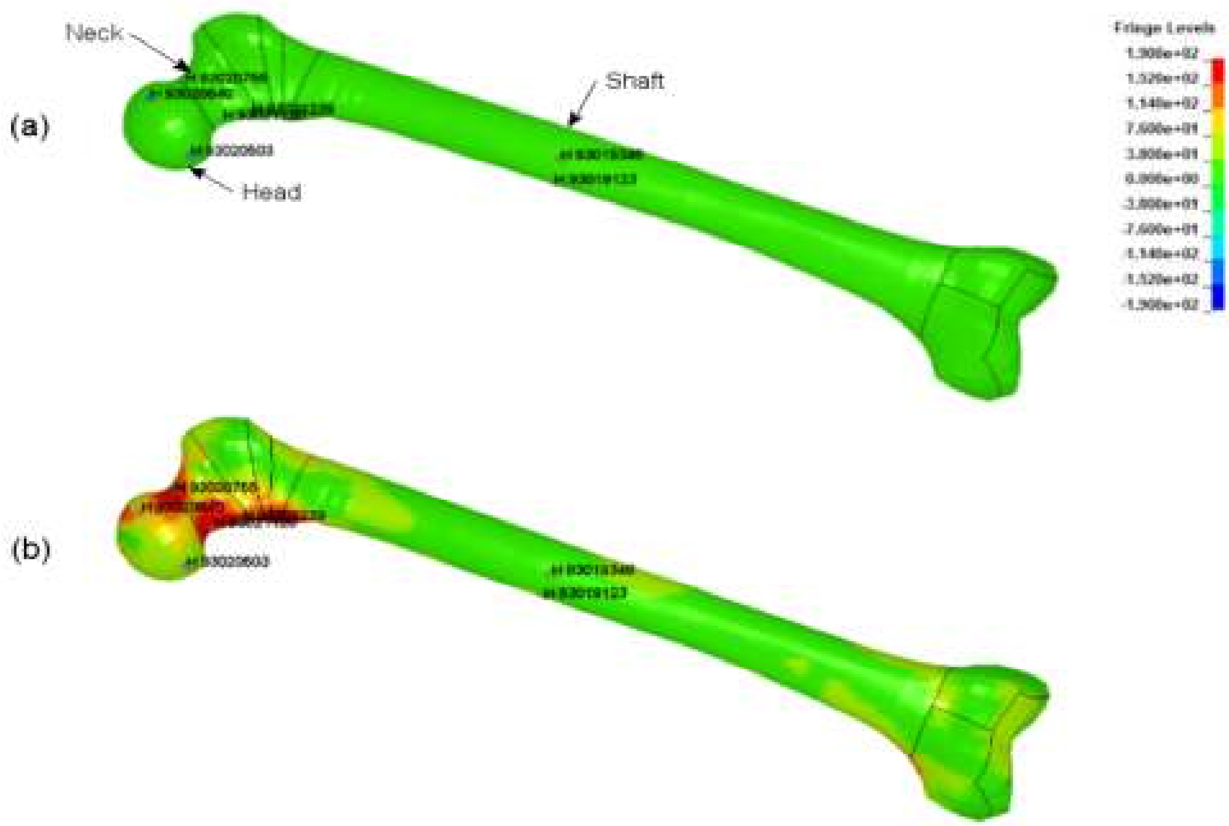

Figure 7.15. Locations of elements of interest on left femur (a) prior to impact and (b) at time of initial fracture for Impact Simulation #1.

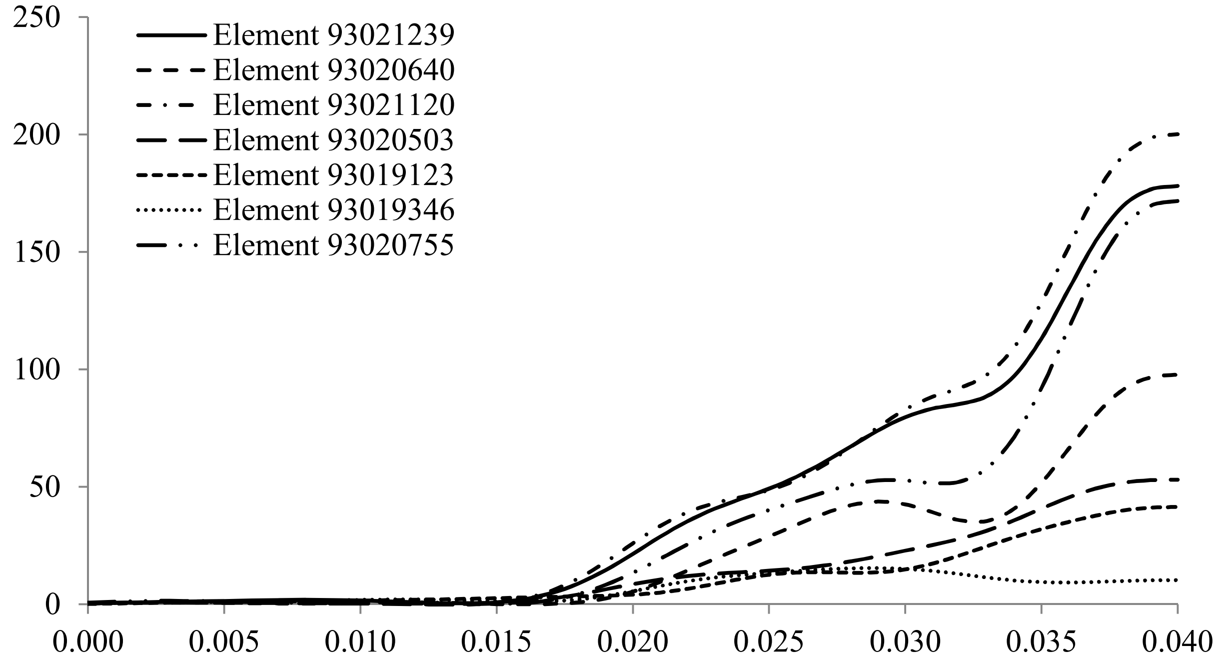

Figure 7.16. Von mises stresses of elements as functions of time for Impact Simulation #1.

VIII. Conclusions and Further Research

A finite element muscle model was developed with the purpose of integrating it into an existing musculo-skeletal model of a 50^{th} percentile KTH and investigating the pre-loading effects of active muscle on the femur during frontal crashes. Various finite element muscle models were investigated by comparing their contractile behavior to manually calculated muscle behavior. An SMFE shell element muscle model was ultimately chosen to be further developed. Shell elements were utilized in conjunction with Hill-based contractile truss elements to form the structure of individual muscles. Various parameters of the shell and truss elements were modified in order for the muscle model to sufficiently conform to the manually calculated muscle behavior and to each muscle being modeled.

Architectural properties of the muscles of the thigh were obtained from literature and used to help model the muscles using the SMFE shell element muscle model and to incorporate them into the KTH model. Impact simulations of the KTH impacting a knee bolster were then performed with passive muscles and various combinations of active and passive muscles. The simulations were compared to each other and to a cadaver sled test performed by Rupp (2002). The two primary parameters used for comparison between the simulations and the test were the femoral axial force and the fracture mechanism.

The rate of induced femoral axial forces observed in the impact simulations was noticeably higher than the rate of induced force observed in the sled test. This was presumed to be due to the added mass provided by the muscle models which caused the overall KTH model to have a greater momentum. Despite this disparity, a pre-loading femoral axial force of up to approximately 300 N due to active muscles was clearly observed when compared to the femoral axial force from an impact simulation with passive muscles. Furthermore, the pre-load force accounted for approximately 7% of the total femoral axial force from the NB0221 test at the time of initial fracture. This higher force indicates that a higher percentage of injuries to the KTH may be due to the effects of active muscles on the femur. The pre-loading force did not seem to decrease the time to initial fracture of the femur nor did it change the failure mechanism of femoral neck fracture. However, the active muscles appeared to stabilize the increase in stress in the femoral neck. Furthermore, the active muscles appeared to direct the stress towards a more concentrated region on the femoral neck than if the muscles were passive.

The manual calculations of muscle behavior made many simplifying assumptions which undoubtedly reduced the accuracy in describing the contractile behavior of real muscle. Furthermore, the contractile behavior of the shell element muscle models did not conform exactly to the manual calculations. It would have been preferred to compare and modify the behavior of the shell element models to behavior observed from actual testing of live skeletal muscle. Unfortunately, this type of testing remains an unresolved goal. Further research could possibly address these issues along with making further modifications to the parameters of the contractile truss elements to conform more closely to experimental results. Further research could also address the issue derived from the added mass from the muscle models on the KTH model causing higher rates of femoral axial force. The flesh modeling could possibly be reduced in order to compensate for the added mass. Finally, additional muscles of the KTH could possibly be modeled to investigate the effects of active muscle on the pelvis during frontal crashes.

IX. References

Biggs, John M. (1964). *Introduction to Structural Dynamics*. New York, NY: McGraw-Hill.

Calhoun Community College. (2009). “Paramedic Student’s Home Page.” Retrieved October 25, 2009 from http://www.calhoun.edu/distance/Internet/Natural/Healthlinks/ems/paramedic%20student%20page/Vol.%201%20Ch.%208a_files/slide0018_image005.jpg

Cameron, John R., Skofronick, James G., and Grant, Roderick M. (1999). *Physics of the Body,* 2nd Edition. Madison, WI: Medical Physics Publishing.

Chang, C.Y., Rupp, J.D., Kikuchi, N., Schneider, L.W. (2008). "Development of a finite element model to study the effects of muscle forces on knee-thigh-hip injuries in frontal crashes." *Stapp Car Crash Journal.*, 1, 475-504.

Chen, Eric J., Novakofski, J., Jenkins, W.K., and O'Brien, W.D. (1996). "Young's modulus measurements of soft tissues with application to elasticity imaging." *IEEE Transactions On Ultrasonics, Ferroelectrics, and Frequency Control.*, 43(1), 191-194.

Farnese, R., (2006). “A finite element model of the 50th percentile male human hip ligaments for impact loadings.” *Thesis*. Politecnico di Milano, Milano, Italia.

Gardner, W.D., Osburn, W.A. (1967). *Structure of the Human Body*. Philadelphia, PA, and London, UK: W.B. Saunders Company.

Glenn, L. (2010). "Smith Machine Squat." Muscle Mag Fitness. Retrieved April 1, 2010 from http://www.musclemagfitness.com/

Gray, H. (1918). *Anatomy of the Human Body.* Retrieved March 25, 2010 from http://www.bartleby.com/107

Green, M. (2000). "'How long does it take to stop?' methodological analysis of driver perception-brake times." *Transportation Human Factors*, 2, 195-216.

Hardin, E.C., Su, A., and van den Bogert, A.J. (2003). "Foot and ankle forces during an automobile collision: the influence of muscles." *Journal of Biomechanics*. 37, 637-644.

Hatze, H. (1981). *Myocybernetic Control Models of Skeletal Muscle: Characteristics and Applications.* Pretoria: University of South Africa.

Hedenstierna, S. (2008). "3D finite element modeling of cervical musculature and its effect on neck injury prevention." Doctoral thesis, Royal Institute of Technology, Stockholm, Sweden.

Hill, A. V. (1938). "The heat of shortening and the dynamic constant of muscles", Proc. Roy. Soc. 126B, 136-195.

Hill, A. V. (1939). "The dynamic constants of human muscle", Proc. Roy. Soc. 128(852), 263-274.

Hill, A. V. (1951). "The transition from rest to full activity in muscle: the velocity of shortening", Proc. Roy. Soc. 138(892), 329-338.

Huxley, H.E. (2000). "Past, present, and future experiments on muscle" Phil. Trans. R. Soc. Lond., 355, 539-543.

Hyde, A. S. (1992). "Chapter Five: Crash Injuries Of The Extremities", in *Crash Injuries: How and Why They Happen: A Primer for Anyone Who Cares About People in Cars*, Society of Automotive Engineers.

IBC Dent. (2005). "Biomechanics in Dentistry." Retrieved February 8, 2010 from http://www.feppd.org/ICB-Dent/campus/biomechanics_in_dentistry/ldv_data/mech/basic_bone.htm

Imberti, E., Ray, M.H., and Silvestri, C. (2007). “Affect of braking on fractures of the femur and acetabulum in frontal crashes using a finite element model of a 50th percentile male.” Bioengineering Institute, Worcester Polytechnic Institute, Worcester, MA.

Kindersley, D. (2007). "Skeletal System." Fact Monster. © 2000–2006 Pearson Education, publishing as Fact Monster. Retrieved February 8, 2010 from http://www.factmonster.com/dk/science/encyclopedia/skeletal-system.html

Kumar, S. (2004). *Muscle Strength.* Boca Raton, FL: CRC Press, LLC.

Kuppa, S. (2002). “An overview of the knee-thigh-hip injuries in frontal crashes in the United States.” National Highway Traffic Safety Administration, *ISSI*, 416, USA.

Kuppa, S., Wang, J., Eppinger, R. and Haffner, M. (2001). “Lower Extremity Injuries and Associated Injury Criteria.” Proceedings of the Seventeenth International Technical Conference on the Enhanced Safety of Vehicles, Amsterdam.

Lieber, R.L. (2002). *Skeletal Muscle Structure, Function, & Plasticity: The Physiological Basis of Rehabilitation,* 2nd Edition. Baltimore, MD: Lippincott Williams & Wilkins.

Linn, S. (1995). “The injury severity score – importance and uses.” *AEP*, 5(6), 440-446.

LSTC. (2007). *LS-DYNA Keyword User’s Manual*. (Vol. 1). Livermore, CA : Livermore Software Corporation.

MacIntosh, B.R., Gardiner, P.F., and McComas, A.J. (2006). *Skeletal Muscle: Form and Function*, 2nd Edition. Champaign, IL: Human Kinetics.

McGinnis, P.M. (2005). *Biomechanics of Sport and Exercise*, 2nd Edition. Champaign, IL: Human Kinetics.

Medical Look. (2010) "Muscles of Thigh and the Hip". Retrieved February 15, 2010 from http://www.medical-look.com/

Milner, C.E. (2008). *Functional Anatomy for Sport and Exercise: Quick Reference*. New York, NY: Routledge.

Nahum, A.M., and Melvin, J. (2002) "Accidentally Injury: biomechanics and prevention", Springer.

National Institutes of Health. (2010). "National Library of Medicine." Retrieved February 18, 2010 from http://www.nlm.nih.gov/

Nigg, B. M., MacIntosh, B. R., and Mester, J. (2000). *Biomechanics and Biology of Movement*. Champaign, IL: Human Kinetics.

NSHS. (2009). "Biomechanics and Movement Analysis." Retrieved October 28, 2009 from http://www.nambourshs.eq.edu.au/

Olivetti, N., (2006). "Development of a Hill's model of the human knee-thigh-hip region for frontal car crash simulations." Thesis, Politecnico di Milano, Milan, Italy.

Oomens, C. W. J., Maenhout, M., van Oijen, C. H., Drost, M. R., and Baaijens, F.P. (2003). "Finite element modeling of contracting skeletal muscle." Phil. Trans. R. Soc. Lond., 358, 1453–1460.

Perfect, S.A., Weiss, J.A., and Schauer, D.A. (1997) “Finite Element Modeling of the Human Anatomic Pelvis and Leg." *Final Report*, NHTSA.

Rupp, J.A. (2002) “‘Test Report No. NB0221’, Discretionary Cooperative Agreement in Support of Biomechanical Research – KTH Injury Investigations. The University of Michigan Transportation Research Institute (UMTRI)”, Ann Arbor, MI.

SEER Training Modules. "Classification of Bones." U. S. National Institutes of Health, National Cancer Institute. Retrieved February 10, 2010 from http://training.seer.cancer.gov/

Sherwood, L. (2007). *Human Physiology: From Cells to Systems,* 7th Edition. Belmont, CA : Brooks/Cole, Cengage Learning.

Siegmund, Gunter P., Blouin, Jean-Sebastien, Brault, John R., Hedenstierna, S., Inglis, Timothy J. (2007). "Electromyography of superficial and deep neck muscles during isometric, voluntary, and reflex contractions." *Journal of Biomechanical Engineering.,* 129, 66-77.

Silvestri, C., (2008). “Development and validation of a knee-thigh-hip LS-DYNA model of a 50th percentile male.” Dissertation, Worcester Polytechnic Institute, Worcester, MA.

Skeletal System. "Joints." Retrieved January 25, 2010 from http://www.skeletalsystem.net/joints.php

Sports Fitness Advisor. “Muscle Anatomy and Structure.” Retrieved October 25, 2009 from http://www.sport-fitness-advisor.com/muscle-anatomy.html

Spence, A.P. (1986). *Basic Human Anatomy,* 2nd Edition. Menlo Park, CA: The Benjamin/Cummings Publishing Company, Inc.

Stojanovic, B., and Kojic, M. (2007). “Modeling of musculoskeletal systems using finite element method.” *Journal of the Serbian Society for Computational Mechanics*., 1(1), 110-119.

Teresinski, G., (2005) “Chapter 10: Injuries of the Thigh, Knee, and Ankle as Reconstructive Factors in Road Traffic Accidents” in *Forensic Medicine of the Lower Extremity. Human Identification and Trauma Analysis of the Thigh, Leg, and Foot*, Humana Press.

Thaller, S., and Wagner, H. (2004). “The relation between Hill’s equation and individual muscle properties.” *Journal of Theoretical Biology*., 231, 319-332.

Turner, C.H., and Burr, D.B. (1993). “Basic biomechanical measurement of bone: a tutorial” Pergamon press.

University of Washington Radiology. (2008) "Muscle Atlas." Retrieved February 15, 2010 from http://www.rad.washington.edu/

Winters, J.M., and Savio, L-Y W. (1990). “Multiple Muscle Systems - Biomechanics and Movement Organization.” Springer-Verlag.

Appendix A - LS-DYNA Card Definitions

Important card definitions for Impact Simulaton #1

```
*PART
$# title
RECTUS FEMORIS
$      PID     SECID       MID     EOSID      HGID      GRAV    ADPOPT      TMID
$#     pid     secid       mid     eosid      hgid      grav    adpopt      tmid
       104       104       104
*SECTION_SHELL
       104         2     0.000         0         0         0         0         0
         5         5         5         5         0     0.000
*MAT_OGDEN_RUBBER
$#     mid        ro        pr         n        nv         g      sigf
       104 1.056E-09       0.3         2         0
$#     sgl        sw        st     lcid1      data     lcid2    bstart     tramp
         4         2         2         1                   2
*PART
$# title
RECTUS FEMORIS CE
$      PID     SECID       MID     EOSID      HGID      GRAV    ADPOPT      TMID
$#     pid     secid       mid     eosid      hgid      grav    adpopt      tmid
     10444     10444     10444
*SECTION_BEAM
     10444         3     0.000     0.000     0.000     0.000
      3.18     0.000
*MAT_MUSCLE_TITLE
RECTUS FEMORIS BEAMS
$#     mid        ro       sno       srm       pis       ssm       cer       dmp
     10444 1.056E-09       1.0         5   0.03125       0.5         1         0
$      alm       sfr       svs        tv       ssp
    -10444       1.0    -10000    -10001    -10000
```

```
*PART
$# title
BICEPS FEMORIS
$      PID     SECID       MID     EOSID      HGID      GRAV    ADPOPT      TMID
$#     pid     secid       mid     eosid      hgid      grav    adpopt      tmid
       128      1282       128         0         0         0         0         0
*SECTION_SHELL
$#   secid    elform      shrf       nip     propt   qr/irid     icomp     setyp
      1282         2     0.000         0         0         0         0         0
$#      t1        t2        t3        t4      nloc     marea      idof    edgset
  7.000000  7.000000  7.000000  7.000000     0.000     0.000     0.000         0
*MAT_OGDEN_RUBBER
$#     mid        ro        pr         n        nv         g      sigf
       128 1.0560E-9  0.300000         2         0     0.000     0.000
$#     sgl        sw        st     lcid1      data     lcid2    bstart     tramp
  4.000000  2.000000  2.000000         1     0.000         2     0.000     0.000
*PART
$# title
BICEPS FEMORIS CE
$      PID     SECID       MID     EOSID      HGID      GRAV    ADPOPT      TMID
$#     pid     secid       mid     eosid      hgid      grav    adpopt      tmid
     12888     12888     12888         0         0         0         0         0
*SECTION_BEAM
$#   secid    elform      shrf   qr/irid       cst     scoor       nsm
     12888         3     0.000         0         0     0.000     0.000
$#       a     rampt    stress
       3.2     0.000     0.000
*MAT_MUSCLE_TITLE
BICEPS FEMORIS BEAMS
$#     mid        ro       sno       srm       pis       ssm       cer       dmp
     12888 1.0560E-9  1.000000  5.000000    0.0625  0.500000  1.000000     0.000
$      alm       sfr       svs        tv       ssp
$#     alm       sfr       svs       svr       ssp
    -12888  1.000000    -10000    -10001    -10000
```

```
*PART
$# title
ADDUCTOR MAGNUS
$      PID     SECID       MID     EOSID      HGID      GRAV    ADPOPT      TMID
$#     pid     secid       mid     eosid      hgid      grav    adpopt      tmid
      1002      1002      1002         0         0         0         0         0
*SECTION_SHELL
$#   secid    elform      shrf       nip     propt   qr/irid     icomp     setyp
      1002         2     0.000         0         0         0         0         0
$#      t1        t2        t3        t4      nloc     marea      idof    edgset
        10        10        10        10     0.000     0.000     0.000         0
*MAT_OGDEN_RUBBER
$#     mid        ro        pr         n        nv         g      sigf
      1002 1.0560E-9  0.300000         2         0     0.000     0.000
$#     sgl        sw        st    lcid1      data     lcid2    bstart     tramp
  4.000000  2.000000  2.000000         1     0.000         2     0.000     0.000
*PART
$# title
ADDUCTOR MAGNUS CE
$      PID     SECID       MID     EOSID      HGID      GRAV    ADPOPT      TMID
$#     pid     secid       mid     eosid      hgid      grav    adpopt      tmid
    100222    100222    100222         0         0         0         0         0
*SECTION_BEAM
$#   secid    elform      shrf   qr/irid       cst     scoor       nsm
    100222         3     0.000         0         0     0.000     0.000
$#       a     rampt    stress
         4     0.000     0.000
*MAT_MUSCLE_TITLE
ADDUCTOR MAGNUS BEAMS
$#     mid        ro       sno       srm       pis       ssm       cer       dmp
    100222 1.0560E-9  1.000000  5.000000      0.05  0.500000  1.000000     0.000
$      alm       sfr       svs        tv       ssp
$#     alm       sfr       svs       svr       ssp
   -100222  1.000000    -10000    -10001    -10000
```

```
*PART
$# title
VASTUS(3)
$      PID     SECID       MID     EOSID      HGID      GRAV    ADPOPT      TMID
$#     pid     secid       mid     eosid      hgid      grav    adpopt      tmid
      1000      1000      1000         0         0         0         0         0
*SECTION_SHELL
$#   secid    elform      shrf       nip     propt   qr/irid     icomp     setyp
      1000         2     0.000         0         0         0         0         0
$#      t1        t2        t3        t4      nloc     marea      idof    edgset
        10        10        10        10     0.000     0.000     0.000         0
*MAT_ELASTIC
$#     mid        ro         e        pr        da        db         k
      1000 1.056E-09        10  0.300000     0.000     0.000     0.000
*PART
$# title
VASTUS(3) CE
$      PID     SECID       MID     EOSID      HGID      GRAV    ADPOPT      TMID
$#     pid     secid       mid     eosid      hgid      grav    adpopt      tmid
    100000    100000    100000         0         0         0         0         0
*SECTION_BEAM
$#   secid    elform      shrf   qr/irid       cst     scoor       nsm
    100000         3     0.000         0         0     0.000     0.000
$#       a     rampt    stress
        20     0.000     0.000
*MAT_MUSCLE_TITLE
VASTUS(3) BEAMS
$#     mid        ro       sno       srm       pis       ssm       cer       dmp
    100000 1.0560E-9  1.000000  5.000000    0.0625  0.500000  1.000000     0.000
$      alm       sfr       svs        tv       ssp
$#     alm       sfr       svs       svr       ssp
   -100000  1.000000    -10000    -10001    -10000
```

```
*PART
$# title
ADDUCTOR LONGUS
$      PID     SECID       MID     EOSID      HGID      GRAV    ADPOPT      TMID
$#     pid     secid       mid     eosid      hgid      grav    adpopt      tmid
      1003      1003      1003         0         0         0         0         0
*SECTION_SHELL
$#   secid    elform      shrf       nip     propt   qr/irid     icomp     setyp
      1003         2     0.000         0         0         0         0         0
$#      t1        t2        t3        t4      nloc     marea      idof    edgset
         3         3         3         3     0.000     0.000     0.000         0
*MAT_OGDEN_RUBBER
$#     mid        ro        pr         n        nv         g      sigf
      1003 1.0560E-9  0.300000         2         0     0.000     0.000
$#     sgl        sw        st    lcid1      data     lcid2    bstart     tramp
  4.000000  2.000000  2.000000         1     0.000         2     0.000     0.000
*PART
$# title
ADDUCTOR LONGUS CE
$      PID     SECID       MID     EOSID      HGID      GRAV    ADPOPT      TMID
$#     pid     secid       mid     eosid      hgid      grav    adpopt      tmid
    100333    100333    100333         0         0         0         0         0
*SECTION_BEAM
$#   secid    elform      shrf   qr/irid       cst     scoor       nsm
    100333         3     0.000         0         0     0.000     0.000
$#       a     rampt    stress
      2.72     0.000     0.000
*MAT_MUSCLE_TITLE
ADDUCTOR LONGUS BEAMS
$#     mid        ro       sno       srm       pis       ssm       cer       dmp
    100333 1.0560E-9  1.000000  5.000000      0.05  0.500000  1.000000     0.000
$      alm       sfr       svs        tv       ssp
$#     alm       sfr       svs       svr       ssp
   -100333  1.000000    -10000    -10001    -10000
```

```
*PART
$# title
SEMITENDINOSUS
$      PID     SECID       MID     EOSID      HGID      GRAV    ADPOPT      TMID
$#     pid     secid       mid     eosid      hgid      grav    adpopt      tmid
      1004     10042     10042         0         0         0         0         0
*SECTION_SHELL
$#   secid    elform      shrf       nip     propt   qr/irid     icomp     setyp
     10042         2     0.000         0         0         0         0         0
$#      t1        t2        t3        t4      nloc     marea      idof    edgset
         5         5         5         3     0.000     0.000     0.000         0
*MAT_OGDEN_RUBBER
$#     mid        ro        pr         n        nv         g      sigf
     10042 1.0560E-9  0.300000         2         0     0.000     0.000
$#     sgl        sw        st    lcid1      data     lcid2    bstart     tramp
  4.000000  2.000000  2.000000         1     0.000         2     0.000     0.000
*PART
$# title
SEMITENDINOSUS CE
$      PID     SECID       MID     EOSID      HGID      GRAV    ADPOPT      TMID
$#     pid     secid       mid     eosid      hgid      grav    adpopt      tmid
    100444    100444    100444         0         0         0         0         0
*SECTION_BEAM
$#   secid    elform      shrf   qr/irid       cst     scoor       nsm
    100444         3     0.000         0         0     0.000     0.000
$#       a    rampt     stress
         3     0.000     0.000
*MAT_MUSCLE_TITLE
SEMITENDINOSUS BEAMS
$#     mid        ro       sno       srm       pis       ssm       cer       dmp
    100444 1.0560E-9  1.000000  5.000000    0.0625  0.500000  1.000000     0.000
$      alm       sfr       svs        tv       ssp
$#     alm       sfr       svs       svr       ssp
   -100444  1.000000    -10000    -10001    -10000
```

```
*PART
$# title
PECTINEUS
$      PID     SECID       MID     EOSID      HGID      GRAV    ADPOPT      TMID
$#     pid     secid       mid     eosid      hgid      grav    adpopt      tmid
      1005      1005      1005         0         0         0         0         0
*SECTION_SHELL
$#   secid    elform      shrf       nip     propt   qr/irid     icomp     setyp
      1005         2     0.000         0         0         0         0         0
$#      t1        t2        t3        t4      nloc     marea      idof    edgset
       3.5       3.5       3.5       3.5     0.000     0.000     0.000         0
*MAT_OGDEN_RUBBER
$#     mid        ro        pr         n        nv         g      sigf
      1005 1.0560E-9  0.300000         2         0     0.000     0.000
$#     sgl        sw        st     lcid1      data     lcid2    bstart     tramp
  4.000000  2.000000  2.000000         1     0.000         2     0.000     0.000
*PART
$# title
PECTINEUS CE
$      PID     SECID       MID     EOSID      HGID      GRAV    ADPOPT      TMID
$#     pid     secid       mid     eosid      hgid      grav    adpopt      tmid
    100555    100555    100555         0         0         0         0         0
*SECTION_BEAM
$#   secid    elform      shrf   qr/irid       cst     scoor       nsm
    100555         3     0.000         0         0     0.000     0.000
$#       a     rampt    stress
       1.5     0.000     0.000
*MAT_MUSCLE_TITLE
PECTINEUS BEAMS
$#     mid        ro       sno       srm       pis       ssm       cer       dmp
    100555 1.0560E-9  1.000000  5.000000    0.0625  0.500000  1.000000     0.000
$      alm       sfr       svs        tv       ssp
$#     alm       sfr       svs       svr       ssp
   -100555  1.000000    -10000    -10001    -10000
```

```
*PART
$# title
ADDUCTOR BREVIS
$      PID     SECID       MID     EOSID      HGID      GRAV    ADPOPT      TMID
$#     pid     secid       mid     eosid      hgid      grav    adpopt      tmid
      1006     10062     10062         0         0         0         0         0
*SECTION_SHELL
$#   secid    elform      shrf       nip     propt   qr/irid     icomp     setyp
     10062         2     0.000         0         0         0         0         0
$#      t1        t2        t3        t4      nloc     marea      idof    edgset
         6         6         6         6     0.000     0.000     0.000         0
*MAT_OGDEN_RUBBER
$#     mid        ro        pr         n        nv         g      sigf
     10062 1.0560E-9  0.300000         2         0     0.000     0.000
$#     sgl        sw        st    lcid1      data     lcid2    bstart     tramp
  4.000000  2.000000  2.000000         1     0.000         2     0.000     0.000
*PART
$# title
ADDUCTOR BREVIS CE
$      PID     SECID       MID     EOSID      HGID      GRAV    ADPOPT      TMID
$#     pid     secid       mid     eosid      hgid      grav    adpopt      tmid
    100666    100666    100666         0         0         0         0         0
*SECTION_BEAM
$#   secid    elform      shrf   qr/irid       cst     scoor       nsm
    100666         3     0.000         0         0     0.000     0.000
$#       a     rampt    stress
         2     0.000     0.000
*MAT_MUSCLE_TITLE
ADDUCTOR BREVIS BEAMS
$#     mid        ro       sno       srm       pis       ssm       cer       dmp
    100666 1.0560E-9  1.000000  5.000000      0.05  0.500000  1.000000     0.000
$      alm       sfr       svs        tv       ssp
$#     alm       sfr       svs       svr       ssp
   -100666  1.000000    -10000    -10001    -10000
```

```
*PART
$# title
GRACILIS
$      PID     SECID       MID     EOSID      HGID      GRAV    ADPOPT      TMID
$#     pid     secid       mid     eosid      hgid      grav    adpopt      tmid
      1007      1007      1007         0         0         0         0         0
*SECTION_SHELL
$#   secid    elform      shrf       nip     propt   qr/irid     icomp     setyp
      1007         2     0.000         0         0         0         0         0
$#      t1        t2        t3        t4      nloc     marea      idof    edgset
       1.7       1.7       1.7       1.7     0.000     0.000     0.000         0
*MAT_OGDEN_RUBBER
$#     mid        ro        pr         n        nv         g      sigf
      1007 1.0560E-9  0.300000         2         0     0.000     0.000
$#     sgl        sw        st     lcid1      data     lcid2    bstart     tramp
  4.000000  2.000000  2.000000         1     0.000         2     0.000     0.000
*PART
$# title
GRACILIS CE
$      PID     SECID       MID     EOSID      HGID      GRAV    ADPOPT      TMID
$#     pid     secid       mid     eosid      hgid      grav    adpopt      tmid
    100777    100777    100777         0         0         0         0         0
*SECTION_BEAM
$#   secid    elform      shrf   qr/irid       cst     scoor       nsm
    100777         3     0.000         0         0     0.000     0.000
$#       a     rampt    stress
         1     0.000     0.000
*MAT_MUSCLE_TITLE
GRACILIS BEAMS
$#     mid        ro       sno       srm       pis       ssm       cer       dmp
    100777 1.0560E-9  1.000000  5.000000    0.0625  0.500000  1.000000     0.000
$      alm       sfr       svs        tv       ssp
$#     alm       sfr       svs       svr       ssp
   -100777  1.000000    -10000    -10001    -10000
```

```
*PART
$# title
SEMIMEMBRANOSUS
$      PID     SECID       MID     EOSID      HGID      GRAV    ADPOPT      TMID
$#     pid     secid       mid     eosid      hgid      grav    adpopt      tmid
      1008      1008      1008         0         0         0         0         0
*SECTION_SHELL
$#   secid    elform      shrf       nip     propt   qr/irid     icomp     setyp
      1008         2     0.000         0         0         0         0         0
$#      t1        t2        t3        t4      nloc     marea      idof    edgset
      12.5      12.5      12.5      12.5     0.000     0.000     0.000         0
*MAT_OGDEN_RUBBER
$#     mid        ro        pr         n        nv         g      sigf
      1008 1.0560E-9  0.300000         2         0     0.000     0.000
$#     sgl        sw        st     lcid1      data     lcid2    bstart     tramp
  4.000000  2.000000  2.000000         1     0.000         2     0.000     0.000
*PART
$# title
SEMIMEMBRANOSUS CE
$      PID     SECID       MID     EOSID      HGID      GRAV    ADPOPT      TMID
$#     pid     secid       mid     eosid      hgid      grav    adpopt      tmid
    100888    100888    100888         0         0         0         0         0
*SECTION_BEAM
$#   secid    elform      shrf   qr/irid       cst     scoor       nsm
    100888         3     0.000         0         0     0.000     0.000
$#       a     rampt    stress
      8.45     0.000     0.000
*MAT_MUSCLE_TITLE
SEMIMEMBRANOSUS BEAMS
$#     mid        ro       sno       srm       pis       ssm       cer       dmp
    100888 1.0560E-9  1.000000  5.000000    0.0625  0.500000  1.000000     0.000
$      alm       sfr       svs        tv       ssp
$#     alm       sfr       svs       svr       ssp
   -100888  1.000000    -10000    -10001    -10000
```

```
*PART
$# title
SARTORIUS
$      PID     SECID       MID     EOSID      HGID      GRAV    ADPOPT      TMID
$#     pid     secid       mid     eosid      hgid      grav    adpopt      tmid
      1009      1009      1009         0         0         0         0         0
*SECTION_SHELL
$#   secid    elform      shrf       nip     propt   qr/irid     icomp     setyp
      1009         2     0.000         0         0         0         0         0
$#      t1        t2        t3        t4      nloc     marea      idof    edgset
      1.78      1.78      1.78      1.78     0.000     0.000     0.000         0
*MAT_ELASTIC
$#     mid        ro         e        pr        da        db         k
      1009 1.056E-09        10  0.300000     0.000     0.000     0.000
*PART
$# title
SARTORIUS CE
$      PID     SECID       MID     EOSID      HGID      GRAV    ADPOPT      TMID
$#     pid     secid       mid     eosid      hgid      grav    adpopt      tmid
    100999    100999    100999         0         0         0         0         0
*SECTION_BEAM
$#   secid    elform      shrf   qr/irid       cst     scoor       nsm
    100999         3     0.000         0         0     0.000     0.000
$#       a     rampt    stress
      0.85     0.000     0.000
*MAT_MUSCLE_TITLE
SARTORIUS BEAMS
$#     mid        ro       sno       srm       pis       ssm       cer       dmp
    100999 1.0560E-9  1.000000  5.000000    0.0625  0.500000  1.000000     0.000
$      alm       sfr       svs        tv       ssp
$#     alm       sfr       svs       svr       ssp
   -100999  1.000000    -10000    -10001    -10000
```